Self-navigated Cine DENSE MRI for Free-breathing Myocardial Strain Imaging

---

A Dissertation

Presented to

the faculty of the School of Engineering and Applied Science

University of Virginia

---

in partial fulfillment
of the requirements for the degree

Doctor of Philosophy

by

Xiaoying Cai

May 2019

APPROVAL SHEET

This Dissertation
is submitted in partial fulfillment of the requirements
for the degree of
Doctor of Philosophy

Author Signature: 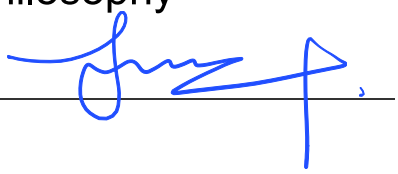

This Dissertation has been read and approved by the examining committee:

Advisor: Frederick H. Epstein

Committee Member: Craig H. Meyer

Committee Member: Daniel S. Weller

Committee Member: Kenneth Bilchick

Committee Member: John P. Mugler

Committee Member: _____

Accepted for the School of Engineering and Applied Science:

Craig H. Benson, School of Engineering and Applied Science

May 2019

Abstract

Myocardial strain imaging by echocardiography and magnetic resonance imaging (MRI) is increasingly used to assess cardiac function. Cine displacement-encoded stimulated-echoes (DENSE) MRI is a strain imaging technique that is accurate, reproducible and amenable to rapid displacement and strain analysis. With these properties, the clinical applications of cine DENSE are expanding. Recent studies demonstrated the potential of cine DENSE to improve implementation of cardiac resynchronization therapy in heart failure patients and detect subclinical ventricular dysfunction in childhood obesity. Studies in patients with acute myocardial infarction proved the prognostic value of strain by cine DENSE.

Conventionally, cine DENSE requires breath-holds for data acquisition, which is challenging in many patient populations, such as heart failure, pediatrics, and cardiomyopathy with dyspnea. A reliable free-breathing method is important for reproducible and efficient imaging in these patients. Although a conventional diaphragm-based navigator method (dNAV) was previously applied to enable free-breathing cine DENSE imaging, there are numerous disadvantages including the requirement of extra scout scans, variable imaging quality, sensitivity to respiratory pattern change, and reduced reproducibility. The field of cardiac MRI has shifted to self-navigated free-breathing methods where respiratory motion is typically extracted from the imaging data itself for motion compensation. The overall goal of this dissertation was to investigate the artifact sources in free-breathing cine DENSE and to develop and evaluate a self-navigated method that addressed these artifacts correspondingly.

A match-making reconstruction framework was developed to effectively compensate for two major sources of artifacts, namely the striping artifacts due to residual T_1-relaxation echo and blurring due to inter-heartbeat motion. The framework was validated through experimental data in phantom and healthy subjects. The phantom experiments demonstrated the concepts of the framework where minimal residual energy of the T_1-relaxation echo (rT1E) indicated little motion between the phase-cycling data and subsequent motion correction with image-based navigators reduced blurring

artifacts. A preliminary evaluation in healthy subjects showed that the framework can reduce free-breathing artifacts better than the conventional diaphragm navigator method.

An acquisition algorithm was designed to diminish rT1E adaptively in real-time. The algorithm calculates the rT1E values of new phase-cycling pairs and always repeats the k-space data portion with the highest rT1E during the acquisition until the rT1E is low enough or maximal imaging time is reached. Experiments in healthy subjects were performed to determine the stopping criteria. The results demonstrated that the rT1E decreased efficiently.

The presented self-navigated free-breathing method was evaluated in healthy volunteers and patients with heart disease. Free-breathing datasets were acquired with the adaptive algorithm and the image reconstruction was performed with compensation for both inter- and intra-heartbeat motion using stimulated-echo image-based navigators (ste-iNAV). The methods were found to achieve better image quality and more reproducible strain imaging than the dNAV method.

The self-navigated acquisition and reconstruction methods address the artifacts sources in free-breathing cine DENSE effectively and achieve reproducible segmental myocardial strain. Unlike dNAV, the method does not require extra set-up scans. These methods hold promise for reliable free-breathing strain imaging in patients with heart disease.

Acknowledgments

The past five and half years of working on this dissertation project has been an incredible experience. Looking back near the completion, I realized more than any time that it would not have been possible if it weren't for support and efforts from many people.

I am extremely grateful to my advisor, Dr. Frederick Epstein, for his exceptional mentoring. I really appreciate his continuous support and guidance with research and career development. His enthusiasm in research and humility is truly inspiring. I have been I feel extremely privileged to work with him. I would like to thank my advisory committee members, Drs. Craig Meyer, Daniel Weller, Kenneth Bilchick, and John Mugler for help shaping the dissertation project. I am grateful of them offering insightful suggestions whenever I met obstacles. I would also like to thank Dr. Michael Salerno for his encouragement throughout my graduate study and his help with the patient studies.

I am extremely grateful to my advisors during my undergraduate study, Drs. Kui Ying, Huijun Chen, and Jiangyang Zhang. They were the first ones that taught me about MRI research. I would also like to thank my friends and mentors outside of UVA, particularly Drs. Kelvin Chow and Bruce Spottiswoode for navigating me into the industrial world of MRI. I am extremely grateful to the wonderful colleagues I was fortunate to work with especially Drs. Xiao Chen, Dan Auger, Nivedita Naresh, Yang Yang and Bhairav Mehta for their tremendous help and insightful discussions.

I would like to thank the MRI technicians that I worked with. Joe Hylton and Jose Reyes, our research technologists, were always willing to help with patience and kindness when I had issues with scheduling, protocol or supplies, etc. My experiments would not have been so smooth without their help. I would also like to thank the clinical MRI team, who are super supportive with me when I needed to add-on to clinical studies to collect data in patients. Their schedule was always busy and stressful. I am grateful for them tolerating me being around and interrupting their procedures to gather data in the middle of the scans.

I am thankful to all the subjects who participated in my studies. Many volunteers offered their time for free and helped me get through the long period of trial and error

when developing my methods. The names are too many to count. I'm especially grateful to the patients who agreed to participate. These were people who I never met before, who were dealing with their conditions, and who would not benefit directly from their participation. Yet, they were all understanding and willing to help when I told them the purpose of my study was for research. I was truly moved when a patient consented before I needed to explain anything simply because "it helps other people". Working with these lovely people truly reminded me why we want to tackle the problems we are tackling. It is because we want to help people in need.

I am extremely thankful to the American Heart Association and the Children's Heart Foundation for supporting my predoctoral fellowship. The two organizations have also inspired me with their dedications to promote heart health and help those with heart conditions through supporting researches.

Most importantly, I am extremely grateful to my family and friends for their support through the days when things were not going so well. My parents have been extremely supportive of my decisions all the time and are willing to offer help and comfort whenever I needed extra strength to get over difficulties. I am very grateful of everything they have done for me.

Table of content

List of Figures

List of Symbols

α	flip angle
$\boldsymbol{A}$	affine motion matrix
B_0	main magnetic field
E	strain or image energy
E_{cc}	circumferential strain
E_{ll}	longitudinal strain
d	k-space data
d'	motion corrected k-space data
k	k-space position
k_x, k_y	k-space position in x- and y-directions
k'_x, k'_y	affine motion corrected k-space position in x- and y-directions
k_e	displacement-encoding frequency
k_d	through-plane dephasing frequency
M_{xy}	transverse magnetization
M_z	longitudinal magnetization
M_0	equilibrium longitudinal magnetization
S_{ref}	reference k-space segment
S_{cor}	the k-space segment to be corrected
t	time
t_x, t_y	in-plane translations due to breathing motion in x- and y-directions
T_1	spin-lattice relaxation time
T_2	spin-spin relaxation time
x, y, z	spatial location in 3D
x', y'	motion transformed spatial locations in the x- and y-directions
$\Delta x, \Delta y, \Delta z$	displacement in the x-, y-, and z-directions respectively
$\Delta\theta_b$	background phase

T_x, T_y, T_z	intra-heartbeat breathing induced translations of the heart
G_x, G_y, G_z	gradient in the x-, y- and z-directions
$\vec{\mu}$	magnetic moment
γ	gyromagnetic ratio
θ	global phase correction
W	displacement encoding matrix

List of Abbreviations

1D	one dimensional
2D	two dimensional
3D	three dimensional
3T	3 Tesla
AHA	the American Heart Association
ACQ	data acquisition
ANOVA	analysis of variance
BH	breath-holding
c-iNAV	conventional image-based navigator
CMR	cardiac magnetic resonance
CRT	cardiac resynchronization therapy
CT	computed tomography
dNAV	diaphragm-based navigator
DE	displacement encoding
DENSE	displacement-encoded stimulated-echoes
DVA	diminishing variance algorithm
DWI	diffusion weighted imaging
ECG	electrocardiography
ECHO	echocardiography
FB	free-breathing
FOV	field-of-view
FS	fat saturation
FT	Fourier transform
GLS	global longitudinal strain
HARP	harmonic phase imaging
HB	heart-beat
iNAV	image-based navigator
ICD	implantable cardioverter defibrillator
IFT	inverse Fourier Transform

LGE	late-gadolinium enhanced
LVEF	left ventricle ejection fraction
MC	motion correction
MRI	magnetic resonance imaging
MM	match-making of phase-cycling data
NMR	nuclei magnetic resonance
NUFFT	non-uniform fast Fourier Transform
ps-interleaves	post-subtraction spiral interleaves
PC	phase-cycling
PCA	principal component analysis
PhaCor	phase error correction
rT1E	residual T_1-relaxation echo energy
ROI	region-of-interest
self-NAV	self-navigated methods
ste-iNAV	stimulated-echo only image-based navigator
SENC	strain-encoded
SMS	simultaneous multi-slice
SNR	signal-to-noise ratio
SSFP	steady-state free-precession
T_1-echo	T_1-relaxation echo
TD	trigger delay time
TE	echo time
TPD	through-plane dephasing
TR	repetition time

Chapter 1

Introduction

1.1 Magnetic resonance imaging

Magnetic resonance imaging (MRI) is a widely used imaging technique for non-invasively assessing organ anatomy and function in clinics. MRI has numerous advantages over other imaging techniques, including versatile image planes, excellent tissue contrast and absence of ionizing radiation. Applications of MRI include brain imaging, cardiac imaging, abdominal imaging and musculoskeletal imaging.

MRI originated from the nuclear magnetic resonance (NMR) phenomenon discovered in 1946. An MRI system consists of three main components: a main magnet, a radio-frequency (RF) system, and a magnetic field gradient system. The main magnet creates the NMR phenomenon and subsequently generates magnetization in the direction of the main magnetic field. The RF system applies short-duration oscillating magnetic fields to perturb the magnetization to generate detectable magnetization in the transverse plane. The gradient system produces spatially non-uniform and time-varying magnetic fields for signal localization to allows the pixels of an image to be differentiated, which is crucial for imaging

1.1.1. Imaging signal

The imaging signal of MRI starts with the microscopic magnetic moment of an NMR-active nucleus, often noted as $\vec{\mu}$. Hydrogen nuclei are most commonly used for in-vivo imaging due to their abundance and their relatively strong response. Magnetic moments have certain magnitudes but completely random orientations in the absence of an externally applied magnetic field. Therefore, the net magnetization of a macroscopic object is zero at thermal equilibrium. However, exposure to a strong external magnetic field preferentially aligns lines up the magnetic moments and creates a bulk magnetization in the direction of the external magnetic field (z-axis), often noted as

longitudinal magnetization or M_z. The value of M_z and thermal equilibrium is noted as M_0. The observed M_z is the collective magnetic moment of many nuclei spins and each spin, in the classical physics description, still undergoes precession about the direction of the external magnetic field at a frequency determined by,

$$\omega = \gamma B_0, \tag{1.1}$$

known as the Larmor Frequency. B_0 is the strength of the main field and γ is a constant called the gyromagnetic ratio. The bulk magnetization of a voxel is a function of the total number of spins present, which is a tissue property, and the magnetic field strength.

Application of an RF pulse near the Larmor Frequency tips M_z away from the z-axis and creates a measurable transverse magnetization M_{xy}. The magnitudes of magnetizations after the RF pulse excitation are,

$$M_{xy}(0_+) = M_z(0_-)\sin(\alpha), \tag{1.2}$$

$$M_z(0_+) = M_z(0_-)\cos(\alpha), \tag{1.3}$$

where $M_z(0_-)$ is longitudinal magnetization before the excitation and α is the angle between the tipped magnetization and the z-axis, also known as the flip angle. The same coil for excitation or another coil tuned to the Larmor frequency can detect the precession of M_{xy} as imaging readouts.

After the excitation, the perturbed magnetizations will return to their thermal equilibrium M_0 given sufficient time. This process is called relaxation and can be described using solutions to the Bloch Equation,

$$M_z(t) = M_0\left(1 - e^{-t/T_1}\right) + M_z(t_0)e^{-t/T_1} \tag{1.4}$$

$$M_{xy}(t) = M_{xy}(t_0)e^{-t/T_2} \tag{1.5}$$

where T_1 and T_2 are time constants characterizing the relaxation. The recovery of longitudinal magnetization is called longitudinal relaxation, or T_1-relaxation and the loss of transverse magnetization is called transverse relation, or T_2-relaxation.

1.1.2. Segmented data acquisition

In MRI, the collected imaging signal after each excitation is in the Fourier domain of the image, the so-called k-space [1]. Reconstruction of a 2D image requires inverse 2D Fourier Transform with a set of sufficiently sampled k-space data, according to the Nyquist sampling theorem. Sampling the k-space can take various trajectories by varying the gradients during acquisitions. The number of k-space samples collected per readout is limited by relaxation effects, gradient limits and sampling rate, etc. In practice, the k-space is often divided into segments and sampled over multiple excitations and readouts, which is often noted as segmented acquisition [2]. As shown in Figure 1.1A, portions of the k-space are sampled separately and potentially at different times and the data are combined to reconstruct the image via inverse Fourier Transform.

1.1.3. Motion artifacts

The imaging speed of MRI is relatively slow. For example, it can take approximately 0.5 s (256 sampling lines and 2 ms for each line) to obtain a 2D image with a Cartesian trajectory and if acquisitions of all the sampling lines are performed. Due to the limited imaging speed, the quality of MRI images is prone to motion. Motion can occur during or among acquisitions of k-space segments. In either case, the k-space data become inconsistent and the reconstructed image via inverse Fourier Transform contains artifacts [3]. The appearance of motion artifacts varies depending on the type of motion, usage of signal preparation and sampling scheme. Figure 1.1 demonstrates the effects of incremental translation during Cartesian k-space sampling using simulations. In the case of in-plane translation, it can be blurring with sequential sampling order (Figure 1.1B) or ghosting with interleaved sampling order (Figure 1.1C). In non-Cartesian imaging, motion artifacts often appear as blurriness. How to compensate motion artifacts has been one of the focuses of research studies. Compensation strategies have been investigated for different applications using both prospective and retrospective corrections.

Particularly in cardiac magnetic resonance imaging (CMR), there are multiple motion sources, including cardiac motion and respiratory motion. Resolving cardiac motion can provide diagnostic information and is often achieved by imaging with electrocardiography (ECG) signal to trigger the acquisition during each heartbeat. With

ECG triggering, the acquisitions of different segments of a k-space are synchronized to the same delay time after detections of the R-waves (Figure 1.2A, B). The delay time can be adjusted to image a certain frame of the cardiac cycle. A simple and effective approach to manage respiration is to perform data acquisition during breath-holding, which is typically employed in clinical CMR scans. Figure 1.2C, D demonstrate that both beating motion of the heart and respiration can create artifacts in CMR images when not well managed.

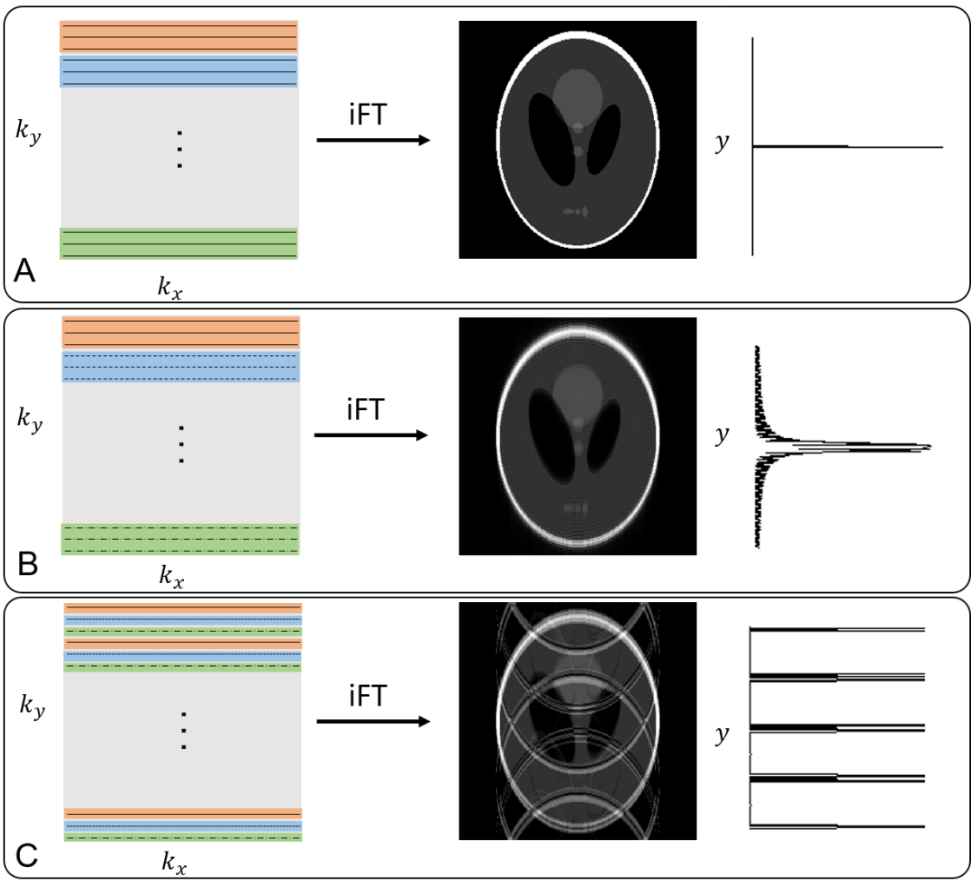

Figure 1.1. Illustration of segmented acquisition and motion artifacts. (A) Segments of the k-space (color-coded) are sampled potentially at different times and the data are combined to reconstruct the image via inverse Fourier Transform. (B) When incremental translations in the y-direction occur between sampling of the different k-space segments, the reconstructed image contains blurriness. (C) When k-space is sampled with an interleaved order and the same motion as in (B) occurs, the reconstructed image contains ghosting artifacts. The point spread functions are shown in the right column showing the effects of the motion on the images.

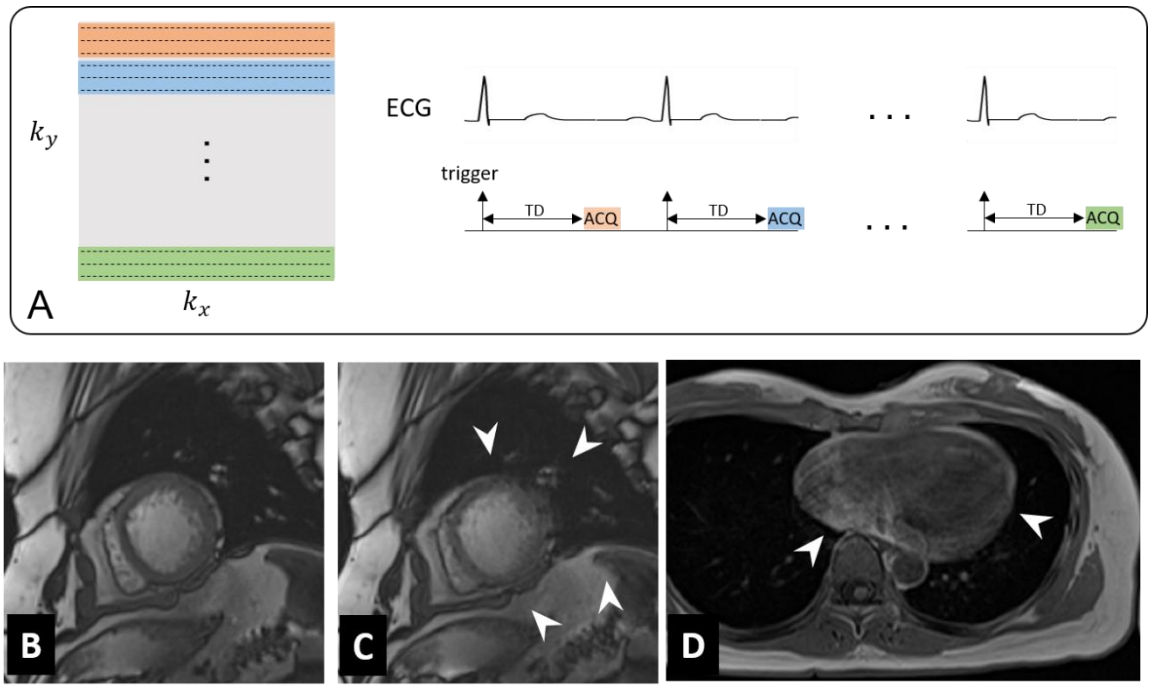

Figure 1.2. Illustration of ECG triggered acquisition and artifacts in cardic MRI. (A) k-Space segments are acquired with the same delay time relative to the ECG triggers. (B) A short-axis diastolic image acquired with ECG triggering and breath-hold. The image is artifact-free. (C) A short-axis diastolic image acquired with imperfect breath-hold. The image is blurry (arrows) due to breathing motion. (D) An axial image acquired with breath-hold but no ECG triggering. Beating artifacts are present (arrows). (ECG: electrocardiography signal; TD: delay time; ACQ: data acquisition)

1.2 Myocardial strain imaging

Cardiovascular disease remains the leading cause of morbidity and mortality worldwide [4]. Disease of the heart is the most common type of cardiovascular disease. Assessing structural and functional abnormalities of the heart is crucial for diagnosing and managing patients with heart disease. Medical imaging techniques such as echocardiography (ECHO), computed tomography (CT), MRI and PET/SPECT are routinely used to non-invasively evaluate heart anatomy and quantify cardiac function [5]. The most widely used quantification of cardiac function is left ventricular ejection fraction (LVEF) which is defined as the ratio of end-systolic and end-diastolic ventricular volumes. LVEF depicts the percentage change in LV volume and has been used for diagnosis and treatment stratification in many diseases. However, LVEF does not always

reflect ventricular function change in conditions of subtle or subclinical tissue alteration. LVEF can overestimate systolic function in patients with hypertrophic myocardium [6]. LVEF only quantifies global cardiac function while regional function assessment may reflect regional and subtle changes better than global function measurements [7].

Myocardial strain imaging has emerged as an important technique to assess cardiac function [8]. Myocardial strain characterizes the contractility of the myocardium and can be calculated for multiple sectors of the ventricle and multiple time frames of the cardiac cycle. Recent studies have demonstrated that strain is superior to LVEF for assessing cardiac function in multiple heart disease populations [9-13]. For instance, global longitudinal strain (GLS) can better detect myocardial dysfunction in hypertrophic myocardium and heart failure with preserved ejection fraction [10, 13, 14]. GLS can predict mortalities in chronic or acute heart failure [11, 13]. Characterizing mechanical dyssynchrony of the myocardial contraction with regional strain predicts outcome of cardiac resynchronization therapy (CRT) and may be promising for optimizing CRT patient selection and implementation [15-19]. GLS can detect myocardial dysfunction in chemotherapy related cardiotoxicity earlier than LVEF [20, 21].

1.3 CMR strain methods

Although ECHO is the most frequently used cardiac imaging tool with its readily availability and quick imaging, it lacks the ability to provide diagnostic information in numerous conditions [22]. Cardiac MRI has emerged as the reference for cardiac imaging in both congenital and acquired heart disease [5, 23, 24]. CMR can provide comprehensive and versatile evaluation of the cardiac anatomy, function, metabolism, and blood flow in the great vessels [25, 26]. CMR has the unique ability to characterize tissue properties and thus is the tool of choice to assess myocardial scar, diffuse fibrosis and edema [23, 27]. CMR is also the gold standard to measure myocardial strain [28]. There are a number of existing MRI strain methods, including MR tagging [29, 30], harmonic phase (HARP) MRI [31], strain-encoded (SENC) imaging [32], feature tracking [33] and cine displacement-encoded stimulated echoes (cine DENSE) [34].

MR tag imaging creates spatial modulation of the magnetization at the beginning of the heart cycle in the forms of line tags or spatial tags. The tags deform along with the

myocardium contraction and relaxation. Myocardial displacement and subsequently strain are quantified by tracking the tags and interpolating the motion trajectories of the tracked tags or grids. MR tagging is a very reproducible method and considered the gold standard of myocardial strain imaging. However, the complicated and time-consuming post-processing hinders wide usage of the technique in clinical applications. The displacement estimation is also limited by the distance between line or grid tags. HARP MRI is an image processing method that attempts to simplify analysis of MR tagging images by applying a band-pass filter to the data and tracking motion of the tags on the synthetic HARP phase images. Yet, there is limited availability of the analysis software and the limitations of MR tagging still stand.

In SENC imaging [32], tag planes parallel to the image plane are created and two images with different z phase encodes are acquired for calculation of longitudinal strain maps on a short-axis slice. The method is capable of accurately measuring longitudinal strain. However, the information SENC can provide is limited. It does not provide strain components other than longitudinal strain, such as radial and circumferential strains. The method cannot be extended for 3D strain imaging. SENC imaging also requires prior knowledge of strain and tilt angles for choices of z-plane encoding frequencies. Without such prior information, the strain calculation may not be accurate.

Feature tracking is the MRI equivalent of speckle tracking with echocardiography. As a post-processing method, feature tracking utilizes routinely collected cine images and estimates myocardial displacement by identifying features in the images and tracking them in the consecutive frames. The major advantage of feature tracking is that no additional acquisition is required. However, it is prone to through-plane motion and the displacement measurement is limited by pixel size as it cannot detect motion smaller than the pixel size.

Cine DENSE is a well-established and dedicated strain imaging technique with MRI. Cine DENSE is accurate, reproducible and easy to process. With these properties, the clinical applications of cine DENSE are expanding. The method will be described in more detail in the following subsections.

1.4 Cine DENSE

Cine DENSE images myocardial displacement and strain by encoding the displacement into the phase of the imaging signals instead of tracking image features. Cine DENSE was rigorously validated in both phantom [35] and in-vivo studies against MR tagging and was proven highly accurate and reproducible [36, 37]. Recent studies have recognize cine DENSE as the reference of myocardial strain quantification [38]. With these properties, the applications of cine DENSE are expanding. Auger et al [18] showed in heart failure patients that cine DENSE can quantify late mechanical activation and predict CRT response. And imaging segmental strain and subsequently mechanical late activation delay can be used to guide therapy implementation. Mangion et al [39] showed the prognostic value of cine DENSE in acute myocardial infarction, and Jing et al [40] showed the detection of subclinical contractile dysfunction in childhood obesity. The following subsections will introduce the basics of cine DENSE data acquisition and image processing.

1.4.1. Pulse sequence and imaging signal

The pulse sequence for cine DENSE imaging is shown in Figure 1.3 [34, 41]. The sequence consists of two major modules: magnetization preparation for displacement encoding and readouts for data acquisition. Cine DENSE is ECG-triggered to place the displacement encoding module at end diastole and data acquisition is repeated for all the cardiac frames following the preparation pulses.

The displacement encoding module consists of two 90-degree RF pules with encoding gradients applied in between. The 90-degree RF pules are not spatially selective. At the end of the displacement encoding module, the longitudinal magnetization M_z is spatially modulated and can be expressed as,

$$M_z(x) = M\cos(2\pi k_e x), \qquad (1.6)$$

where k_e is the displacement encoding frequency in cyc/mm, M is the value of longitudinal magnetization right before application of the displacement encoding pulses, and the transverse magnetization is ideally zero.

For each readout of the data acquisition, an RF pulse is first applied, followed by a displacement-unencoding gradient of equal area with the encoding gradient. Afterward, the echo can be readout using Cartesian or non-Cartesian trajectories. According to Equation 1.4, the longitudinal magnetization before the RF pulse is,

$$M_z(x,t) = [M\cos(2\pi k_e x) - M_0]e^{-\frac{t}{T_1}} + M_0 \qquad (1.7)$$

where t is the time since the application of the displacement encoding module. After application of the RF pulse and the unencoding gradient, the transverse magnetization is,

$$M_{xy}(x,t) = \left\{[M\cos(2\pi k_e x) - M_0]e^{-\frac{t}{T_1}} + M_0\right\}\sin(\alpha)\, e^{-j2\pi k_e(x+\Delta x)}, \qquad (1.8)$$

where Δx is the local tissue displacement that has occurred since the application of displacement encoding module. By rewriting $\cos(k_e x)$ into its Eulerian form, Equation 1.8 becomes,

$$\begin{aligned} M_{xy}(x,t) = {} & \frac{M}{2}\sin(\alpha)\, e^{-\frac{t}{T_1}}e^{-j2\pi k_e \Delta x} \\ & + M_0\sin(\alpha)\,(1 - e^{-\frac{t}{T_1}})e^{-j2\pi k_e(x+\Delta x)} \\ & + \frac{M}{2}\sin(\alpha)\, e^{-\frac{t}{T_1}}e^{-j2\pi k_e \Delta x}e^{-j2\pi 2k_e x}. \end{aligned} \qquad (1.9)$$

There are three components in the imaging signal that correspond to three echoes centered at $k_x = 0, k_e, 2k_e$ respectively. The first echo is the desired stimulated-echo with its phase proportional to the tissue displacement. The second echo is the so-called T_1-relaxation echo, given its property of growing intensity with T_1-relaxation. And the third is a complex conjugate echo, which is outside of the imaging window with the parameters typically used and therefore neglected in the scope of this dissertation. The T_1-relaxation echo generates artifacts (strips) in the images and is problematic for cine DENSE imaging. Suppression of the T_1-relaxation echo is necessary.

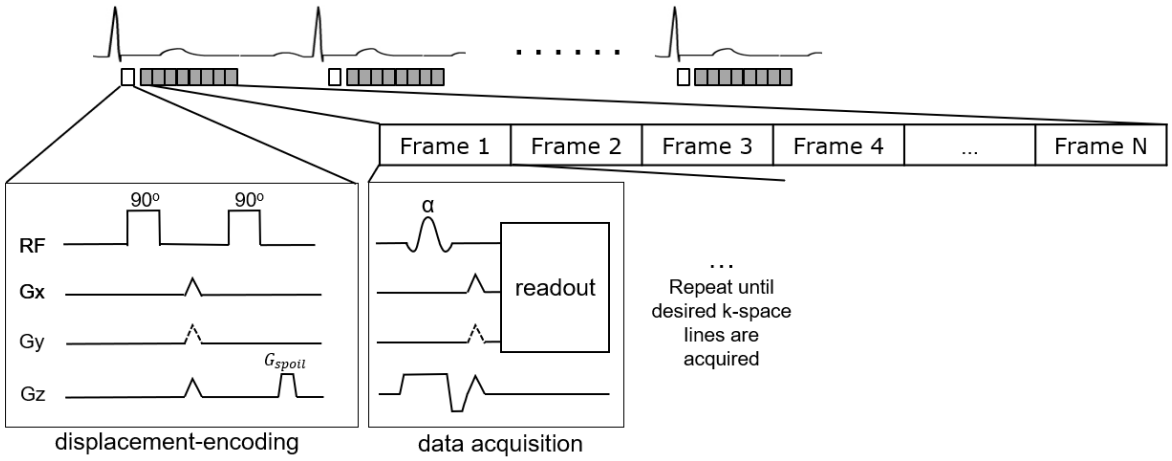

Figure 1.3. Pulse sequence of cine DENSE. Displacement encoding modules are applied after each ECG trigger and followed by multi-frame acquisition. The displacement encoding module consists of two 90-degree RF pulses with displacement encoding and through-plane dephasing gradients in between. The data acquisition uses segmented k-space coverage typically with a spiral trajectory. A data acquisition module consists of a slice-selective RF pulse, un-encoding, and through-plane dephasing gradients and readout gradients. The through-plane dephasing gradient in the data acquisition module is often combined with the slice-selective rephasing gradient to minimize the echo time, but shown separately in the diagram.

1.4.2. T_1-relaxation echo suppression

Two methods are often used in conjunction to effectively suppress the T_1-relaxation echo, complementary spatial modulation of magnetization [42], i.e. phase-cycling, and through-plane dephasing (TPD) [43].

With phase-cycling, an additional dataset is acquired separately with the phase of the second 90-degree RF pulse in the displacement encoding module incremented by 180 degrees. The transverse magnetizations of the two phase-cycled acquisitions are,

$$M_{xy}^1(x,t) = \frac{M}{2}\sin(\alpha)\, e^{-\frac{t}{T_1}} e^{-j2\pi k_e \Delta x} + M_0 \sin(\alpha)\,(1 - e^{-\frac{t}{T_1}}) e^{-j2\pi k_e (x+\Delta x)}, \qquad (1.10)$$

$$M_{xy}^2(x,t) = -\frac{M}{2}\sin(\alpha)\, e^{-\frac{t}{T_1}} e^{-j2\pi k_e \Delta x} + M_0 \sin(\alpha)\,(1 - e^{-\frac{t}{T_1}}) e^{-j2\pi k_e (x+\Delta x)} \qquad (1.11)$$

The sign of the stimulated-echo in the phase-cycled acquisition is negated. By subtracting the two phase-cyclings, the T_1-relaxation echo is canceled and the signal of the stimulated echo is doubled,

$$M_{xy}^{C}(x,t) = M\sin(\alpha)\, e^{-\frac{t}{T_1}} e^{-j2\pi k_e \Delta x} \qquad (1.12)$$

where M_{xy}^{C} indicates the isolated stimulated-echo with local tissue displacement encoded in the phase, $e^{-jk_e\Delta x}$.

The through-plane dephasing method selectively dephases the T_1-relaxation echo (and the complex conjugate echo in fact) with the use of a z gradient. As shown in Figure 1.3, a pair of gradients in the through-plane direction (G_z) are applied along with the in-plane encoding and unencoding gradients. With this method alone, the transverse magnetization in Equation 1.9 becomes,

$$\begin{aligned} M_{xy}(x,z,t) = {} & \frac{M}{2}\sin(\alpha)\, e^{-\frac{t}{T_1}} e^{-j2\pi k_e \Delta x} e^{-j2\pi k_d \Delta z} \\ & + M_0 \sin(\alpha)\,(1 - e^{-\frac{t}{T_1}}) e^{-j2\pi k_e (x+\Delta x)} e^{-j2\pi k_d (z+\Delta z)} \\ & + \frac{M}{2}\sin(\alpha)\, e^{-\frac{t}{T_1}} e^{-j2\pi k_e \Delta x} e^{-j2\pi 2k_e x} e^{-j2\pi k_d \Delta z} e^{-j2\pi 2k_d z}, \end{aligned} \qquad (1.13)$$

where k_d is the through-plane dephasing frequency with the same unit as k_e. This equation suggests that the T_1-relaxation and the complex conjugate echoes are centered at different locations (k_d and $2k_d$ respectively) from the stimulated echo in k_z-axis. Therefore, the complex conjugate echo is further away from the imaging window and the T_1-relaxation echo is dephased compared to Equation 1.9. The limitation of through-plane dephasing is signal-to-noise ratio loss due to intra-voxel dephasing at high dephasing frequencies [43].

The effectiveness of these two methods for suppressing the T_1-relaxation echo can be evaluated by calculating the contribution of the T_1-relaxation echo to the overall image energy [34, 43]. The lowest T_1-echo energy with preserved SNR was achieved with a combination of phase-cycling and through-plane dephasing with k_d of 0.08 cyc/mm. All the in-vivo cine DENSE imaging protocols in this dissertation are performed with these

two methods applied together. The use of through-plane dephasing also suppresses blood signal and generates black-blood images, as shown in Figure 1.4.

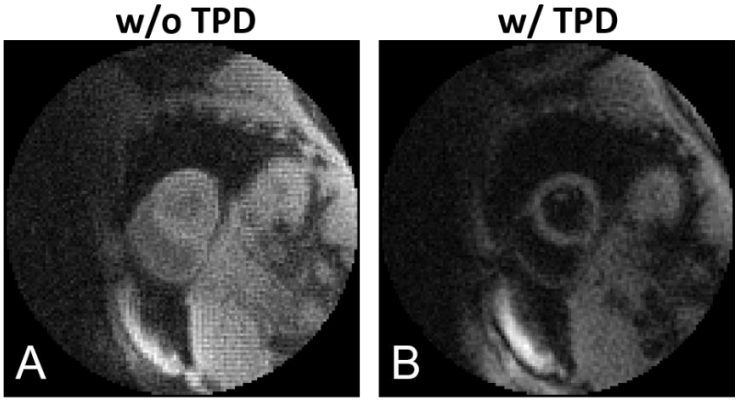

Figure 1.4. Through-plane dephasing in cine DENSE. (A) Cine DENSE image acquired without TPD. (B) Image acquired in the same subject and at the same cardiac frame with TPD. Striping artifacts are present in the image without TPD. TPD also has dark blood effect because blood has large intra-voxel motion and therefore the acquisition with TPD is black-blood. (TPD: through-plane dephasing)

1.4.3. Data acquisition

A segmented gradient echo sequence is typically used for data acquisition in cine DENSE, with either Cartesian [34] or spiral trajectories [41]. A spiral trajectory has the advantage of higher signal-to-noise ratio efficiency. For the rest of the dissertation, the use of a spiral trajectory is presumed.

1.4.4. Background phase correction

Similar to phase-contrast imaging methods, cine DENSE imaging relies on the phase of the imaging signal, which is also influenced by off-resonance effects such as B_0 inhomogeneity. The phase component related to such effects is often referred to as the background phase $\Delta\theta_b$, which has not been included in Equations 1.8-1.13. Compensating for $\Delta\theta_b$ is vital for accurate displacement and strain quantification.

A simple approach is to acquire a reference scan with displacement encoding frequency of zero. For the reference scan, the transverse magnetizations without and with displacement encoding are

$$M_{xy}^{C}(x,t)_{ref} = M\sin(\alpha)\, e^{-\frac{t}{T_1}} e^{-j\Delta\theta_b(x)} \quad (1.14)$$

$$M_{xy}^{C}(x,t) = M\sin(\alpha)\, e^{-\frac{t}{T_1}} e^{-j[2\pi k_e \Delta x + \Delta\theta_b(x)]} \quad (1.15)$$

Correction for the background phase is then performed by pixel-wise complex division. This method is also denoted as simple displacement encoding. When through-plane dephasing is utilized, the transverse magnetizations are:

$$M_{xy}^{C}(x,t)_{ref} = M\sin(\alpha)\, e^{-\frac{t}{T_1}} e^{-j[\Delta\theta_b(x) + 2\pi k_d \Delta z]} \quad (1.16)$$

$$M_{xy}^{C}(x,t) = M\,sin(\alpha)\, e^{-\frac{t}{T_1}} e^{-j[2\pi k_e \Delta x + \Delta\theta_b(x) + 2\pi k_d \Delta z]} \quad (1.17)$$

As shown in the equations, the through-plane motion induced phase $k_d \Delta z$ can be considered as "background phase" and removed along with $\Delta\theta_b$.

The background phase correction can also be performed with a balanced multidimensional encoding method where displacement is always applied in varying directions [44]. For 1D balanced encoding as an example, two scans are required with the encoding direction of the second scan the opposite of the first one. Therefore, the imaged phases of the two scans are $k_e \Delta x + \Delta\theta_b(x)$ and $-k_e \Delta x + \Delta\theta_b(x)$. The displacement phase can still be estimated from phase subtraction of the two scans but with a weighting factor of 2, i.e., $2k_e \Delta x$.

Regardless of the encoding methods, multiple scans are acquired to accurately estimate tissue displacement. As a generalized form for both simple and balanced encoding methods, the image phases of the scans can be described as a combination of displacement-encoded and background phases and as an encoding matrix (W). Solving the inverse of the matrix W produces the desired displacement phases. Zhong et al. described the comprehensive solutions for both encoding methods [44].

The data processing and reconstruction pipeline of cine DENSE is shown in Figure 1.5 with example data and images at a systolic frame. Within each encoding dimension, rawdata (in k-space) sets of the phase-cycled acquisitions are subtracted to remove the T_1-relaxation echo. Then the complex image is reconstructed from the post-subtraction k-space data via inverse Fourier Transform. Afterward, the true displacement phase image

is estimated with the images of multiple encoding dimensions. In the displacement phase image, the phase values in the beating heart reflect the displacements of the myocardium pixels while the phases in the static tissues such as the chest wall are trivial. In this example, two encoding dimensions are required to extract the 1D displacement. However, the pipeline applies to 2D and 3D imaging. A combined magnitude image is often obtained by averaging the magnitudes of all encoding dimensions.

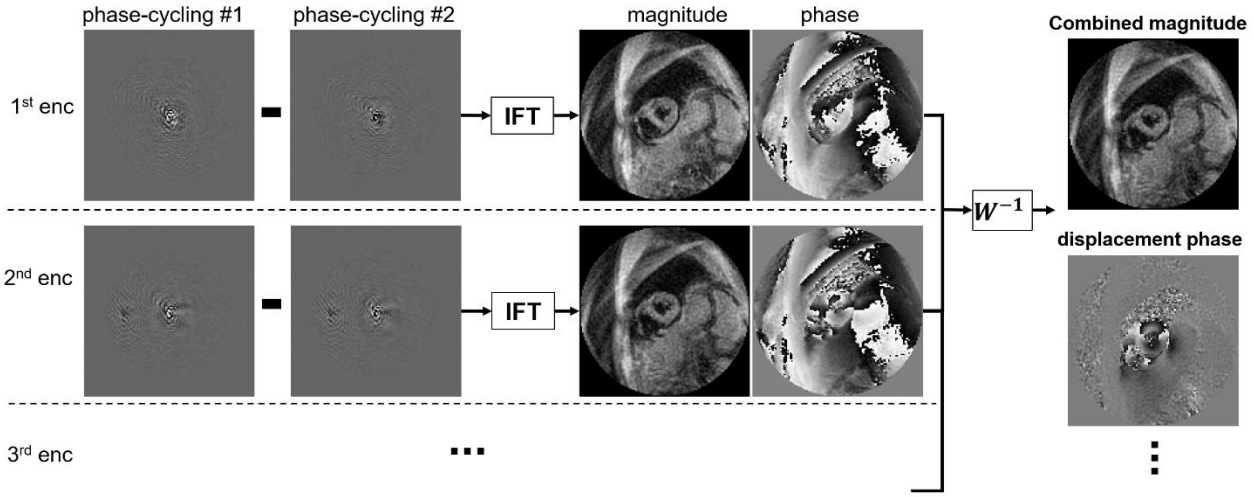

Figure 1.5. Pipeline of data processing and image reconstruction in cine DENSE. The phase-cycled k-space datasets are first subtracted to cancel the T_1-relaxation echo. The k-space data sets are complex values and the real part is shown in this example. Then complex images are reconstructed from the post-subtraction k-space with inverse Fourier Transform (IFT). Finally, the true displacement phase images are estimated from the images of multiple encoding dimensions. The example data shows a 1D simple encoding example with 2 scans required with the first encoding being the reference scan and the second encoding being displacement-encoded in the vertical direction. The displacement phase image is obtained by removing the background phase (as shown in the image of the first encoding) from the complex image of the second encoding. The pipeline extends to 2D and 3D imaging with the correct decoding matrix W^{-1}. (enc: encoding dimension)

1.4.5. Image analysis

Cine DENSE calculates strain based on the lagrangian definition as in the following equation,

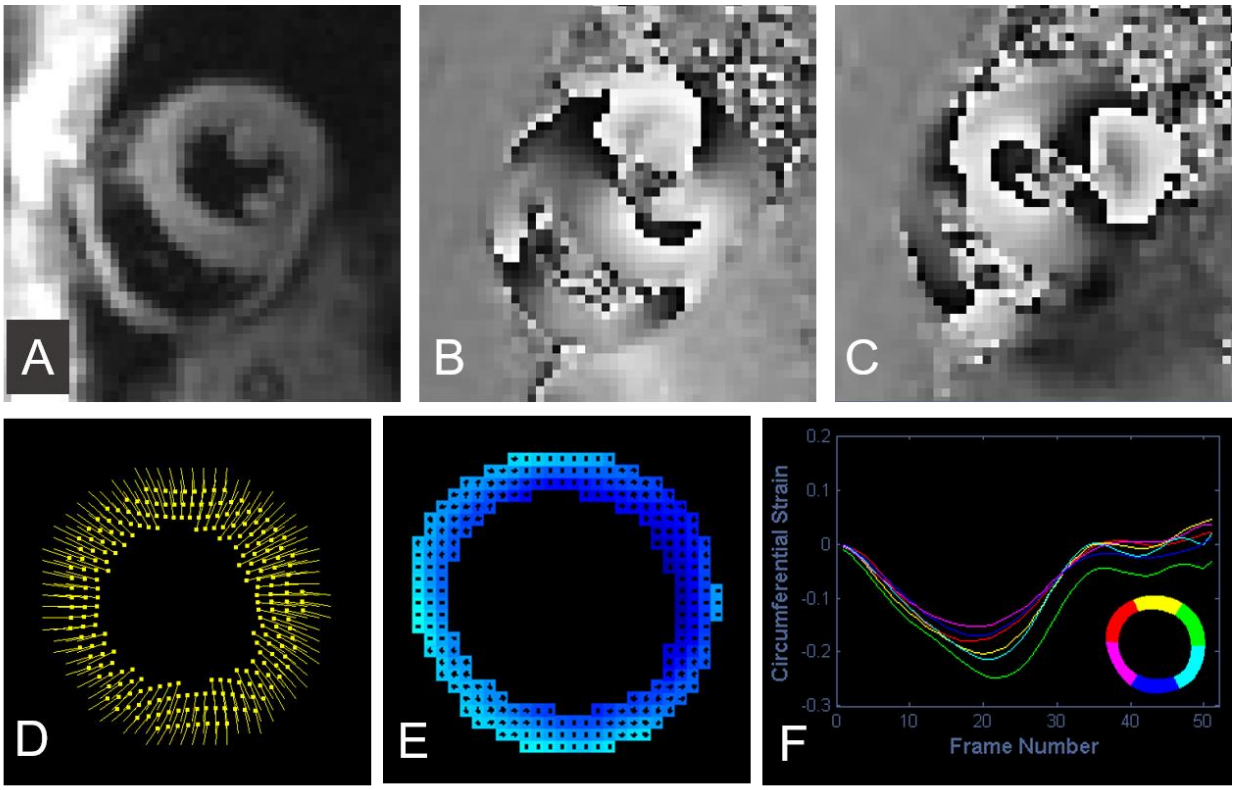

Figure 1.6. Example cine DENSE images at end-systole and segmental strains from a healthy subject. (A) Magnitude image. (B) Phase image with displacement-encoding in the vertical direction. (C) Phase image with displacement-encoding in the horizontal direction. The phase values in the myocardium reflect the tissue displacement in the two directions respectively. (D, E) Myocardial displacement field and circumferential strain map at the same frame. (F) Segmental circumferential strain curves in the imaged cardiac cycle.

$$\mathrm{E} = \frac{dL}{L_0}, \qquad (1.18)$$

where L_0 is the original length and dL is the change in length. To quantify the myocardial strain, the displacement phase images are processed with three major steps: myocardium segmentation, phase unwrapping, and strain calculation [45, 46]. With the motion-guided segmentation method, a myocardium region-of-interest of a single frame is manually defined and then automatically propagated onto the other frames. Then phase unwrapping is applied to the phase images to obtain the true phase values. The unwrapped phases are then directly converted into tissue displacement fields. Interpolation with the displacement fields estimates the motion trajectory of the pixels through the cardiac cycle. Then the myocardial strains can be calculated with the

trajectories for each frame and each myocardium pixel. The most commonly used strains are circumferential strain (E_{cc}) from short-axis imaging and longitudinal strain from long-axis imaging (E_{ll}) [41]. Figure 1.6 shows example results of cine DENSE imaging in a healthy subject. The two-dimensional tissue displacement (panel D) is calculated from the phase images in x- and y-directions (panels B, C). The derived circumferential strains show synchronous contraction of the heart with end-systolic E_{cc} of all segments in the range of -0.15 ~ -0.20 (panels D, E).

1.4.6. Additional technical aspects

As discussed previously, the tissue displacement estimation is relatively straightforward and simple in cine DENSE imaging. No tracking of image features is necessary for the processing. Therefore, measuring myocardial displacement in a certain cardiac frame does not depend on adjacent frames, unlike MR tagging and feature tracking. The method can be used for imaging a single frame or multiple frames. The tissue displacement estimation is not limited by the imaging spatial resolution and thus cine DENSE can be adapted to different applications and used to measure very fine tissue motion [47]. For myocardial strain imaging, higher encoding frequency provides better sensitivity of tissue motion but also induces more phase wrapping and signal loss due to intra-voxel dephasing especially during fast contraction and relaxation of the heart (such as early diastole). An encoding frequency around 0.10 cyc/mm is recommended.

Cine DENSE imaging uses stimulated-echoes, which results in halved imaging SNR [34, 48]. The image signal of the stimulated echo decays due to T1-relaxation, as shown in Equation 1.12. Therefore, the SNR decreases significantly with cardiac time, similarly to MR tagging. Variable flip angle has been employed to maintain the SNR in MR tagging and cine DENSE [49, 50]. Characteristics of SNR with different flip angle strategies have been investigated. A train of RF pulses with various flip angles with the end flip angle of 15 ~ 20 degrees produces optimal and constant SNR through the cardiac cycle [51]. Imaging at high magnetic fields, e.g. 3T, also improves the imaging SNR [51].

Fat signal has a lower resonance frequency than water and can create artifacts [3]. Fat saturation is often necessary in cardiac imaging to better visualize the heart anatomy and reduce artifacts from chemical shift. Typically, fat signal is selectively excited and saturated before application of the imaging pulses. Fat suppression is usually not feasible

in cine imaging due to the relatively longer RF pulses for fat signal saturation or spectrally selective selection. However, in cine DENSE, which is a stimulated-echo acquisition based imaging technique, fat suppression can be efficiently achieved by applying the fat saturation pulses before the displacement encoding pulses [52]. With this method, the recovered fat signal appears only in the T_1-relaxation echo and therefore is canceled with phase-cycling subtraction.

The stimulated-echo generation can be localized with a simple modification to the displacement-encoding module [53]. In the original cine DENSE sequence (Figure 1.3), the 90-degree RF pulses in the displacement encoding module are not spatially selective. By applying slice-selection to the two RF pulses in orthogonal directions in the imaging plane, the stimulated-echo would originate only from the rectangular region where the two slice profiles intersect. As a result, the cine DENSE images can be localized to the heart region by placing the field-of-view center over the heart center (Figure 1.7B). Localized generation of stimulated echo can be useful for accelerating the data acquisition [54, 55]. In cine DENSE, it is worth noting that the T_1-relaxation echo signal still originates from the entire imaging slice (Figure 1.7C).

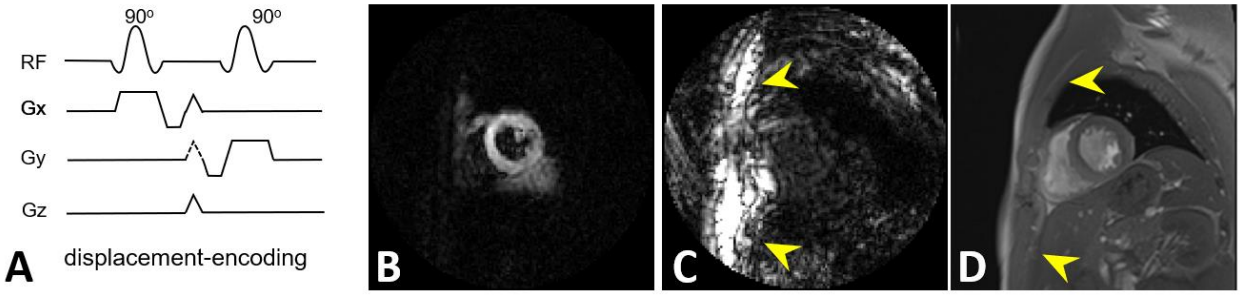

Figure 1.7. Cine DENSE with localized stimulated-echo generation. (A) The modified displacement encoding pulses localize stimulated-echo generation. The two 90-degree RF pulses are spatially selective in the two in-plane orthogonal directions. The data acquisition pulses are the same as previously described. (B) A cine DENSE image acquired with localized stimulated-echo generation. The stimulated-echo signal originates only in the region where the excitation profiles of the two RF pulses intersect, i.e. the heart region in this example. (C) The corresponding T_1-relaxation echo image reconstructed by summing the phase-cycled data. The T_1-relaxation echo signal still originates from the entire image slice. The T_1-relaxation echo is particularly strong in the chest wall (yellow arrows), likely due to closeness

to the receiver coils placed right above the chest and fast-relaxing fat signal. (D) The localizer image with gradient echo illustrating the anatomy of the imaging slice.

1.5 Respiratory motion compensation

Respiratory motion remains a major challenge for cardiac MRI. The simple and effective approach of breath-holding is often challenging or even not feasible in some patient populations such as heart failure, pediatrics and those under sedation. Performing multiple breath-holds can be taxing for patients and complicated for imaging technologists. Acquisitions with imperfect breath-holding are often repeated which further increase the imaging time. The typically feasible length of breath-hold limits the imaging resolution and spatial coverage. Free-breathing imaging methods are desirable for these reasons.

The existing free-breathing methods can be divided into two categories: diaphragm-navigator method (dNAV) and self-navigation. The following subsections will briefly discuss both methods. Real-time imaging [56, 57] is an alternative approach to reduce motion artifacts by restraining the acquisition of an image to a single short time window. While real-time imaging is feasible with reasonable resolutions, its ability to image at high resolutions or large spatial coverage may be limited. This dissertation focuses on discussing the compensation of respiratory motion for segmented acquisition other than real-time imaging.

1.5.1. Diaphragm navigator

The dNAV method monitors respiration motion by detecting the position of the diaphragm with a navigator echo [58, 59]. With this method, a 1D pencil beam navigator perpendicular to the lung-liver interface is positioned and acquired along with the imaging data (Figure 1.8A) [3]. dNAV data is often acquired right before or after acquisitions of the imaging data, depending on the specific applications. dNAV acquisition is typically applied with an accept/reject strategy to reduce respiratory artifacts, where data are accepted when the diaphragm position is at a certain respiratory phase, often end-expiration (green box, Figure 1.8B) and otherwise rejected. This diaphragm navigator based accept/reject strategy is often referred to as dNAV-gating.

The dNAV-gating method has been applied to many MR imaging applications and proven to reduce motion artifacts. However, there are several limitations. This method requires scout scans to set up the dNAV position and acceptance window parameters, which usually takes 2-3 trials. The imaging efficiency is significantly reduced (~35%). The motion pattern of the diaphragm with respiration varies from subject to subject and the same acceptance window corresponds to various imaging efficiency and the amount of motion in the accepted imaging data [60, 61]. A 1D navigator is not sufficient to reflect the motion of the heart due to respiration. Therefore, the dNAV method often results in variable image quality. The navigator positions cannot be used to correct for motion in the image plane and therefore is limited to accept/reject strategy. Acquisition of dNAVs disturbs signal and creates dark bands in the liver region which is problematic for liver imaging. The dNAV method is not compatible with imaging with continuous acquisitions such as cine SSFP with retrospective ECG-gating. The dNAV acquisition would interrupt the steady-state of the imaging signal and the dNAV can only track heart motion at limited temporal resolution.

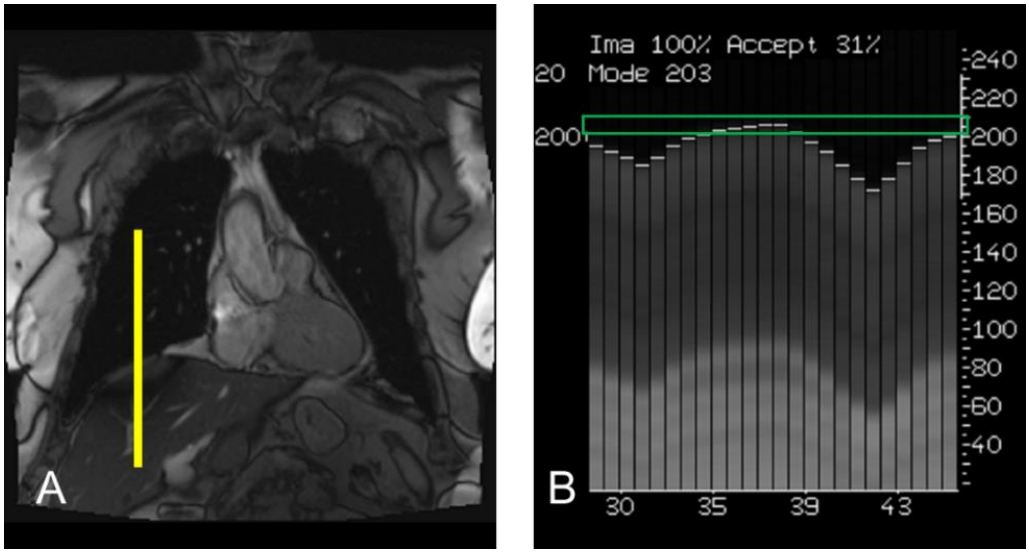

Figure 1.8. Illustration of dNAV-gating. (A) The pencil beam navigator is positioned over the lung-liver interface to track the motion of the right hemi-diaphragm in the superior-inferior direction. (B) Diaphragm positions indicating the respiration of the subject. The navigators were acquired once per heartbeat in this example. An acceptance window is set at end-expiration (green box).

1.5.2. Self-navigation

Self-navigation methods typically compensate for respiration artifacts with the motion information extracted from the imaging data without using diaphragm navigators.

With self-navigation methods, respiratory motion estimation is performed either in the image domain using image registration methods or the k-space domain with feature extraction methods. For the case of image domain motion estimation, intermediate images are often reconstructed by combining consecutively acquired data and used as navigators, termed image-based navigators (iNAV). These iNAVs are often lower spatial and/or temporal resolutions than the desired images. Registration on these iNAVs provides an estimation of the motion of the heart due to respiration. Motion estimation with iNAVs was first introduced for free-breathing MR angiography [62, 63] and then cine imaging [64, 65]. For example, Sussman et al. reconstructed real-time low spatial resolution images with central k-space data as iNAVs and estimated the motion information using cross-correlation [62]. Leung et al. combined data of cardiac frames to reconstruct one iNAV image per heartbeat and estimated the respiratory motion from heartbeat to heartbeat using registration methods [65]. For motion estimation with k-space rawdata, a portion of the k-space, either the center or the central lines, is often acquired repeatedly. The temporal profiles of these data reflect changes induced by motion. Spectral analysis or feature extraction, such as principal component analysis, with the temporal profile can be used to estimate the respiratory motion. For example, Liu et al. developed a self-navigation method for 3D cine imaging [66]. In this method, a stack of star trajectory is used and each k-space segment contains the same k-space center line in the z-direction. Fourier transform of the kz line provides a projection of the image. The motion signal of the free-breathing acquisition is then estimated by calculating the center of mass of the projections. In another study, Feng et al. estimated the cardiac motion and respiratory motion using filters with repeatedly sampled k-space center data in cine imaging [67]. The band-pass filters were designed based on the prior that cardiac and respiratory motions have different frequency ranges, 0.5-2.5 and 0.1-0.5 Hz, respectively. Alternatively, correlation analysis with coil array data can also produce an estimation of the respiratory states [68].

There are numerous approaches to compensate for respiratory motion with self-navigation. The first method is an accept/reject gating strategy similar to that in the dNAV method [69]. By defining the common positions, i.e. the mode, typically at end-expiration of the respiratory positions [66] and accepting data within a window around the mode, the breathing artifacts can be reduced. To use such a gating strategy, motion estimation in 1D is typically used and usually performed for the superior-inferior direction. The gating method was proven to reduce artifacts in multiple applications but with reduced imaging efficiency.

The second method is to apply correction in k-space with the estimated motion information. Compensation for rigid motion has an explicit mathematical solution [70]. According to the Fourier transform relations, translation in image domain corresponds to a linear phase in the k-space domain and rotation in image domain corresponds to rotation in the k-space domain. 2D rigid motion correction in k-space can be summarized as the following equations [65]. The coordinates of the transformed image, x', y' can be expressed with the coordinates of the original image, x, y, as,

$$\begin{bmatrix} x' \\ y' \end{bmatrix} = \begin{bmatrix} \cos(\theta) & -\sin(\theta) \\ \sin(\theta) & \cos(\theta) \end{bmatrix} \begin{bmatrix} S_x & 0 \\ 0 & S_y \end{bmatrix} \begin{bmatrix} 1 & S_{xy} \\ 0 & 1 \end{bmatrix} \begin{bmatrix} x \\ y \end{bmatrix}$$

$$= \boldsymbol{A} \begin{bmatrix} x \\ y \end{bmatrix} + \begin{bmatrix} t_x \\ t_y \end{bmatrix} \quad (1.19)$$

where θ is the rotation angle, S_x, S_y are scaling factors, and S_{xy} is the shear parameter. Matrix $\boldsymbol{A}$ indicates the affine motion matrix and t_x, t_y are the in-plane translations. These parameters can be estimated from image registration algorithms. Correspondingly, compensation in k-space needs to first warp the k-space trajectory with,

$$\begin{bmatrix} k_x' \\ k_y' \end{bmatrix} = \boldsymbol{A}^{-T} \begin{bmatrix} k_x \\ k_y \end{bmatrix} \quad (1.20)$$

where k_x, k_y are the original k-space coordinates and k_x', k_y' are the corrected k-space coordinates. Then the k-space data are modified with,

$$d'(k_x', k_y') = \frac{e^{j2\pi\left(k_x' t_x + k_y' t_y\right)}}{\det(\boldsymbol{A})} d(k_x, k_y) \quad (1.21)$$

where $d(k_x, k_y)$ is the original k-space data and $d'(k'_x, k'_y)$ is the corrected k-space data. This model extends to 3D correction [70, 71].

Many studies have proven that this k-space rigid motion compensation method can effectively reduce artifacts due to motion [65, 71-74]. Figure 1.9 shows an example MRI image from a free-breathing acquisition comparing the reconstructions without (panel A) and with (panel B) translation correction. It is clear that simple translation correction reduces the blurriness in the image and provides a better definition of the myocardium borders. Correction in k-space for the in-plane motion allows the reconstruction to utilize more motion-corrupted imaging data and therefore improve imaging efficiency to as high as 100% in some applications [71, 74-76]. The explicit k-space correction is, however, limited to rigid motion. The in-plane motion due to respiration is non-rigid since the motion of different tissue varies. Compensation for non-rigid motion is less intuitive. Therefore, rigid motion estimation often requires a region-of-interest reduced to heart region using a manually defined spatial mask [64, 71, 74] or other methods [77].

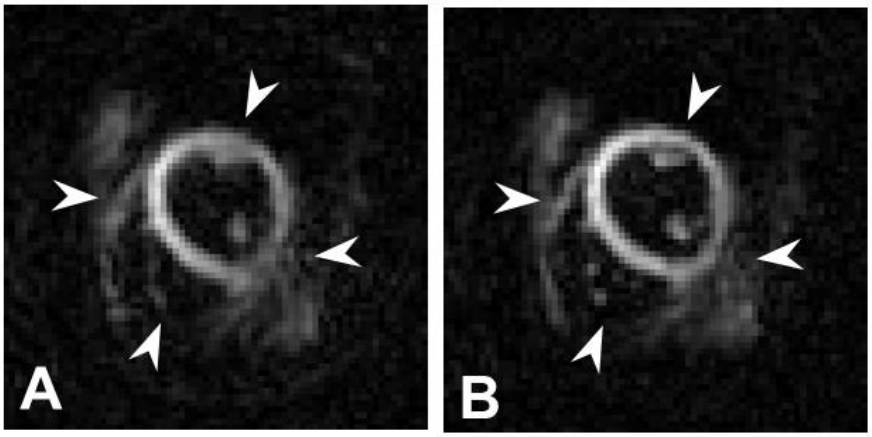

Figure 1.9. Demonstration of k-space rigid motion correction. (A) Reconstruction without translation correction contains blurriness (arrows). (B) Reconstruction of the same data with 2D in-plane translation correction. The acquisition was for multiple cardiac frames and a single diastolic frame is shown. Intermediate iNAVs were used to estimate the in-plane translations. k-Space correction reduces blurriness.

A third approach to compensate respiratory motion is adaptive imaging [69, 78]. While self-navigated motion correction is often performed retrospectively after the acquisition is done, it may be beneficial to prospectively reduce motion artifacts by

detecting respiratory motion in real-time and re-acquire motion corrupted k-space data [62, 79, 80]. Sachs et al. first introduced a diminishing variance algorithm (DVA) motion reduction in real-time [79]. The DVA algorithm used a navigator echo to monitor motion and, instead of gating, the algorithm calculated the distribution and variance of the navigator positions as data quality for each frame. Less variance of the dNAV indicated less motion within the frame. Then the algorithm repeated the acquisition of the frame that had the most variance, i.e. least quality. DVA eliminated the necessity of a predefined acceptance window and processed calculations in real-time. Similary, Sussman et al. developed an adaptive imaging method with iNAV-based motion detection for coronary artery imaging [62]. In this study, low-resolution iNAVs were reconstructed and their correlation coefficients with the template image were calculated as the motion information. Small correlation coefficients indicated large motion. Then the acquisition always reacquires the k-space data corresponded to the smallest correlation coefficient until the variance of the correlation coefficients of all data was smaller than a threshold. Such adaptive imaging methods can prospectively eliminate severely corrupted k-space data.

The different motion estimation and compensation methods can be used in conjunction or multiple times. Pang et al. proposed a free-breathing framework for MR angiography [75]. In the framework, the respiratory positions are firstly estimated from the repeatedly sampled k-space central line and used to bin all the rawdata into different motion states based on the respiratory positions. Intermediate images are reconstructed for each motion state and used to estimate the 3D motion of the heart due to respiration. Motion correction is then applied in k-space before reconstruction of the compensated free-breathing images. Similarly, Usman et al. proposed a framework with two-step of motion estimation for free-breathing dynamic MRI [76]. In this study, iNAVs are first reconstructed to estimate the heartbeat-to-heartbeat translations, k-space data are binned into several respiratory states accordingly and preliminary images of the different motion states are reconstructed for finer motion estimation and correction.

Overall, self-navigation methods are advantageous compared to dNAV. Self-navigated motion estimation is data-driven and usually does not require extra data acquisition or set-up. Self-navigation methods directly provide motion of heart due to respiration. The ability to apply data correction significantly improves imaging efficiency.

Self-navigation is particularly suitable for non-Cartesian sampling trajectories because of their greater sampling densities near the center of the k-space. For example, the central k-space data acquired with a dual density spiral trajectory is fully-sampled and provides a low-resolution iNAV. The k-space center for a radial trajectory is sampled with every readout. Non-Cartesian data acquisitions with trajectory rotation in time facilitates reconstruction of iNAVs as data of consecutive time points generate fully-sampled intermediate k-spaces and images.

1.6 Free-breathing cine DENSE

Conventionally, cine DENSE requires breath-holding for acquisition, which is a major limitation. The imaging time of cine DENSE is relatively long with the phase-cycling acquisition and multiple encoding dimensions. Usage of a spiral trajectory improve the SNR efficiency over imaging with an EPI trajectory. Yet, the total length of a typical cine DENSE imaging with 1D encoding is 14 heartbeats and two breath-holds are required for each slice. Requirement of multiple breath-holds is a major challenge as many patients have reduced capacities of performing breath-holds [81].

Previously, the dNAV method was applied to enable free-breathing cine DENSE imaging [41, 82]. However, dNAV is not ideal and the image quality varies due to the reasons described in the previous sections. A reliable self-navigated method is desirable. Cine DENSE imaging typically uses a segmented spiral trajectory for data acquisition and therefore it may be suitable to use iNAV-based motion estimation and correction methods. The challenges may lie in the artifact sources unique to cine DENSE imaging.

Overall there are three major types of artifacts in free-breathing cine DENSE: striping artifacts due to the residual T_1-echo, blurring and signal cancellation (Figure 1.10). Striping artifacts and blurring are due to inter-heartbeat respiratory motion and signal cancellation is due to intra-heartbeat motion. The motion that occurs during each readout is neglected in the scope of this dissertation.

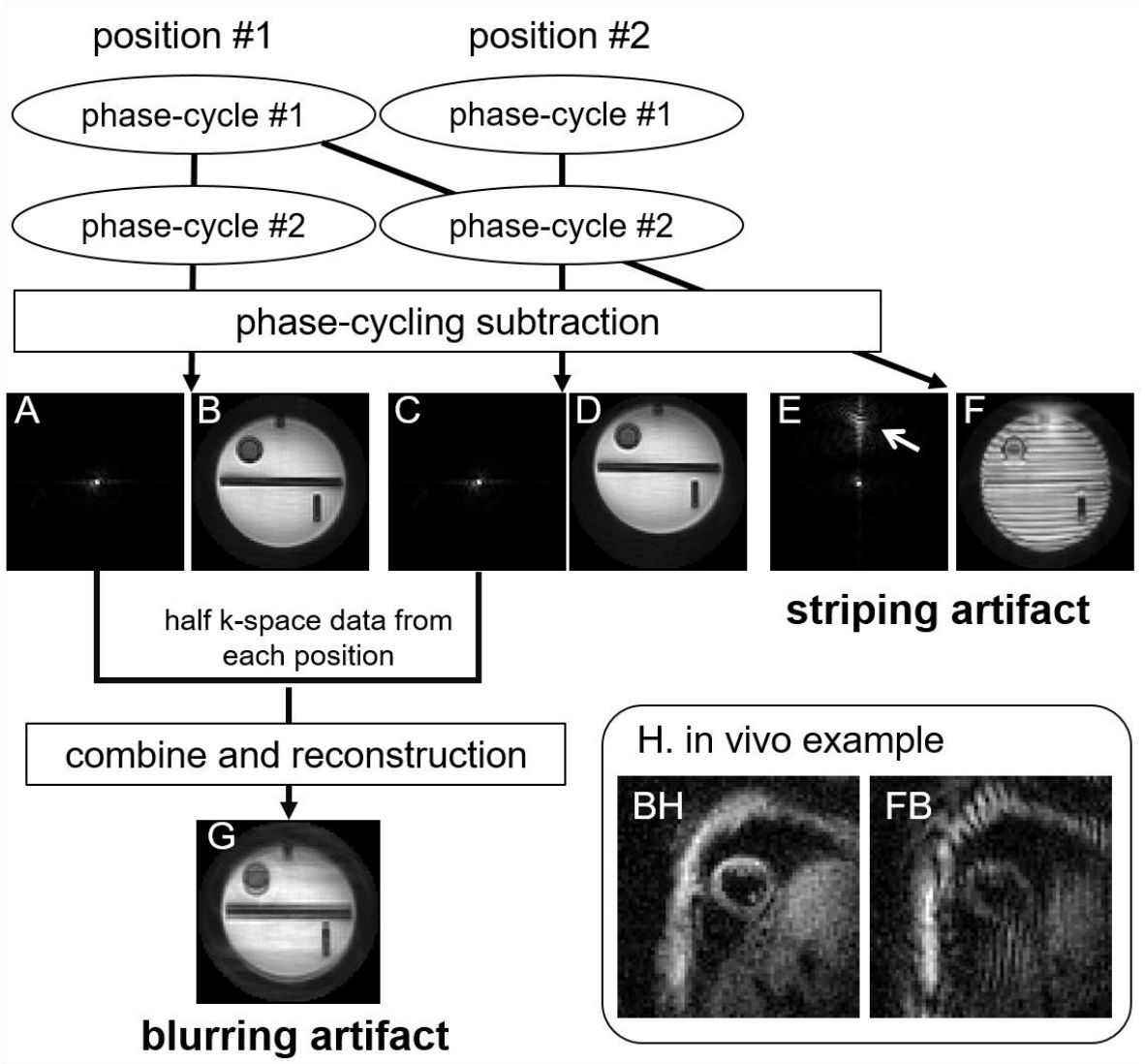

Figure 1.10. Demonstration of striping and blurring artifacts in free-breathing cine DENSE. In this experiment, fully-sampled cine DENSE images were acquired with the phantom located at position 1 and also at position 2. Motion, simulated by combining phase-cycling pairs from positions 1 and 2, induces insufficient suppression of the T_1-relaxation echo (panel E, white arrow) and corresponding striping artifacts in the images (panel F). If phase-cycled data at matched positions are subtracted (panels A, C), but motion occurs between k-space segments after sufficient suppression of the T_1-relaxation echo (panel B, D), then blurring artifact occurs when combining data from different segments (panel G). In this example, half of the k-space data was taken from each of the two positions. In vivo example images demonstrating both blurring and striping artifacts due to respiratory motion are also shown (panel H). (BH: breath-hold; FB: free-breathing)

With inter-heartbeat motion, the suppression of the T_1-relaxation echo is not effective. Therefore, strong residual signal of the T_1-echo may exist and cause striping artifacts. The inter-heartbeat motion also causes inconsistencies in the stimulated-echo signal and blurring as in other MRI applications. Figure 1.10 demonstrates both striping and blurring artifacts using spiral cine DENSE data acquired from a phantom placed at two different positions. Subtraction of phase-cycled data acquired at mismatched positions leads to a strong residual T_1-relaxation echo in the k-space (panel E) and striping artifacts in the corresponding image (panel F). After subtraction of phase-cycled data from matched positions, image reconstruction that combines post-subtraction stimulated echoes from different positions leads to blurring (panel G). These types of artifacts are observed in in-vivo cine DENSE images as shown in panel H.

Besides inter-heartbeat motion, intra-heartbeat motion also occurs. The bulk motion of the heart due to respiration is simultaneously encoded into the phase of the stimulated echoes, along with the contraction and relaxation of the myocardium. With rigid translation ($\vec{T} = (T_x, T_y, T_z)$) that occurs from the application of the DENSE preparation pulses to the data acquisition of a frame, the imaging signal in Equation 1.15 becomes,

$$M_{xy}^{C}(x, y, t, s) = M \sin(\alpha)\, e^{-\frac{t}{T_1}} e^{-j\left[2\pi(k_e^x \Delta x + k_e^y \Delta y + k_d \Delta z) + \Delta\theta_b(x)\right]} e^{-j2\pi[k_e^x T_x + k_e^y T_y + k_d T_z]} \quad (1.22)$$

where k_e^x and k_e^y are the displacement encoding frequencies applied in x- and y-directions, k_d indicates the through-plane dephasing frequency, and s is the index of the k-space segment. The equation is generalized for any displacement encoding directions. The additional phase term,

$$e^{-j2\pi[k_e^x T_x + k_e^y T_y + k_d T_z]}, \quad (1.23)$$

is the collective consequence of translations of the heart due to respiration.

With free-breathing, the motion $\vec{T}$ is very likely to vary from heartbeat to heartbeat, which causes different breathing-induced phases in different k-space segments. As a result, signal cancellation artifacts can occur when the k-space segments are combined for final image reconstruction, particularly when two k-space segments are acquired

during respiration phases that lead to opposite signs of $\vec{T}$ (for example, inspiration vs. expiration). Such signal cancellation artifacts due to phase variations have been investigated in diffusion weighted imaging (DWI) where a pair of gradients with large moments are used and thus sensitive to motion [2, 83]. The extra phase due to intra-heartbeat motion can also leads to errors in the displacement phase images and subsequently in displacement and strain quantification. As shown in Figure 1.11, the free-breathing acquisition by dNAV had both reduced magnitudes and phase errors due to the intra-heartbeat motion (panels C, D). These artifacts lead to errors in the displacement phases and the estimated displacement fields (panels G, J).

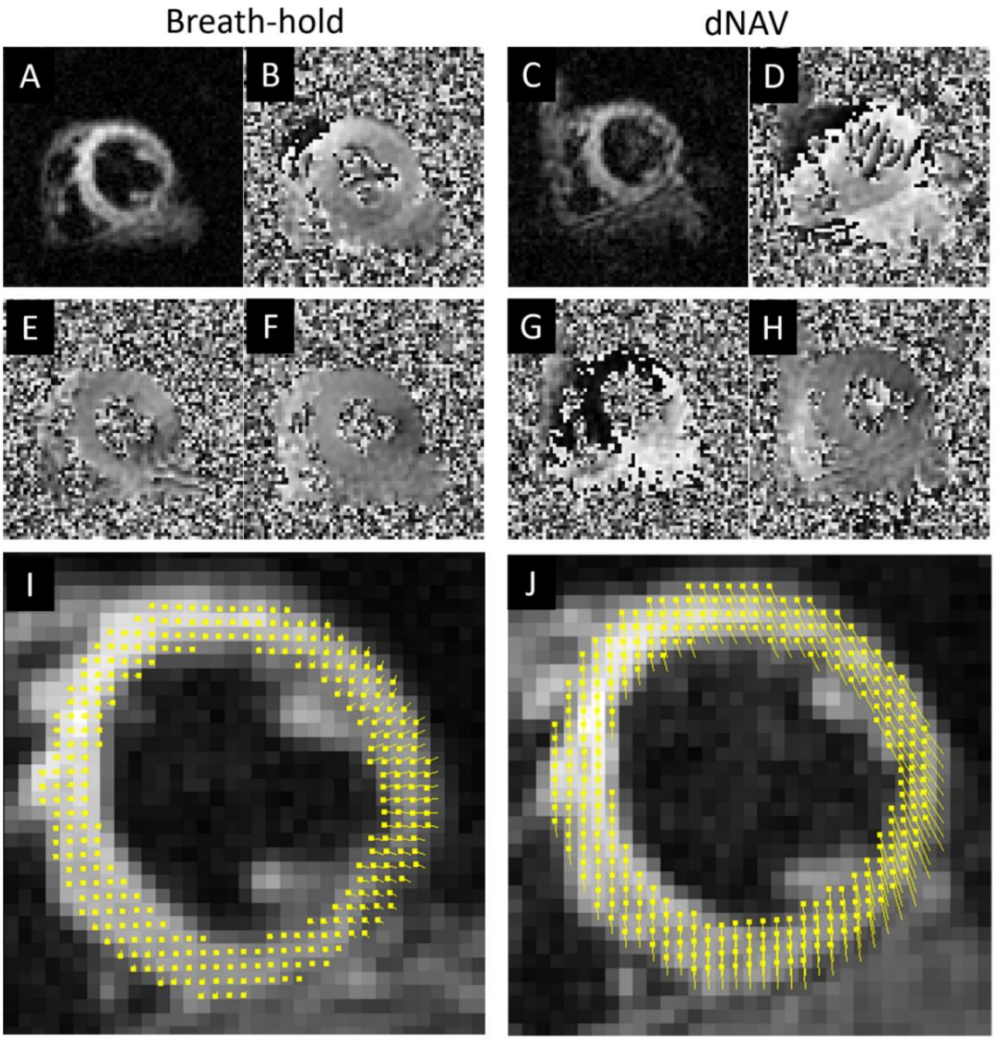

Figure 1.11. Demonstration of intra-heartbeat motion induced phase errors. Results of a late diastolic frame are shown acquired with breath-hold (left) and free-breathing by dNAV

(right). (A-D) Images of the third encoding dimension in balanced 2D encoding. Compared to the breath-hold images, the images of dNAV have reduced magnitudes (C vs. A) and elevated phases (D vs. B) due to intra-heartbeat motion. (E-H) Displacement phase images. The displacement phases of breath-hold are overall small as expected at late-diastole. However, the displacement phases of dNAV in the x-direction have significant errors (G vs. E). (I, J) Estimated 2D displacement fields. Bulk motion due to the intra-heartbeat motion induced phase errors (G) is observed in the dNAV displacement field. (dNAV: diaphragm navigator-based gating)

1.7 Scope of the dissertation

This dissertation focuses on developing self-navigated methods that compensate for the major artifact sources in free-breathing cine DENSE. The specific aims are (1) to develop a self-navigation reconstruction framework that suppresses the artifacts due to inter-heartbeat motion; (2) to develop an adaptive acquisition algorithm that can prospectively reduce the residual T_1-echo and a phase correction to compensate for the intra-heartbeat motion; (3) to evaluate the self-navigated method in vivo. The next few Chapters will discuss the studies performed for these three aims.

Chapter 2 presents a framework to compensate for striping and blurring artifacts due to the inter-heartbeat breathing motion during image reconstruction. The framework first performs a match-making process to identify phase-cycling pairs acquired at similar respiratory positions to reduce striping artifacts. The matched phase-cycling pairs are identified as those with minimal residual T_1-echo energy (rT1E). Subsequently, after subtraction of the matched phase-cycling pairs, image-based navigators of the stimulated echoes are reconstructed for motion estimation and correction in k-space. The framework was demonstrated in both phantom and in vivo.

Chapter 3 describes an adaptive imaging algorithm that uses the rT1E to guide data acquisition in real-time. The algorithm aims to reduce the overall rT1E both efficiently and effectively by always repeating the k-space segment with the highest rT1E. Signal cancellation due to intra-heartbeat motion is also investigated and corrected with a phase correction method. The algorithm was investigated in healthy subjects and the stopping criteria values were determined.

Chapter 4 evaluates the self-navigated free-breathing cine DENSE method (self-NAV) in both healthy subjects and patients with heart disease and compares self-NAV with the conventional dNAV-gating method. Cine DENSE datasets are acquired on each subject with breath-holding, dNAV-gating, and self-NAV. Free-breathing acquisitions are repeated once. The image quality and rT1E are calculated for each dataset. The agreement of free-breathing strain with breath-hold strain and the intra-session reproducibility of free-breathing strain are compared between self-NAV and dNAV methods.

Chapter 5 discusses the overall accomplishments, findings, limitations, and future directions of this dissertation project.

1.8 References

1. Liang, Z.-P. and P.C. Lauterbur, *Principles of magnetic resonance imaging: a signal processing perspective*. 2000: SPIE Optical Engineering Press.
2. Bernstein, M.A., K.F. King, and X.J. Zhou, *Handbook of MRI pulse sequences*. 2004: Elsevier.
3. Brown, R.W., et al., *Magnetic resonance imaging: physical principles and sequence design*. 2014: John Wiley & Sons.
4. Benjamin, E.J., et al., *Heart disease and stroke statistics—2018 update: a report from the American Heart Association.* Circulation, 2018. **137**(12): p. e67-e492.
5. de Roos, A. and C.B. Higgins, *Cardiac radiology: Centenary review.* Radiology, 2014. **273**(2S): p. S142-S159.
6. Kalam, K., P. Otahal, and T.H. Marwick, *Prognostic implications of global LV dysfunction: a systematic review and meta-analysis of global longitudinal strain and ejection fraction.* Heart, 2014. **100**(21): p. 1673-1680.
7. Chitiboi, T. and L. Axel, *Magnetic resonance imaging of myocardial strain: a review of current approaches.* Journal of Magnetic Resonance Imaging, 2017. **46**(5): p. 1263-1280.
8. Sutherland, G.R., et al., *Strain and strain rate imaging: a new clinical approach to quantifying regional myocardial function.* Journal of the American Society of Echocardiography, 2004. **17**(7): p. 788-802.
9. Cho, G.-Y., et al., *Global 2-dimensional strain as a new prognosticator in patients with heart failure.* Journal of the American College of Cardiology, 2009. **54**(7): p. 618-624.
10. Kraigher-Krainer, E., et al., *Impaired systolic function by strain imaging in heart failure with preserved ejection fraction.* Journal of the American College of Cardiology, 2014. **63**(5): p. 447-456.
11. Motoki, H., et al., *Incremental prognostic value of assessing left ventricular myocardial mechanics in patients with chronic systolic heart failure.* Journal of the American College of Cardiology, 2012. **60**(20): p. 2074-2081.
12. Sengeløv, M., et al., *Global longitudinal strain is a superior predictor of all-cause mortality in heart failure with reduced ejection fraction.* JACC: Cardiovascular Imaging, 2015. **8**(12): p. 1351-1359.
13. Park, J.J., et al., *Global longitudinal strain to predict mortality in patients with acute heart failure.* Journal of the American College of Cardiology, 2018. **71**(18): p. 1947-1957.

14. Smiseth, O.A., et al., *Myocardial strain imaging: how useful is it in clinical decision making?* European heart journal, 2015. **37**(15): p. 1196-1207.
15. Lardo, A.C., T.P. Abraham, and D.A. Kass, *Magnetic resonance imaging assessment of ventricular dyssynchrony: current and emerging concepts.* Journal of the American College of Cardiology, 2005. **46**(12): p. 2223-2228.
16. Bilchick, K.C., et al., *Cardiac magnetic resonance assessment of dyssynchrony and myocardial scar predicts function class improvement following cardiac resynchronization therapy.* JACC: Cardiovascular Imaging, 2008. **1**(5): p. 561-568.
17. Bilchick, K.C., et al., *Impact of mechanical activation, scar, and electrical timing on cardiac resynchronization therapy response and clinical outcomes.* Journal of the American College of Cardiology, 2014. **63**(16): p. 1657-1666.
18. Auger, D.A., et al., *Imaging left‐ventricular mechanical activation in heart failure patients using cine DENSE MRI: Validation and implications for cardiac resynchronization therapy.* Journal of Magnetic Resonance Imaging, 2017.
19. Delgado, V., et al., *Relative merits of left ventricular dyssynchrony, left ventricular lead position, and myocardial scar to predict long-term survival of ischemic heart failure patients undergoing cardiac resynchronization therapy.* Circulation, 2011. **123**(1): p. 70-78.
20. Thavendiranathan, P., et al., *Use of myocardial strain imaging by echocardiography for the early detection of cardiotoxicity in patients during and after cancer chemotherapy: a systematic review.* Journal of the American College of Cardiology, 2014. **63**(25): p. 2751-2768.
21. Plana, J.C., et al., *Expert consensus for multimodality imaging evaluation of adult patients during and after cancer therapy: a report from the American Society of Echocardiography and the European Association of Cardiovascular Imaging.* European Heart Journal–Cardiovascular Imaging, 2014. **15**(10): p. 1063-1093.
22. Friedrich, M.G. and F. Marcotte, *Cardiac magnetic resonance assessment of myocarditis.* Circulation: Cardiovascular Imaging, 2013. **6**(5): p. 833-839.
23. Hundley, W.G., et al., *ACCF/ACR/AHA/NASCI/SCMR 2010 expert consensus document on cardiovascular magnetic resonance: a report of the American College of Cardiology Foundation Task Force on Expert Consensus Documents.* Journal of the American College of Cardiology, 2010. **55**(23): p. 2614-2662.

24. Kilner, P.J., et al., *Recommendations for cardiovascular magnetic resonance in adults with congenital heart disease from the respective working groups of the European Society of Cardiology.* European heart journal, 2010. **31**(7): p. 794-805.

25. Pennell, D.J., et al., *Clinical indications for cardiovascular magnetic resonance (CMR): Consensus Panel report.* Journal of Cardiovascular Magnetic Resonance, 2004. **6**(4): p. 727-765.

26. Bellenger, N., et al., *Comparison of left ventricular ejection fraction and volumes in heart failure by echocardiography, radionuclide ventriculography and cardiovascular magnetic resonance. Are they interchangeable?* European heart journal, 2000. **21**(16): p. 1387-1396.

27. Amado, L.C., et al., *Accurate and objective infarct sizing by contrast-enhanced magnetic resonance imaging in a canine myocardial infarction model.* Journal of the American College of Cardiology, 2004. **44**(12): p. 2383-2389.

28. Amundsen, B.H., et al., *Noninvasive myocardial strain measurement by speckle tracking echocardiography: validation against sonomicrometry and tagged magnetic resonance imaging.* Journal of the American College of Cardiology, 2006. **47**(4): p. 789-793.

29. Axel, L. and L. Dougherty, *MR imaging of motion with spatial modulation of magnetization.* Radiology, 1989. **171**(3): p. 841-845.

30. Axel, L. and L. Dougherty, *Heart wall motion: improved method of spatial modulation of magnetization for MR imaging.* Radiology, 1989. **172**(2): p. 349-350.

31. Osman, N.F., et al., *Cardiac motion tracking using CINE harmonic phase (HARP) magnetic resonance imaging.* Magnetic Resonance in Medicine: An Official Journal of the International Society for Magnetic Resonance in Medicine, 1999. **42**(6): p. 1048-1060.

32. Osman, N.F., et al., *Imaging longitudinal cardiac strain on short - axis images using strain - encoded MRI.* Magnetic Resonance in Medicine: An Official Journal of the International Society for Magnetic Resonance in Medicine, 2001. **46**(2): p. 324-334.

33. Hor, K.N., et al., *Magnetic resonance derived myocardial strain assessment using feature tracking.* Journal of visualized experiments: JoVE, 2011(48).

34. Kim, D., et al., *Myocardial tissue tracking with two-dimensional cine displacement-encoded MR imaging: development and initial evaluation.* Radiology, 2004. **230**(3): p. 862-871.

35. Young, A.A., et al., *Generalized spatiotemporal myocardial strain analysis for DENSE and SPAMM imaging.* Magnetic resonance in medicine, 2012. **67**(6): p. 1590-1599.

36. Haggerty, C.M., et al., *Reproducibility of cine displacement encoding with stimulated echoes (DENSE) cardiovascular magnetic resonance for measuring left ventricular strains, torsion, and synchrony in mice.* Journal of cardiovascular magnetic resonance, 2013. **15**(1): p. 71.
37. Lin, K., et al., *Reproducibility of cine displacement encoding with stimulated echoes (DENSE) in human subjects.* Magnetic resonance imaging, 2017. **35**: p. 148-153.
38. Wehner, G.J., et al., *Comparison of left ventricular strains and torsion derived from feature tracking and DENSE CMR.* Journal of Cardiovascular Magnetic Resonance, 2018. **20**(1): p. 63.
39. Mangion, K., et al., *Circumferential strain predicts major adverse cardiovascular events following an acute ST-segment–elevation myocardial infarction.* Radiology, 2018: p. 181253.
40. Jing, L., et al., *Cardiac remodeling and dysfunction in childhood obesity: a cardiovascular magnetic resonance study.* Journal of Cardiovascular Magnetic Resonance, 2016. **18**(1): p. 28.
41. Zhong, X., et al., *Imaging three‐dimensional myocardial mechanics using navigator‐gated volumetric spiral cine DENSE MRI.* Magnetic resonance in medicine, 2010. **64**(4): p. 1089-1097.
42. Gilson, W.D., et al., *Complementary displacement‐encoded MRI for contrast‐enhanced infarct detection and quantification of myocardial function in mice.* Magnetic Resonance in Medicine: An Official Journal of the International Society for Magnetic Resonance in Medicine, 2004. **51**(4): p. 744-752.
43. Zhong, X., et al., *Selective suppression of artifact‐generating echoes in cine DENSE using through‐plane dephasing.* Magnetic resonance in medicine, 2006. **56**(5): p. 1126-1131.
44. Zhong, X., P.A. Helm, and F.H. Epstein, *Balanced multipoint displacement encoding for DENSE MRI.* Magnetic resonance in medicine, 2009. **61**(4): p. 981-988.
45. Spottiswoode, B.S., et al., *Tracking myocardial motion from cine DENSE images using spatiotemporal phase unwrapping and temporal fitting.* IEEE transactions on medical imaging, 2007. **26**(1): p. 15-30.
46. Spottiswoode, B.S., et al., *Motion-guided segmentation for cine DENSE MRI.* Medical image analysis, 2009. **13**(1): p. 105-115.
47. Zhong, X., et al., *Tracking brain motion during the cardiac cycle using spiral cine‐DENSE MRI.* Medical physics, 2009. **36**(8): p. 3413-3419.
48. Fischer, S.E., et al., *Limitations of stimulated echo acquisition mode (STEAM) techniques in cardiac applications.* Magnetic resonance in medicine, 1995. **34**(1): p. 80-91.

49. Stuber, M., et al., *Single breath-hold slice-following CSPAMM myocardial tagging.* Magnetic Resonance Materials in Physics, Biology and Medicine, 1999. **9**(1-2): p. 85-91.
50. Sigfridsson, A., et al., *In vivo SNR in DENSE MRI; temporal and regional effects of field strength, receiver coil sensitivity and flip angle strategies.* Magnetic resonance imaging, 2011. **29**(2): p. 202-208.
51. Wehner, G.J., et al., *Validation of in vivo 2D displacements from spiral cine DENSE at 3T.* Journal of Cardiovascular Magnetic Resonance, 2015. **17**(1): p. 5.
52. Fahmy, A.S., E.-S.H. Ibrahim, and N.F. Osman, *Spectrally-Presaturated Modulation (SPM): An efficient fat suppression technique for STEAM-based cardiac imaging sequences.* Magnetic resonance imaging, 2017. **37**: p. 209-215.
53. Mills, P., et al., *Localized imaging using stimulated echoes.* Magnetic resonance in medicine, 1987. **5**(4): p. 384-389.
54. Aletras, A.H., R.S. Balaban, and H. Wen, *High-resolution strain analysis of the human heart with fast-DENSE.* Journal of Magnetic Resonance, 1999. **140**(1): p. 41-57.
55. Pan, L., et al., *Real - time imaging of regional myocardial function using fast - SENC.* Magnetic Resonance in Medicine: An Official Journal of the International Society for Magnetic Resonance in Medicine, 2006. **55**(2): p. 386-395.
56. Weiger, M., K.P. Pruessmann, and P. Boesiger, *Cardiac real - time imaging using SENSE.* Magnetic Resonance in Medicine: An Official Journal of the International Society for Magnetic Resonance in Medicine, 2000. **43**(2): p. 177-184.
57. Uecker, M., et al., *Real - time MRI at a resolution of 20 ms.* NMR in Biomedicine, 2010. **23**(8): p. 986-994.
58. Wang, Y., et al., *Navigator-echo-based real-time respiratory gating and triggering for reduction of respiration effects in three-dimensional coronary MR angiography.* Radiology, 1996. **198**(1): p. 55-60.
59. Ehman, R.L. and J.P. Felmlee, *Adaptive technique for high-definition MR imaging of moving structures.* Radiology, 1989. **173**(1): p. 255-263.
60. Nehrke, K., et al., *Free-breathing cardiac MR imaging: study of implications of respiratory motion—initial results.* Radiology, 2001. **220**(3): p. 810-815.
61. Taylor, A.M., et al., *MR navigator - echo monitoring of temporal changes in diaphragm position: implications for MR coronary angiography.* Journal of Magnetic Resonance Imaging, 1997. **7**(4): p. 629-636.

62. Sussman, M.S., et al., *Variable - density adaptive imaging for high - resolution coronary artery MRI.* Magnetic Resonance in Medicine: An Official Journal of the International Society for Magnetic Resonance in Medicine, 2002. **48**(5): p. 753-764.
63. Hardy, C.J., et al., *Coronary MR angiography: respiratory motion correction with BACSPIN.* Journal of Magnetic Resonance Imaging, 2003. **17**(2): p. 170-176.
64. Larson, A.C., et al., *Preliminary investigation of respiratory self - gating for free - breathing segmented cine MRI.* Magnetic Resonance in Medicine: An Official Journal of the International Society for Magnetic Resonance in Medicine, 2005. **53**(1): p. 159-168.
65. Leung, A.O., I. Paterson, and R.B. Thompson, *Free - breathing cine MRI.* Magnetic resonance in medicine, 2008. **60**(3): p. 709-717.
66. Liu, J., et al., *Respiratory and cardiac self - gated free - breathing cardiac CINE imaging with multiecho 3D hybrid radial SSFP acquisition.* Magnetic resonance in medicine, 2010. **63**(5): p. 1230-1237.
67. Feng, L., et al., *XD - GRASP: golden - angle radial MRI with reconstruction of extra motion - state dimensions using compressed sensing.* Magnetic resonance in medicine, 2016. **75**(2): p. 775-788.
68. Hu, P., et al., *Motion correction using coil arrays (MOCCA) for free - breathing cardiac cine MRI.* Magnetic resonance in medicine, 2011. **66**(2): p. 467-475.
69. Sachs, T.S., et al., *Real - time motion detection in spiral MRI using navigators.* Magnetic resonance in medicine, 1994. **32**(5): p. 639-645.
70. Shechter, G. and E.R. McVeigh. *MR motion correction of 3D affine deformations*. in *Proceedings Int Soc Mag Reson Med*. 2003. Citeseer.
71. Moghari, M.H., et al., *Three - dimensional heart locator for whole - heart coronary magnetic resonance angiography.* Magnetic resonance in medicine, 2014. **71**(6): p. 2118-2126.
72. Pipe, J.G., *Motion correction with PROPELLER MRI: application to head motion and free-breathing cardiac imaging.* Magnetic resonance in medicine, 1999. **42**(5): p. 963-969.
73. Leung, G. and D.B. Plewes, *Retrospective motion compensation using variable - density spiral trajectories.* Journal of Magnetic Resonance Imaging: An Official Journal of the International Society for Magnetic Resonance in Medicine, 2005. **22**(3): p. 373-380.

74. Bhat, H., et al., *3D radial sampling and 3D affine transform - based respiratory motion correction technique for free - breathing whole - heart coronary MRA with 100% imaging efficiency.* Magnetic resonance in medicine, 2011. **65**(5): p. 1269-1277.

75. Pang, J., et al., *Whole - heart coronary MRA with 100% respiratory gating efficiency: self - navigated three - dimensional retrospective image - based motion correction (TRIM).* Magnetic resonance in medicine, 2014. **71**(1): p. 67-74.

76. Usman, M., et al., *Motion corrected compressed sensing for free - breathing dynamic cardiac MRI.* Magnetic resonance in medicine, 2013. **70**(2): p. 504-516.

77. Lai, P., et al., *A dual - projection respiratory self - gating technique for whole - heart coronary MRA.* Journal of Magnetic Resonance Imaging, 2008. **28**(3): p. 612-620.

78. Sinkus, R. and P. Börnert, *Motion pattern adapted real - time respiratory gating.* Magnetic Resonance in Medicine: An Official Journal of the International Society for Magnetic Resonance in Medicine, 1999. **41**(1): p. 148-155.

79. Sachs, T.S., et al., *The diminishing variance algorithm for real - time reduction of motion artifacts in MRI.* Magnetic resonance in medicine, 1995. **34**(3): p. 412-422.

80. Sachs, T.S., et al., *The real-time interactive 3-D-DVA for robust coronary MRA.* IEEE transactions on medical imaging, 2000. **19**(2): p. 73-79.

81. Kihlberg, J., et al., *Clinical experience of strain imaging using DENSE for detecting infarcted cardiac segments.* Journal of Cardiovascular Magnetic Resonance, 2015. **17**(1): p. 50.

82. Hamlet, S.M., et al., *Optimal configuration of respiratory navigator gating for the quantification of left ventricular strain using spiral cine displacement encoding with stimulated echoes (DENSE) MRI.* Journal of Magnetic Resonance Imaging, 2017. **45**(3): p. 786-794.

83. Anderson, A.W. and J.C. Gore, *Analysis and correction of motion artifacts in diffusion weighted imaging.* Magnetic resonance in medicine, 1994. **32**(3): p. 379-387.

Chapter 2
Free-breathing cine DENSE MRI using phase-cycling with match-making and stimulated-echo image-based navigators

2.1 Introduction

Cine displacement encoding with stimulated echoes (DENSE) [1] is a myocardial strain imaging method that is accurate [2], reproducible for both global and regional measurements [3], and amenable to rapid displacement and strain analysis [4]. Like many cardiac MRI acquisitions, cine DENSE is generally performed during breath-holding. However, multiple breath-holds can be taxing for many patients and complicated for the technologists. Self-navigated free-breathing methods could overcome these problems. Self-navigated methods have the advantages that they do not require additional diaphragm-based navigator (dNAV) setup procedures and they are more efficient than dNAVs because, with motion estimation and correction, they use data acquired during much or all of the respiratory cycle. However, self-navigated techniques have not yet been developed for strain imaging methods such as cine DENSE.

In free-breathing cine DENSE, respiration induced motion that occurs from heartbeat to heartbeat (inter-heartbeat motion) leads to two major types of artifacts, striping and blurring artifacts. The striping artifacts are due to insufficient suppression of the T1-relaxation echo with phase-cycling subtraction, which represents a unique and major challenge for free-breathing self-navigated cine DENSE. In addition, inter-heartbeat motion also induces blurring of the stimulated-echo image, as it does for other MR images. These two types of artifacts can lead to unsuccessful imaging of patients with imperfect breath-holding, as previously reported [5, 6]. The purpose the study in this chapter was to develop an effective method for free-breathing self-navigated cine DENSE,

and the proposed approach involved suppression of the T_1-relaxation echo as a first step, followed by the use of image-based navigators (iNAVs) for motion estimation and correction as a second step.

2.2 Methods

2.2.1. Free-breathing cine DENSE framework

A self-navigated framework is proposed for free-breathing spiral cine DENSE to (a) select phase-cycled spiral interleaves at matched respiratory phases, (b) perform subtraction of matched phase-cycled interleaves, (c) reconstructs image-based navigators (iNAVs) from post-subtraction interleaves (ps-interleaves) that are primarily comprised of the stimulated echo (termed ste-iNAVs), (d) performs ste-iNAV-based motion estimation to account for motion between ps-interleaves, and (e) applies rigid motion correction in k-space for image reconstruction. The first part of this method, which selects phase-cycled interleaves at matched respiratory phases, is termed "match-making". The proposed framework is illustrated in Figure 2.1A and is shown in contrast to conventional respiratory-gated navigator strategies such as dNAVs or conventional iNAVs (c-iNAVs) (Figure 2.1B).

The metric for match-making of phase-cycled interleaves acquired during free breathing is the residual energy of the T_1-relaxation echo after complex subtraction of those phase-cycled interleaves. This approach is based on the concept that the residual T_1-relaxation echo energy will be minimized when the phase-cycled interleaves are acquired at matched respiratory phases, and will be greater otherwise. Since the approximate location in k-space of the T_1-relaxation echo is determined by the displacement-encoding frequency, k_e, the residual T_1-relaxation echo energy can be estimated by summing data over a predetermined region of k-space, i.e., $k > k_e/2$. Along with match-making to suppress the T_1-relaxation echo, localized generation of stimulated echoes is also employed, so that ste-iNAVs can be focused to the heart, a reduced field of view (FOV) can be used, and automated motion estimation is facilitated.

2.2.2. Pulse sequence

To experimentally investigate free-breathing cine DENSE imaging using the match-making framework with motion compensation, a previously-described spiral cine DENSE pulse sequence [7], which supports two-point phase-cycling, was modified to include golden angle rotation [8, 9] through time frames within the cardiac cycle and localized generation of stimulated echoes, as shown in Figure 2.2. Golden angle rotation facilitates the reconstruction of iNAVs by utilizing consecutively acquired interleaves. In the current design, each fully sampled iNAV frame consisted of eight consecutively acquired interleaves, i.e. four consecutive frames with golden angle rotation between them and two interleaves per frame with uniform rotation. Localized generation of stimulated echoes was implemented by applying slice selection for all RF pulses that contribute to the stimulated echo such that stimulated echoes were generated only in the region where the RF pulse profiles intersect [10, 11]. With this pulse sequence, the stimulated echo can be localized to the heart region but the T_1-relaxation echo originates from the entire slice. The cine DENSE pulse sequence also supported the acquisition of a dNAV at end-diastole, as previously described [7]. All DENSE scans employed multicoil acquisitions, and multi-channel data were adaptively combined to reconstruct complex images with sensitivity maps estimated from the data itself, as previously described [12].

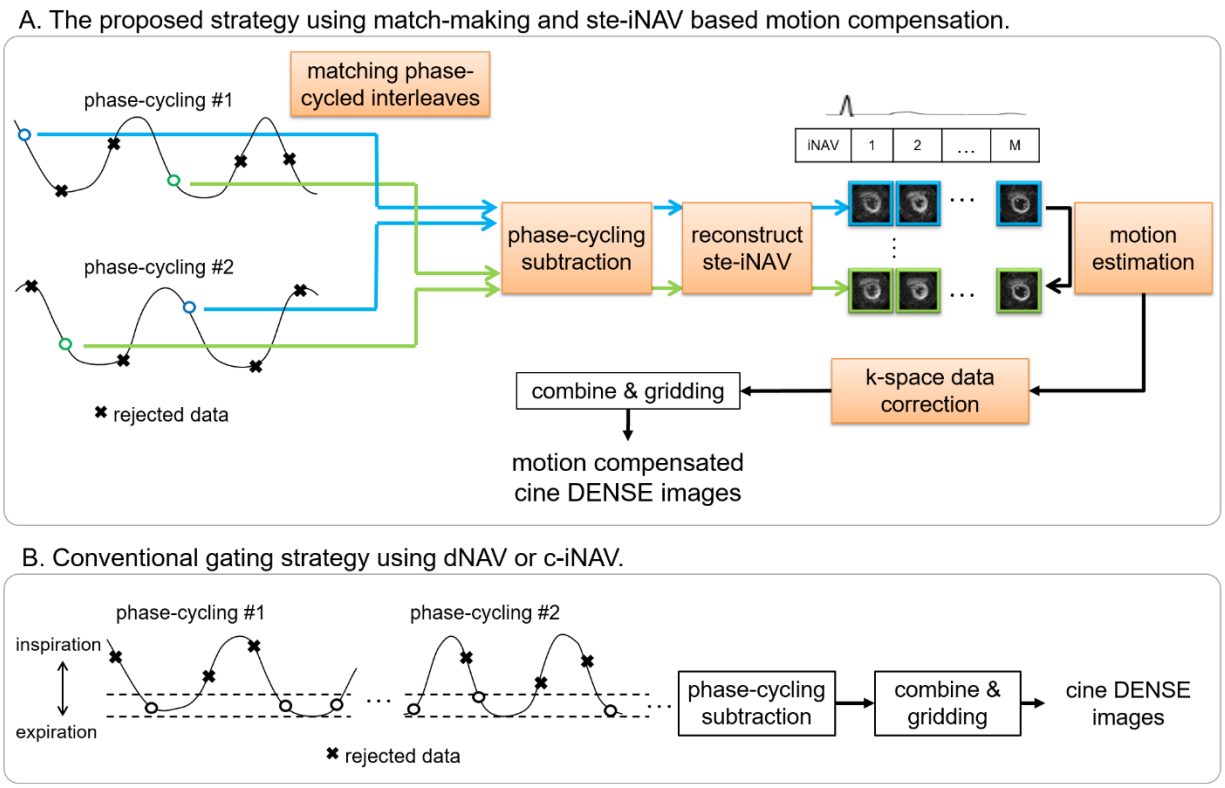

Figure 2.1. Diagram of the proposed match-making framework. (A) Diagram of the proposed match-making framework for free-breathing cine DENSE imaging. First, match-making is applied to identify phase-cycled interleave pairs acquired at matched respiratory positions to compensate for striping artifacts. The two blue circles identify a matched phase-cycling pair and the two green circles identify another matched pair. Phase-cycling subtraction is performed using the identified phase-cycled interleaves and ste-iNAVs are reconstructed from post-subtraction data. Lastly, ste-iNAV based in-plane motion estimation and correction is performed to compensate for blurring artifacts. (B) Diagram of the conventional respiratory gating strategy using dNAVs or conventional iNAVs (c-iNAVs), where data within a narrow window around end-expiration are accepted.

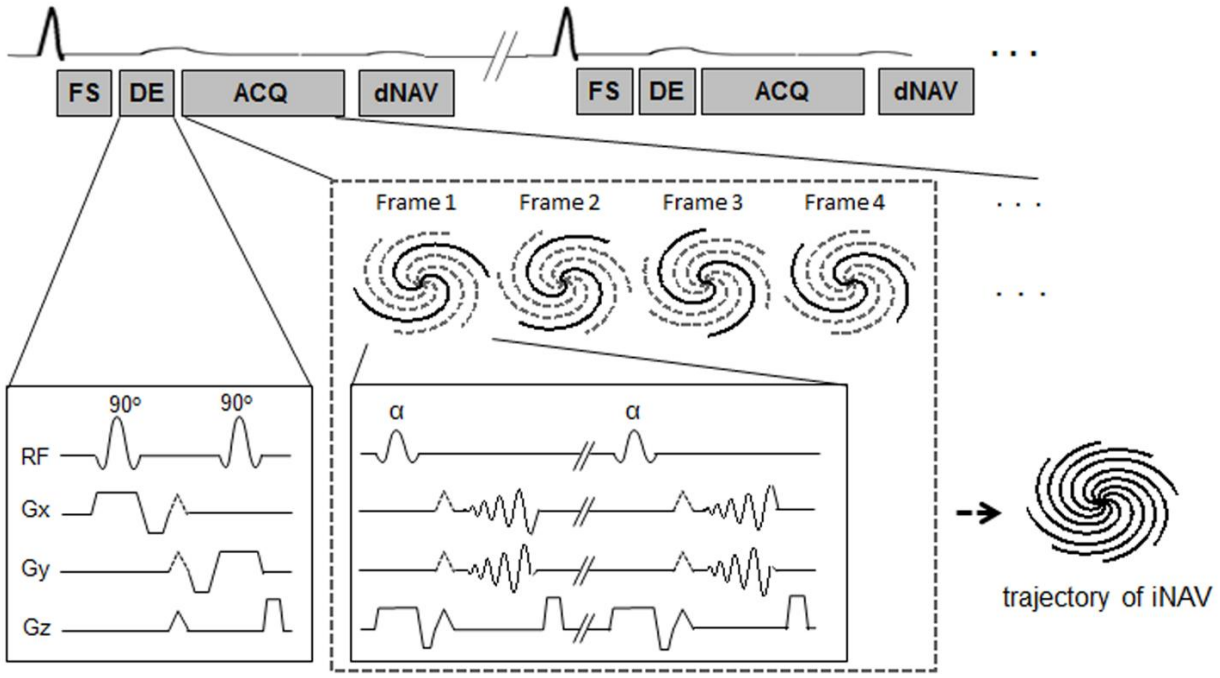

Figure 2.2. Diagram of the pulse sequence used for free-breathing cine DENSE. Fat saturation (FS) is applied after each ECG trigger, followed by displacement encoding (DE) pulses, spiral acquisitions (ACQ) and the diaphragm navigator (dNAV). Localized generation of stimulated echoes is performed by applying slice selection for all RF pulses, including those in the displacement encoding module. Data acquisition uses a segmented spiral trajectory with golden angle rotation of the trajectory through cardiac frames. Each iNAV frame consists of four cine DENSE frames (i.e., eight consecutive spiral interleaves).

2.2.3. Reconstruction using the match-making framework

As illustrated in Figure 2.1A, phase-cycled spiral interleaves at matched respiratory phases were selected using the match-maker criterion, specifically the minimal residual T_1-relaxation echo energy. Matched interleaves must have the same displacement encoding and k-space trajectory, and they could be selected from any respiratory phase, without limitation. The residual T_1 -relaxation echo energy was averaged over all cardiac frames within each heartbeat. Assuming multiple repetitions of all interleaves are acquired and of the available pairs of interleaves to choose from, the one pair (one repetition) with the lowest residual T_1-echo energy (the match) is selected for the reconstruction, and all other data are discarded. After match-making, subtraction

of matched interleaves was performed and ste-iNAVs were reconstructed. Multiple ste-iNAVs were reconstructed per heartbeat, specifically one ste-iNAV was reconstructed using eight spiral interleaves, and a sliding window was not used. Two-dimensional translations were estimated using the ste-iNAVs automatically, without manual identification of a region, using two-dimensional cross-correlation. Motion estimation was performed separately for different cardiac phases. The resulting motion estimation was used for motion compensation of the selected segmented k-space data [13]. The resulting motion-corrected k-space data underwent density-weighted nonuniform fast Fourier transform [14] to reconstruct final cine DENSE images.

2.2.4. Reconstruction using conventional dNAV gating

As illustrated in Figure 2.1B, the conventional dNAV reconstruction method accepted data acquired within a dNAV window centered at end-expiration and rejected data outside that window. Specifically, in the protocol for in vivo experiments, a fixed number of repetitions were acquired, and in a retrospective reconstruction, one repetition of data that were within the narrowest window at end-expiration based on the dNAV position were accepted. This method was chosen to ensure a fair comparison between the various reconstructions.

2.2.5. Reconstruction using conventional iNAV gating

For the c-iNAV reconstruction, c-iNAVs were reconstructed using the methods described in the Appendix. Since c-iNAVs were reconstructed for each individual heartbeat, their reconstruction did not employ subtraction of phase-cycled interleaves. Instead, suppression of the T_1-relaxation echo for the c-iNAVs was performed by separating the stimulated echo and T_1-relaxation echoes using principal component analysis (PCA), and applying a PCA filter to the iNAVs (Appendix). An early systolic c-iNAV was used and 2D translation was estimated by 2D cross-correlation for displacement-based retrospective gating. Similar to dNAV-gating, one repetition of data within a narrow window around end expiration defined by the c-iNAV position were accepted, as described in Figure 2.1B.

2.2.6. Phantom experiments

Phantom experiments were conducted to demonstrate the use of matching phase-cycled interleaves using the residual T_1-echo energy and using localized ste-iNAVs for motion estimation and correction. All phantom imaging was performed on a 3T MRI system (Magnetom Prisma, Siemens Healthcare, Erlangen, Germany) with a 32-channel phased-array spine coil. Specifically, a phantom was scanned and cine DENSE datasets were acquired six times. In between each acquisition, the phantom was moved toward the head direction in 5 mm increments to create a range of translations. For each phantom position, a coronal slice, a transverse slice and an oblique slice between the coronal and transverse planes were scanned. The motions seen by these three slices were in-plane translation, through-plane motion and a combination of in-plane and through-plane motion, respectively. Cine DENSE datasets were acquired with the following parameters: FOV = 260 x 260 mm^2, 10 spiral interleaves, spiral readout length of 2.8 ms, in-plane spatial resolution of 3.4 x 3.4 mm^2, 2 spiral interleaves per segment, TR = 15 ms, TE = 1.08 ms, and slice thickness = 8 mm. The displacement encoding frequency was 0.10 cycles/mm, and the through-plane dephasing frequency was 0.04 cycles/mm. The T_1 of the phantom was approximately 150 ms. DENSE imaging was performed with a simulated RR interval of 1000 ms. Ten frames were imaged for the phantom experiment. The trigger time of the images used for data analysis was 150 ms. For analysis, the correlation coefficient between the residual T_1-echo energy and the amount of phantom motion was calculated and motion estimation and compensation were performed using ste-iNAVs.

2.2.7. In-vivo experiments

In addition, free-breathing cine DENSE datasets were acquired from 12 healthy volunteers (7 male, 27.3 ± 2.1 years old) who were scanned in accordance with protocols approved by the institutional review board after providing informed consent. All volunteer imaging was performed on 3T systems (Magnetom Trio and Magnetom Prisma; Siemens Healthineers, Erlangen, Germany) with a phased-array body coil (6-channel for Magnetom Trio and 18-channel for Magnetom Prisma) and a 32-channel spine coil. After the acquisition of localizer images, a mid-ventricular short-axis slice was acquired during

both breath-holding and free-breathing acquisitions with the following parameters: FOV = 160 x 160 mm^2, thickness of localized stimulated echo = 80 - 100 mm^2, 6 spiral interleaves per image, 2 interleaves per segment, spiral readout length of 3.4 ms, in-plane spatial resolution of 3 x 3 mm^2, slice thickness = 8 mm, TR = 15 ms, TE = 1.08 ms, and temporal resolution of 30 ms. Ramped flip angles with a final flip angle of 15 degrees were employed to achieve a consistent signal-to-noise ratio (SNR) through the cardiac cycle [15]. Fat suppression was employed by applying a fat saturation pulse immediately after ECG triggering as previously described [7, 16]. Depending on the heart rate of the subject, 22-30 frames were acquired, covering approximately 80% of the RR interval. The rest of the RR interval was used to acquire the dNAV and allow for variation in the RR interval. The total scan time was 18 heartbeats (corresponding to one repetition) for breath-hold acquisitions and 54 heartbeats (corresponding to the acquisition of each interleave three times, and implemented using the repetition loop) for free-breathing acquisitions. As shown in Figure 2.3, the DENSE loop structure, from inner to outer, looped through interleaves per segment, k-space segments, repetitions, phase-cycling pairs, and displacement-encoding dimensions, which included reference, x-encoded and y-encoded acquisitions [17]. The temporal and spatial resolutions were chosen based on protocols that have been reported in clinical studies to provide a balance of SNR, temporal resolution, and total scan time [18]. Additionally, for 5 subjects, a 15-repetition dataset (270 heartbeats in duration) was acquired and these data were used to demonstrate the relationships between ste-iNAV and c-iNAV motion estimation and dNAV data. All 3-repetition datasets were reconstructed offline three ways in MATLAB (Mathworks, Natick, MA) using: (a) the conventional dNAV method, (b) the c-iNAV method and (c) the match-making framework.

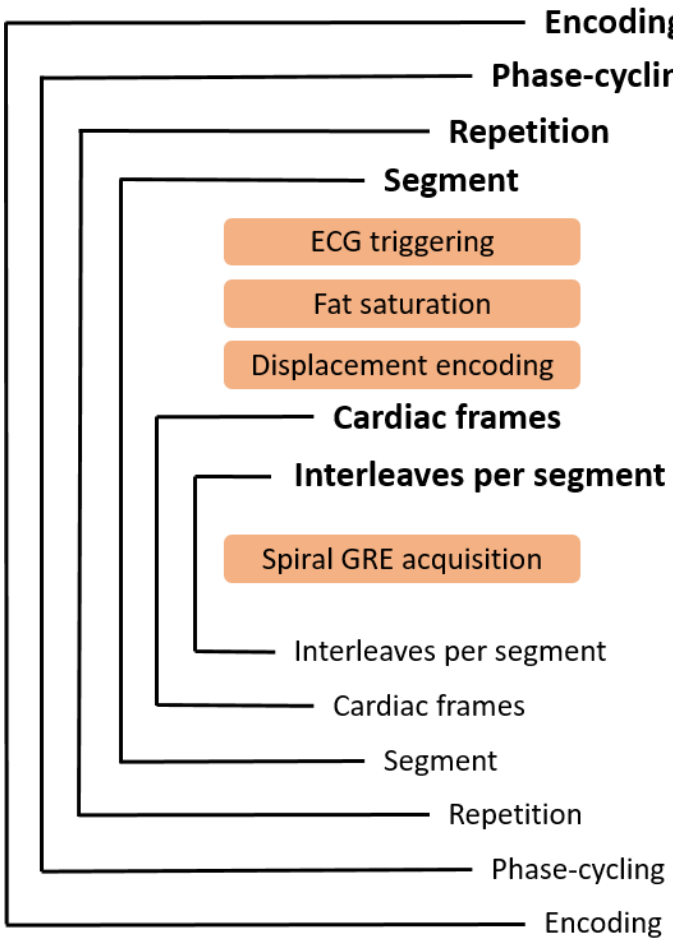

Figure 2.3. Loop structure of cine DENSE acquisition.

2.2.8. Evaluation of the match-making framework

The volunteer data were used to evaluate intermediate steps of the match-making framework as applied to in vivo imaging. Specifically, the correlation between the residual T_1-echo energy and the difference in the dNAV positions for all phase-cycling interleave pairs from free-breathing acquisitions was calculated. These data could demonstrate that low residual T_1-echo energy of ps-interleaves indicates that the phase-cycled interleave pair were acquired at matched respiratory phases, and vice versa. The ste-iNAVs were also compared with c-iNAVs by assessing the correlation of motion estimated from iNAVs with respiration measured by dNAVs using the 15-repetition acquisitions. Specifically, for each of the first 15 heartbeats, the best phase-cycling match was found from subsequent heartbeats. Then ste-iNAVs were reconstructed and used to

estimate respiration-induced heart motion (2D translations) between the ste-iNAVs. The translations were then correlated to the dNAV positions of the first 15 heartbeats. Correlations were analyzed for both x- and y-translations, and for all encoding dimensions. For comparison, translations were also estimated using c-iNAVs for the first 15 heartbeats of the same datasets and correlated to the dNAV positions. The Signed Rank test was used to test for statistically significant differences in correlations with significance level set at 0.05. In addition, the motion estimation algorithm was applied to ste-iNAVs reconstructed from the breath-holding datasets to demonstrate that negligible motion estimates are obtained in these conditions. The range of motion from breath-holding ste-iNAVs was compared to that estimated from free-breathing datasets.

2.2.9. Comparison with the conventional dNAV and c-iNAV methods

Finally, free-breathing cine DENSE magnitude and phase images reconstructed using dNAV, c-iNAV, and match-making framework were compared. Each of the volunteer datasets was reconstructed using all three methods. Because factors that affect intrinsic SNR such as number of repetitions, voxel size, and readout time were constant for all reconstruction methods, but breathing artifacts can lead to an apparent SNR reduction by affecting both the myocardial and background signals, the different reconstruction methods were compared using apparent SNR. The apparent SNR was measured from magnitude-reconstructed images using a region of interest (ROI) that included all of the myocardium within a slice and a large background ROI. The apparent SNR was calculated as the mean of the myocardial ROI divided by the standard deviation of the background ROI, and the correction for the Rician distribution of the magnitude signal was applied [19, 20]. In addition, phase quality (the variance of the local 2D spatial derivative of the phase image) [21, 22] was measured from all of the manually-segmented myocardium within each slice. Phase quality was calculated for background phase-corrected phase images after phase unwrapping. Also, for each reconstruction method, the residual T_1-echo energy was computed from the corresponding raw data. Given that k-space energy varies among subjects and scans, for each dataset the residual T_1-echo energy was normalized to a baseline value estimated from early systole (the minimal residual T_1-echo energy within 300 ms after the displacement-encoding pulses) of the best-matched phase-cycling interleaves and the normalized value is referred as relative

residual T_1-echo energy. In this way, the residual T_1-echo energy can be compared both among reconstruction methods and among subjects. Apparent SNR, phase quality and the relative residual T_1-echo energy were averaged over all cardiac phases.

The total acceptance windows and the inter-phase-cycling motion for accepted data were also compared for each reconstruction method. The total acceptance windows were computed using the corresponding dNAV data defined as the range of dNAV positions for accepted heartbeats. The inter-phase-cycling motion was quantified as the difference in dNAV positions between the two interleaves of each accepted phase-cycling pair. All quantifications are presented as mean ± standard error. One-way repeated-measures ANOVA (or one-way repeated-measures ANOVA with ranks if the normality test failed) was used to test for statistical significance with significance level set at 0.05. Lastly, circumferential strain was computed [22] using a single-slice six-segment model for each reconstruction method. Bland-Altman plots were used to analyze the agreement of strain values from free-breathing acquisitions with those from breath-holding acquisitions.

2.3 Results

2.3.1. Demonstration of the match-making framework with phantom

Cine DENSE data were acquired from a phantom positioned at different locations to demonstrate the reduction of striping and blurring artifacts using matching of phase-cycled interleaves and ste-iNAV motion correction. Example k-space domain signals after subtraction of phase-cycled interleaves sampled along a spiral trajectory are illustrated in Figure 2.4A. In one case (black line) the phase-cycled interleaves were acquired at matched locations and in the other case (red line) the phase-cycled interleaves were acquired at mismatched locations. For matched locations, the echo due to T_1 relaxation is well suppressed, whereas for mismatched locations it is not (arrows). Multiple peaks corresponding to the T_1-relaxation echo are observed because the spiral trajectory intersects the T_1-relaxation echo multiple times, as shown in Figure 2.4B. Experiments were performed where the phantom was moved between 0 – 25 mm with 5 mm increments, and Figure 2.4C-E demonstrate that the residual T_1-echo energy after

subtraction of phase-cycled interleaves is linearly related to the distance the phantom was moved between the acquisitions of the phase-cycled interleaves. This finding holds for in-plane motion (Figure 2.4C), through-plane motion (Figure 2.4D), and a combination of in-plane and through-plane motion (Figure 2.4E). These results show that the residual T_1-echo energy is an indicator of the amount of motion between acquisitions of phase-cycled interleaves, and that very low residual T_1-echo energy can be used to select phase-cycled interleaves acquired at matched locations (match-making). Figure 2.4G-H shows that striping artifacts are removed from the DENSE image when phase-cycled interleaves from matched locations are selected and subtracted, but image blurring still occurs when ps-interleaves from different locations are combined for the reconstruction. By using the ste-iNAV of each ps-interleave for motion estimation, k-space domain motion correction can be applied to compensate for the blurring induced by in-plane motion (Figure 2.4I), and the images corrected for in-plane motion compare favorably to corresponding images from data acquired at a single position (Figure 2.4F). Together, these results demonstrate the use of match-making and ste-iNAV-based motion estimation to compensate for motion-induced artifacts.

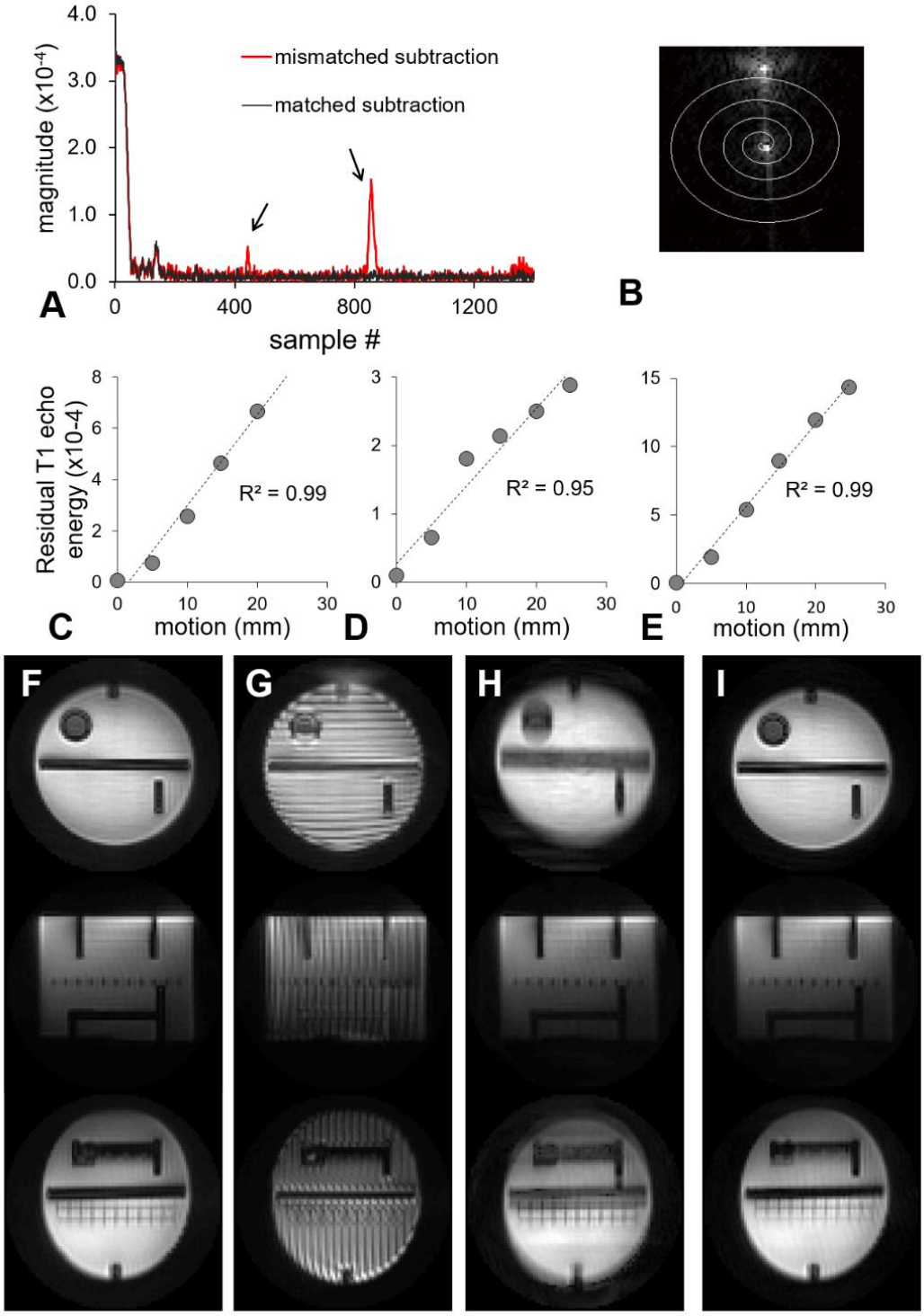

Figure 2.4. Results of the phantom experiment demonstrating the match-maker method. (A) Intensities of k-space data along a post-subtraction spiral interleave (ps-interleave) from subtraction of matched phase-cycled interleaves (black curve) and mismatched phase-cycled

interleaves (red curve). Strong residual T_1-relaxation echo signal remains in the ps-interleave from the mismatched subtraction (arrows). (B) Illustrative trajectory of the ps-interleave in (A). (C-E) Correlation between the residual T_1-relaxation echo energy of the ps-interleave and the amount of translation between interleaves for in-plane motion (C), through-plane motion (D), and a combination of both in-plane and through-plane motion (E), respectively. (F-I) Demonstration of applying the match-maker framework for the cases of in-plane (top), through-plane (middle) and combined (bottom) motions. (F) Motion-free reference images. (G) Images reconstructed using ps-interleaves of mismatched phase-cycled interleave pairs have strong striping artifacts and blurring. (H) The images from ps-interleaves with matched phase-cycling but with motion between ps-interleaves show removal of striping artifacts but still have blurring. (I) Using the match-making framework with motion compensation, blurring artifacts due to in-plane motion were also removed.

2.3.2. Evaluation of the match-making framework in vivo

For in-vivo evaluation, two datasets were excluded from analysis due to extremely low SNR and extensive artifacts in images reconstructed by dNAV, c-iNAV, and match-making methods. Figure 2.5 demonstrates the use of the residual T_1-echo energy as an effective criterion for matching phase-cycled interleaves for in vivo imaging. The respiratory pattern of a volunteer as measured by the dNAV signal is shown in Figure 2.5A, and the respiratory phases of three interleaves are annotated. Specifically, interleave A (Int-A) and interleave B (Int-B) are a pair of phase-cycled interleaves acquired at different respiratory phases, while Int-B and Int-C are phase-cycled interleaves acquired at a similar respiratory phase. Figure 2.5B shows the k-space domain data after subtraction of the two pairs of phase-cycled interleaves and demonstrates suppression of the residual T_1-echo for interleaves acquired at matched respiratory phases and substantial residual T_1-echo signal for interleaves acquired at mismatched respiratory phases. Figure 2.5C shows that the residual T_1-echo energy remains low throughout the cardiac cycle for the phase-cycled interleaves acquired at similar respiratory phases, but increases for the phase-cycled interleaves acquired at different respiratory phases. For all phase-cycled interleave pairs from this acquisition, the relative residual T_1-echo energy (averaged over all cardiac frames) was highly correlated with the difference in the corresponding dNAV positions, $\Delta\mathrm{dNAV}$, with R^2 of 0.71. The average R^2 for all subjects was 0.61 ± 0.04 (N = 10). These results demonstrated that the relative

residual T_1-echo energy was an indicator of respiratory motion between phase-cycled interleaves.

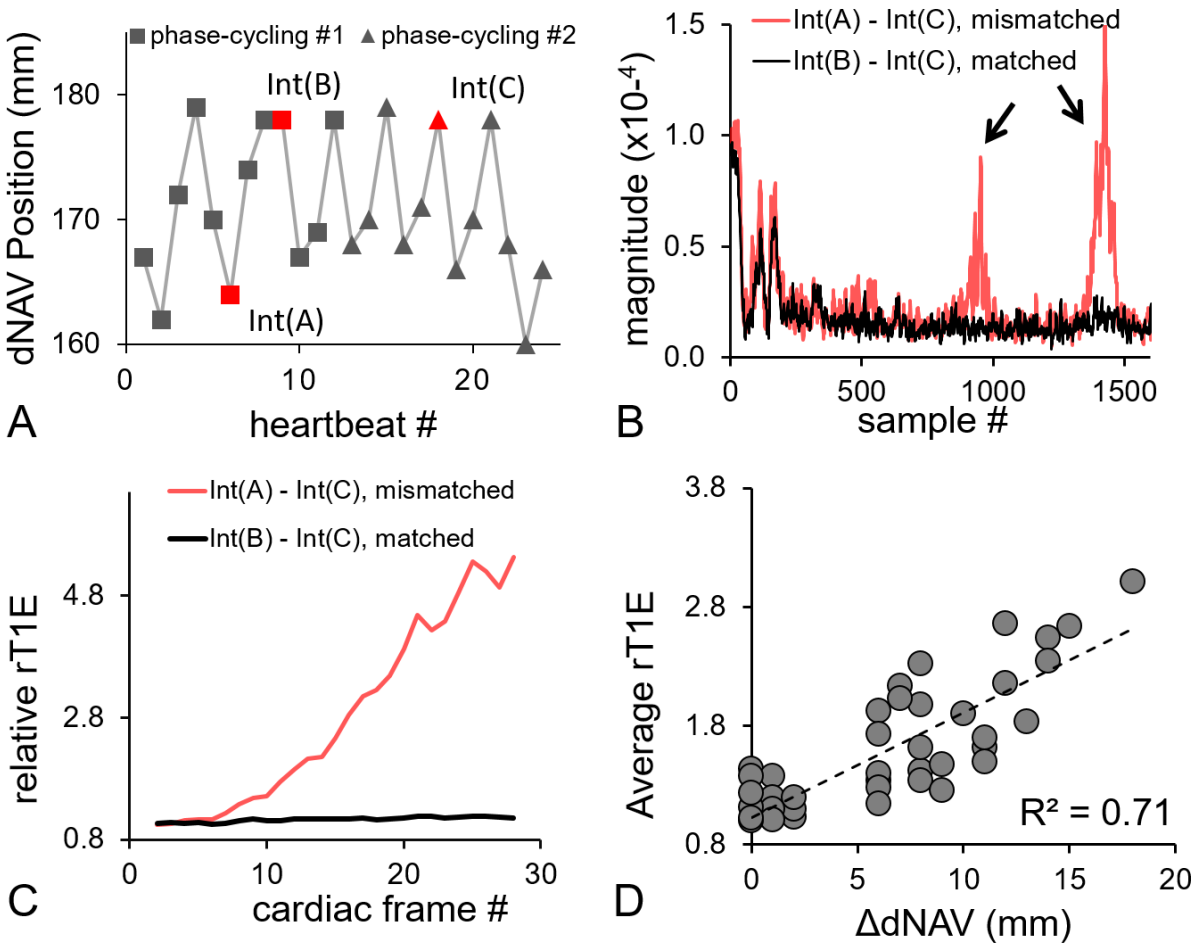

Figure 2.5. Phase-cycled cine DENSE data acquired during free breathing were processed to show that the relative residual T_1-relaxation echo energy from phase-cycled interleave pairs correlates with the difference in the diaphragm positions of the interleave pairs for in vivo imaging. (A) dNAV-based monitoring of respiration is shown, along with the annotated acquisitions of phase-cycled interleaves. (B) Magnitudes of post-subtraction interleaves for interleave pairs at similar (Int(B) – Int(C)) and different (Int(A) – Int(C)) respiratory positions. (C) The relative residual T_1-relaxation echo energies of the two phase-cycling pairs at each cardiac frame. (D) The relative residual T_1-relaxation-echo energy summed over all cardiac frames is highly correlated to the difference in the diaphragm positions, with $R^2 = 0.71$.

2.3.3. Match-maker ste-iNAVs assess respiration-induced heart motion better than c-iNAVs

Figure 2.6 shows (A) a c-iNAV reconstructed using a simple low-pass filter to suppress the T_1-relaxation echo, (B) a c-iNAV reconstructed using a simple low-pass filter and PCA filtering, and (C) a match-maker ste-iNAV. The ste-iNAV is localized to the heart and depicts the heart more clearly than the c-iNAVs. Note that Figure 2.6 shows navigator images, not reconstructed DENSE images. Figure 2.6 also shows the correlation between respiration-induced heart motion as estimated by iNAVs and diaphragm motion as measured by dNAVs for both c-iNAVs (with low-pass and PCA filtering) and ste-iNAVs. As shown in Figure 2.6G, the correlation for ste-iNAVs was significantly higher than that of c-iNAVs for the same datasets, with an R^2 of 0.82 ± 0.03 vs. 0.70 ± 0.05 ($P < 0.05$, signed-rank test). This result supports the premise that motion estimation was more accurate using ste-iNAVs compared to using c-iNAVs. Also, the overall range of heart motion due to respiration estimated from breath-holding ste-iNAVs was negligible (0.62 ± 0.20 mm, $N = 5$) compared to the range of heart motion estimated from the free-breathing ste-iNAVs (6.75 ± 3.33 mm, $N = 5$).

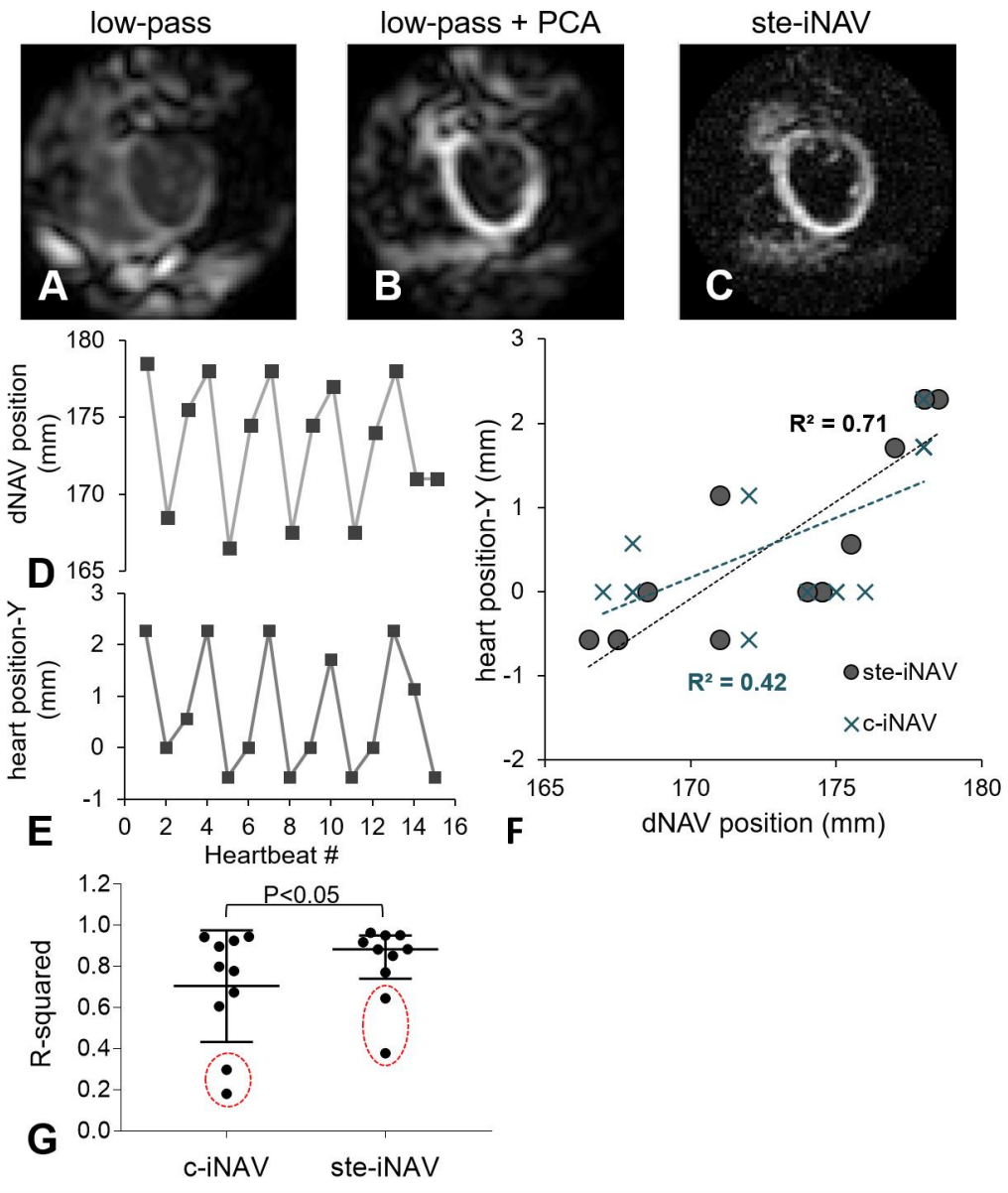

Figure 2.6. Comparison of conventional iNAVs and ste-iNAVs. Example iNAVs are shown for (A) an iNAV reconstructed from pre-subtraction data with low-pass filtering, (B) an iNAV reconstructed with PCA-based and low-pass filtering, and (C) a ste-iNAV from matched ps-interleave data, which is localized to the heart region and provides higher spatial resolution. Panel (D) shows the dNAV positions for 15 consecutive heartbeats, and panel (E) shows heart motion estimated from ste-iNAVs for the same 15 heartbeats. Panel (F) provides an example showing that the correlation of iNAV-measured heart motion to dNAV position measured by ste-iNAVs is higher than for conventional iNAVs (c-iNAVs). Panel (G) shows the R^2 values for all five subjects and for both x- and y-translations and all encoding dimensions (median

and interquartile range values are displayed). The two data points (circled) showing the worst correlation for c-iNAV and ste-iNAV corresponded to the same subjects.

was significantly lower than that of the dNAV and c-iNAV methods, demonstrating that the match-making framework better suppressed the T_1 relaxation echoes. The apparent SNR of the match-making framework was higher than that for both the dNAV and c-iNAV methods, and the phase quality was lower or trended to be lower than that of the dNAV and c-iNAV methods, demonstrating better image quality.

2.3.4. Comparison of cine DENSE reconstructions

Example cine DENSE magnitude and phase images for the dNAV, c-iNAV, and matchmaker reconstruction methods applied to the same raw data are shown in Figure 2.7 for both systolic and diastolic cardiac frames. Magnitude reconstructed images using the dNAV and c-iNAV methods had striping artifacts due to residual T_1-relaxation echoes (yellow arrows). However, for the match-making framework, the magnitude reconstructed image had less artifact, higher apparent SNR, and less blurring. The phase images of the match-maker framework had a smoother appearance within the myocardium. The relative residual T_1-echo energy, apparent SNR, and phase quality are summarized for all volunteer data in Figure 2.8A-C. The relative residual T_1-echo energy of the match-making framework Figure 2.8D-E compares the total acceptance windows (as measured by the dNAV positions) and the motion within each accepted phase-cycled interleave pair (as measured by the dNAV positions) for the dNAV and c-iNAV methods and for the match-making framework. The match-making framework had a larger total acceptance window than the conventional dNAV method, indicating that it accepted data from a wider range of respiratory phases. The motion within selected phase-cycled interleave pairs was smaller for the match-making framework compared to the c-iNAV method.

Figure 2.9 shows the Bland-Altman plots of circumferential strain comparing agreement between free-breathing and breath-holding acquisitions for all subjects and all segments. The match-making framework provided better agreement with breath-holding acquisitions than the dNAV and c-iNAV methods.

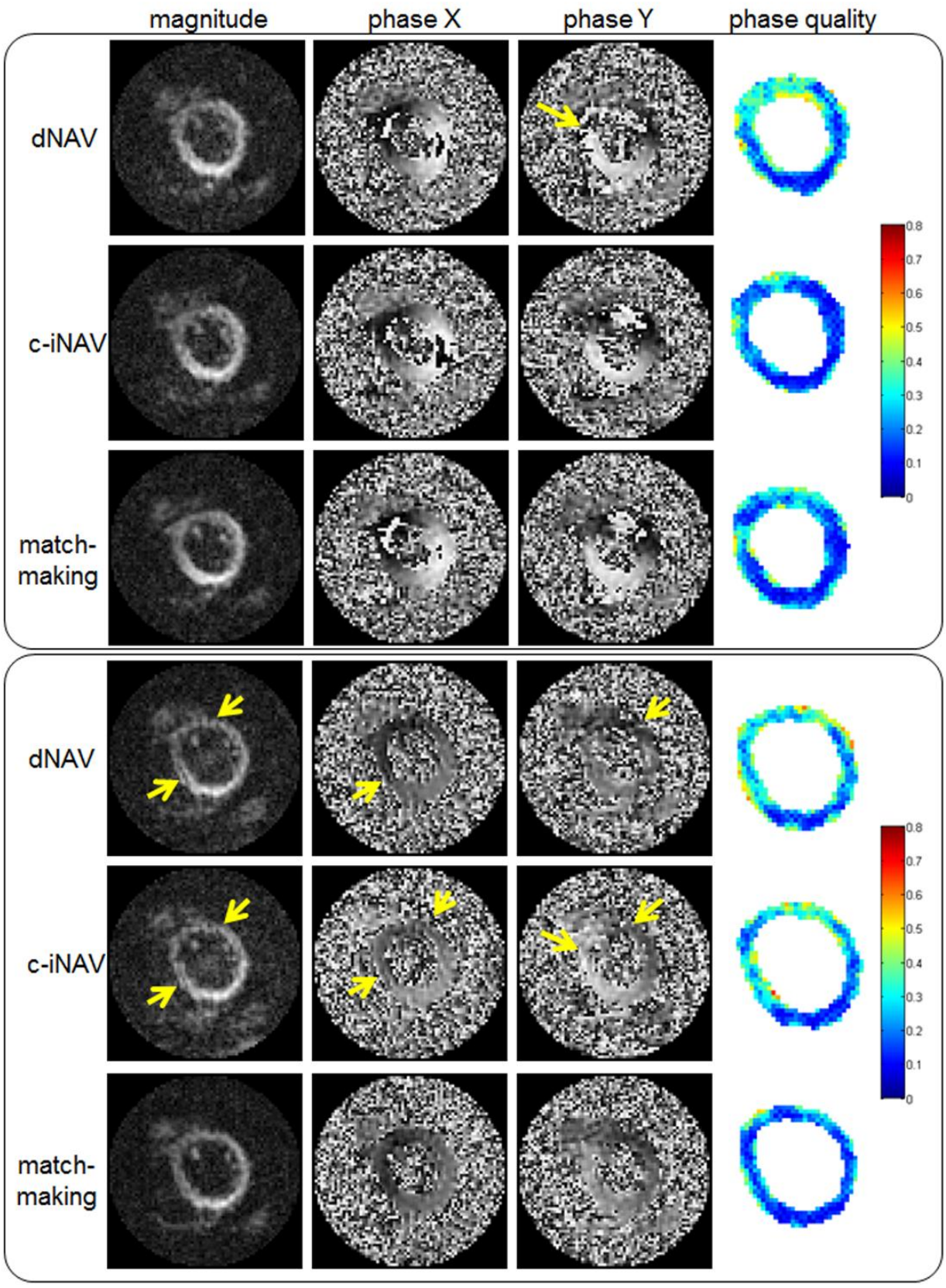
magnitude
phase X
phase Y
phase quality
dNAV
c-iNAV
match-making
dNAV
c-iNAV
match-making
0.8
0.7
0.6
0.5
0.4
0.3
0.2
0.1
0

Figure 2.7. Example DENSE images reconstructed using the conventional dNAV method, the c-iNAV method and the match-making framework for the same free-breathing volunteer raw data. An end-systolic frame (top box) and a diastolic frame (bottom box) are shown. The magnitude reconstructed images of the match-making method demonstrate lower artifact level, higher apparent SNR and better edge definition. The phase images of the match-making method have smoother phase in the myocardial ROI (arrows), and this is reflected in the better phase quality maps.

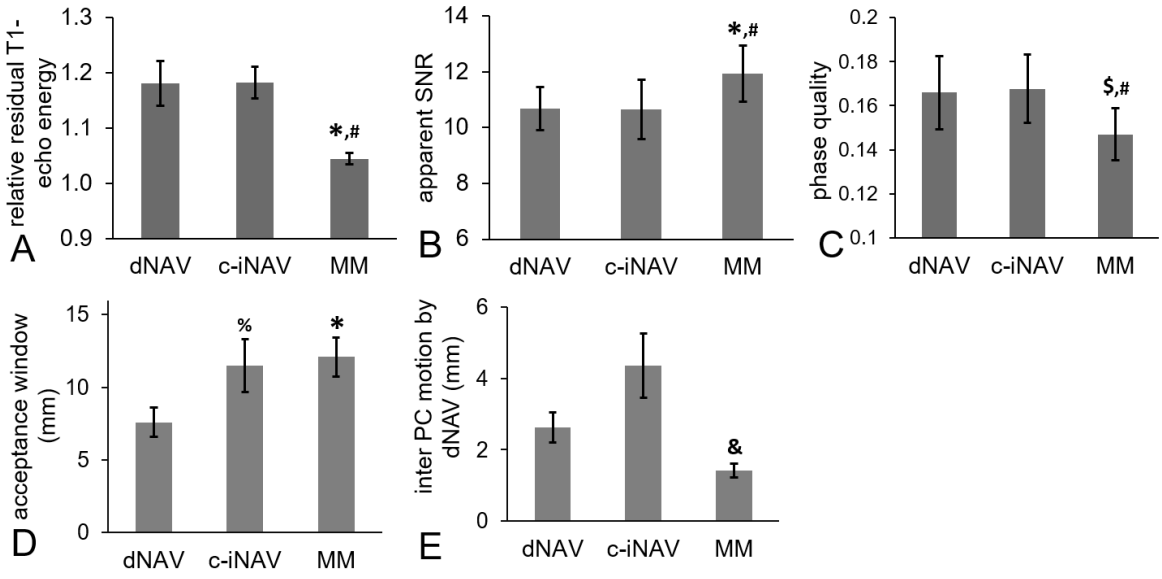

Figure 2.8. Quantitative comparisons for DENSE reconstructions using the match-making framework (MM) and the conventional dNAV and c-iNAV methods. (A) The relative residual T_1-relaxation echo energy was lower for MM (*P<0.05 vs. dNAV; #P<0.05 vs. iNAV). (B) The apparent SNR of magnitude reconstructed images was higher for MM. (C) The phase quality of phase images was better for MM compared to c-iNAV and trended to be better compared to the dNAV method ($P=0.06 vs. dNAV). (D) The match-making framework had a larger total acceptance window than the dNAV method, indicating that it accepted data from a wider range of respiratory phases (%P=0.08 vs. dNAV). (E) The motion within phase-cycled interleave pairs was smaller for MM than for the c-iNAV method (&P<0.05 vs. iNAV, one-way repeated measures ANOVA on ranks), indicating that the match-making framework identified phase-cycled interleaves at closer respiratory phases.

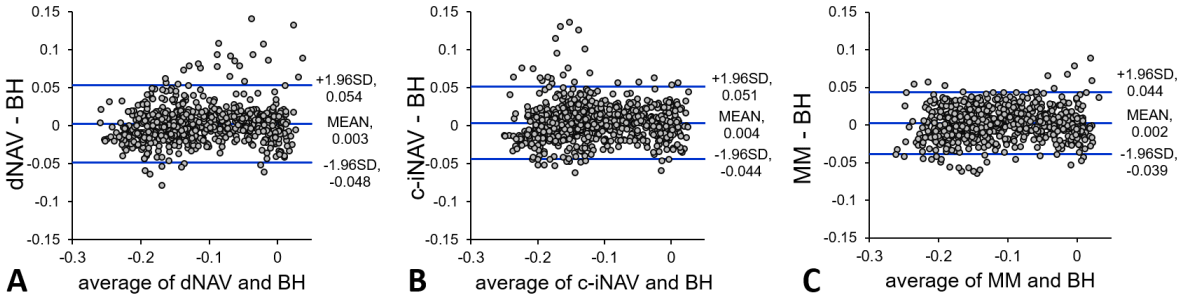

Figure 2.9. Comparison of agreement of circumferential strain from free-breathing acquisitions with that from breath-holding acquisitions for each reconstruction method. The match-making framework (MM, panel C) provided better agreement of strain with breath-holding acquisitions (BH) than the conventional dNAV and c-iNAV methods (panels A, B).

2.4 Discussion

A framework for self-navigated free-breathing cine DENSE MRI was developed and evaluated. The framework addressed two consequences of motion - striping artifacts due to incomplete suppression of the T_1 -relaxation echo and blurring. While a conventional iNAV approach is complicated by the presence of the T_1-relaxation echo, the in vivo data showed that low post-subtraction residual T_1-echo energy is a simple and useful metric to indicate whether phase-cycled DENSE interleaves were acquired at matched respiratory phases. While low residual T1-echo energy was shown to be effective for matching phase-cycled interleaves, this metric alone does not provide information about the absolute position of the heart and cannot be used for motion compensation of post-subtraction data. However, ste-iNAVs reconstructed from interleaves acquired at matched locations are localized, not contaminated by T_1 -relaxation echo artifacts, and can be used to accurately and automatically estimate in-plane heart motion due to respiration. Indeed, ste-iNAV motion estimation correlated better than conventional iNAV motion estimation with dNAV-measured respiratory motion, and the results further showed that the match-making framework reconstructions provided higher apparent SNR and a trend toward better phase quality for free-breathing cine DENSE than did the dNAV or c-iNAV reconstructions applied to the same raw data.

Both in-plane and through-plane motion can lead to changes in the complex T_1-relaxation echo and, subsequently, to an increase of the residual T_1-echo energy after subtraction of phase-cycled interleaves. In-plane displacement causes a phase shift of the k-space domain data. For through-plane motion, different tissue contributes to the different T_1 -relaxation echoes. Both types of motion lead to residual signal after subtraction of the phase-cycled interleaves. Although the underlying motion mechanisms leading to reduced T_1-echo energy are different for in-plane and through-plane motion, in both cases low values of residual T_1-echo energy identify phase-cycled interleaves acquired at matched locations.

Respiratory motion estimated by the ste-iNAVs correlated well with dNAV motion, as shown in Figure 2.6G, whereas respiratory motion estimated by c-iNAVs had an overall lower correlation across all subjects. Furthermore, motion estimation using the ste-iNAVs was completely automatic, without needing manual definition of a region of interest. These results were obtained because the ste-iNAVs were designed to have suppression of the T_1-relaxation echo and localized generation of the stimulated echo. In addition, because c-iNAVs are reconstructed from data prior to phase-cycling subtraction, they consist of signal from both the stimulated echo and the T_1-relaxation echo. Even with PCA-based filtering and/or low-pass filtering, our experience showed that these iNAVs can still be corrupted by the T_1-relaxation echo and are not well-localized to the heart. Therefore, the c-iNAVs are poorly-suited for respiratory motion estimation for cine DENSE. With these results, the match-making framework accepts data from any respiratory position and uses motion estimation and motion correction, while the dNAV and c-iNAV methods use retrospective gating but do not employ motion estimation and correction.

The total acceptance window, as defined by the full range of diaphragm positions for all accepted data, was greater for the match-making framework and trended to be larger for the c-iNAV method than for the conventional dNAV method. However, the motion between phase-cycled interleaves, as measured by the corresponding diaphragm positions, was lower for the match-making framework compared to the c-iNAV method. The lower amount of motion between phase-cycled interleaves led to a lower residual T_1-echo energy and high-quality ste-iNAVs for the match-making framework. Even though the total acceptance window was large, the high-quality ste-iNAVs provided good

motion estimation and compensation, and altogether the match-making framework with motion estimation and compensation produced higher apparent SNR and better phase quality in human subjects than the c-iNAV method. This further demonstrated that the c-iNAV method was not suitable for self-navigation for free-breathing cine DENSE imaging.

A number of evaluations utilized dNAV position, including the correlation between rT1E and dNAV differences within phase-cycling pairs (Figure 2.5D), comparison of motion estimation with ste-iNAV and c-iNAV (Figure 2.6F, G), and calculation of inter phase-cycling motion (Figure 2.8E). However, it is important to note that in these evaluations dNAV was only considered as a measure that other metrics can be compared with rather than the gold standard of respiratory motion estimation.

While the simple method for displacement encoding was used in this study, another option would have been to use the balanced displacement-encoding method [17]. With simple encoding, for the phase reference acquisition, the stimulated echo and T_1-relaxation are overlaid in k-space, which is non-ideal for matchmaking (although matchmaking does still work for this case). The balanced displacement encoding method more naturally separates the stimulated echo and T_1 relaxation echo in k-space for all displacement-encoding dimensions and avoids the overlay problem. In the present study, the simple method was chosen because it leads to less phase wrapping [17]. Nonetheless, in the future balanced encoding may be better suited for use with matchmaking, perhaps when used in combination with lower displacement-encoding frequencies or more effective phase-unwrapping algorithms.

Having established that the residual T_1-echo energy is an effective metric for identifying spiral phase-cycled interleaves acquired at matched locations, this metric may be used to develop an adaptive data acquisition strategy for efficient free-breathing self-navigated cine DENSE. Similar to the diminishing variance algorithm that was previously applied to conventional navigator data [23], an adaptive strategy would be to acquire an initial complete set of spiral interleaves, compute all the residual T_1-echo energies in real time, and then to reacquire interleaves with the highest residual T_1-echo energy until all interleaves have an acceptably low residual T_1-echo energy. Such an approach may provide high-quality free-breathing cine DENSE images with improved time efficiency.

A limitation of the current approach was that an off-resonance deblurring correction for spiral imaging was not employed due to the fact that the field map acquisition was not localized to the heart and therefore the reduced field-of-view was not applied for field map acquisitions. However, the spiral readout was shortened to largely account for the effects of off-resonance. In the protocol employed in this study, the repetition time was not set to its shortest possible value, as using the minimum TR would have led to a lower SNR. Instead, TR = 15 ms was selected in order to maintain an SNR similar to prior studies [18].

In addition, the present motion estimation and compensation methods only considered two-dimensional in-plane translation. Combining stimulated echoes with differing through-plane motions may lead to suboptimal images, and methods to reject, accept, and/or correct for through-plane motion may need to be developed in the future. Another limitation of the study is that only healthy volunteers were scanned. The method will be applied in patients after implementation of the adaptive acquisition strategy in order to acquire data more efficiently. Presently all image reconstruction was performed offline. In the future, an online version of the match-making framework should be implemented. Lastly, the measured improvements in apparent SNR, phase quality and strain compared to the dNAV and c-iNAV methods were modest. It is likely that the improvements were not greater because our experiments involved the acquisition of only three repetitions and used a predefined acquisition order, which limited the degree to which respiratory phases could be closely matched and to which the residual T_1-echo energy could be fully minimized. The envisioned real-time adaptive approach to match-making is expected to overcome this limitation, may provide good suppression of the T_1-relaxation echo for all interleaves, and may provide greater advantages compared to conventional navigator methods.

The match-maker iNAV concept for free-breathing scans may be generalizable to other MRI acquisitions that utilize phase-cycled subtractions to suppress signals, such as myocardial tagging using complementary spatial modulation of magnetization [24, 25], localized spectroscopy [26], and $T_{1\rho}$ imaging [27] with phase cycling.

In conclusion, the match-making framework with motion estimation and compensation addresses both the striping and blurring effects of respiratory motion in free-breathing cine DENSE and provides advantages compared to conventional dNAV

and c-iNAV methods. Nonetheless, adaptive acquisition strategies based on the match-making framework as well as compensation for through-plane motion may enable efficient and high-quality free-breathing cine DENSE imaging with simple setup procedures in clinically-applicable scan times.

2.5 Appendix

Principle component analysis (PCA) to separate signals for improved conventional cine DENSE iNAVs

In this study, respiratory motion estimation was assessed using the match-maker ste-iNAV method and a conventional iNAV method. For the conventional iNAV method, the T_1-relaxation echo led to very poor quality iNAVs and very poor motion estimation performance. To get improved performance, PCA was applied to the iNAV data to separate the stimulated-echo and T_1 -relaxation-echo signals, and iNAVs were reconstructed after removal of the main T_1-relaxation-echo component.

As shown in Supporting Figure 2.10A, preliminarily iNAVs were organized into a spatiotemporal Casorati matrix, S, where each column represents the pixels from each iNAV [28]. PCA was performed to decompose the matrix, S, into spatial and temporal bases. Figure 2.10B-G shows the first and second spatial bases in the image and k-space domains, and also shows their temporal bases, respectively. The first spatial basis in the image and k-space domains and the first temporal basis were found to predominantly represent the T_1-relaxation-echo signal (Figure 2.10, B-D). The second spatial basis in the image and k-space domains and the second temporal basis were found to predominantly represent the stimulated-echo signal (Figure 2.10, E-G). After the first principal component was removed and a low-pass filter was applied to the k-space data to further suppress the residual T_1-relaxation-echo signal, iNAVs were reconstructed from the k-space data.

Demonstration of the effect of PCA-based and low-pass filtering on the iNAVs is shown in Figure 2.11. Without filtering, the iNAV has a strong T_1 relaxation signal outside the heart (predominantly fat signal from chest wall in this example) (Figure 2.11A, white arrow), while the iNAV reconstructed with filtering shows better suppression of

the signal outside the heart (Figure 2.11C). By using manually-tracked iNAVs as a reference, automatic motion estimation using cross-correlation applied to iNAVs with PCA-based and low-pass filtering had better performance for estimating the motion of the heart due to respiration, whereas motion estimation applied to iNAVs without PCA-based filtering had worse performance (Figure 2.11, E, F).

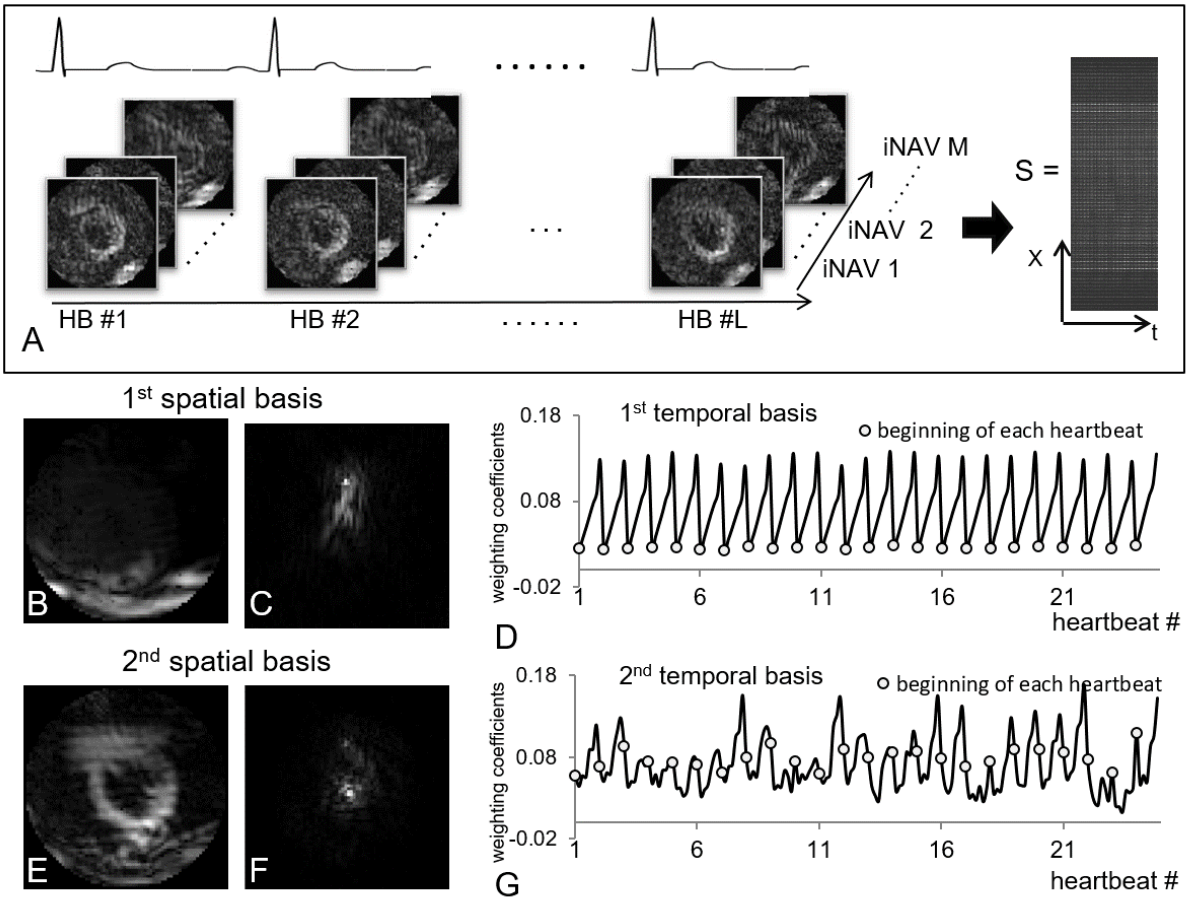

Figure 2.10. Diagram of PCA-based filtering for improved cine DENSE conventional iNAVs. (A) Free-breathing cine DENSE data were acquired over multiple heartbeats. Within each heartbeat, multiple iNAVs are reconstructed by combining 8 consecutive spiral interleaves. All the iNAVs are organized into a Casorati matrix (**S**) where each column represents the pixels from each iNAV. (B-G): Results of PCA applied to the matrix **S**. The first principle component is predominantly the T_1-relaxation signal as shown in the image (B), k-space (C) and the corresponding temporal basis (D). The second principle component is mainly the stimulated echo (E-G). PCA-filtering to remove the first principle component provides an improved c-iNAV.

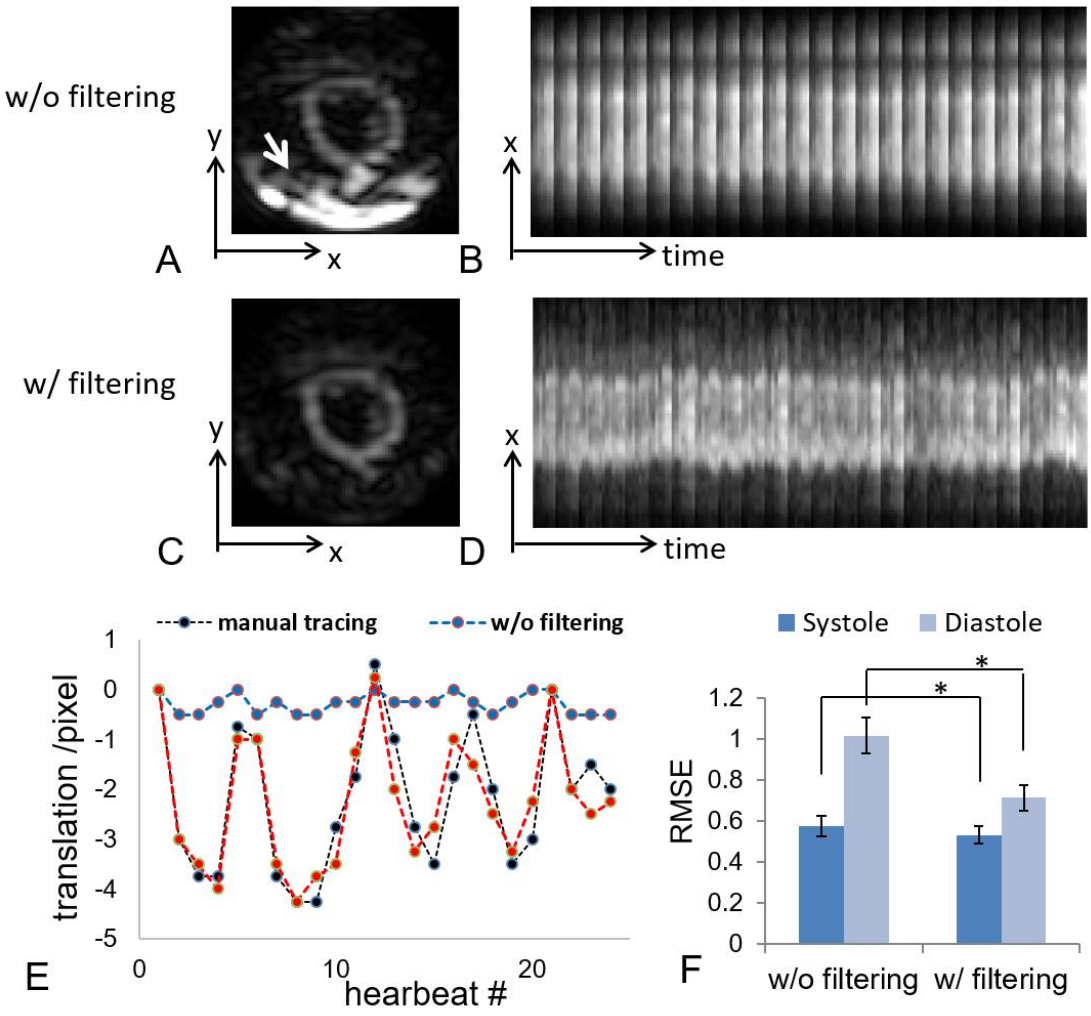

Figure 2.11. Comparison of image quality and motion estimation accuracy of conventional iNAVs reconstructed without and with PCA-based filtering. (A-D) Example c-iNAVs and projections in the x-direction. The filtered images have markedly less T_1 relaxation signal (arrow). Projections with PCA-based filtering show better visualization of respiratory motion (D vs. B). (E) Respiratory translations estimated by cross-correlation using the c-iNAV images without (w/o) and with (w/) PCA-based filtering. Results of manual tracing of the heart from the images reconstructed without filtering are shown as the reference. The motion estimated from c-iNAVs with PCA-based filtering closely matches the manual tracing results while the motion from images without PCA-based filtering is not accurate. (F) Accuracy of motion estimated from iNAVs by root-mean-squared-error (RMSE) relative to manual tracing (*P<0.05, paired t-test, N = 6). For both systole and diastole, motion estimated with iNAVs with PCA-based filtering has significantly less error than that without filtering.

2.6 References

1. Kim, D., et al., *Myocardial tissue tracking with two-dimensional cine displacement-encoded MR imaging: development and initial evaluation.* Radiology, 2004. **230**(3): p. 862-871.
2. Young, A.A., et al., *Generalized spatiotemporal myocardial strain analysis for DENSE and SPAMM imaging.* Magnetic resonance in medicine, 2012. **67**(6): p. 1590-1599.
3. Lin, K., et al., *Reproducibility of cine displacement encoding with stimulated echoes (DENSE) in human subjects.* Magnetic resonance imaging, 2017. **35**: p. 148-153.
4. Gilliam, A.D. and F.H. Epstein, *Automated motion estimation for 2-D cine DENSE MRI.* IEEE transactions on medical imaging, 2012. **31**(9): p. 1669-1681.
5. Goto, Y., et al., *Comparison of Displacement Encoding With Stimulated Echoes to Magnetic Resonance Feature Tracking for the Assessment of Myocardial Strain in Patients With Acute Myocardial Infarction.* The American Journal of Cardiology, 2017. **119**(10): p. 1542-1547.
6. Kihlberg, J., et al., *Clinical experience of strain imaging using DENSE for detecting infarcted cardiac segments.* Journal of Cardiovascular Magnetic Resonance, 2015. **17**(1): p. 50.
7. Zhong, X., et al., *Imaging three‐dimensional myocardial mechanics using navigator‐gated volumetric spiral cine DENSE MRI.* Magnetic resonance in medicine, 2010. **64**(4): p. 1089-1097.
8. Winkelmann, S., et al., *An optimal radial profile order based on the Golden Ratio for time-resolved MRI.* IEEE transactions on medical imaging, 2007. **26**(1): p. 68-76.
9. Kim, Y.C., S.S. Narayanan, and K.S. Nayak, *Flexible retrospective selection of temporal resolution in real‐time speech MRI using a golden‐ratio spiral view order.* Magnetic resonance in medicine, 2011. **65**(5): p. 1365-1371.
10. Mills, P., et al., *Localized imaging using stimulated echoes.* Magnetic resonance in medicine, 1987. **5**(4): p. 384-389.
11. Aletras, A.H., R.S. Balaban, and H. Wen, *High-resolution strain analysis of the human heart with fast-DENSE.* Journal of Magnetic Resonance, 1999. **140**(1): p. 41-57.
12. Walsh, D.O., A.F. Gmitro, and M.W. Marcellin, *Adaptive reconstruction of phased array MR imagery.* Magnetic Resonance in Medicine, 2000. **43**(5): p. 682-690.
13. Ehman, R.L. and J.P. Felmlee, *Adaptive technique for high-definition MR imaging of moving structures.* Radiology, 1989. **173**(1): p. 255-263.

14. Fessler, J.A. and B.P. Sutton, *Nonuniform fast Fourier transforms using min-max interpolation.* IEEE Transactions on Signal Processing, 2003. **51**(2): p. 560-574.
15. Wehner, G.J., et al., *Validation of in vivo 2D displacements from spiral cine DENSE at 3T.* Journal of Cardiovascular Magnetic Resonance, 2015. **17**(1): p. 5.
16. Fahmy, A.S., E.-S.H. Ibrahim, and N.F. Osman, *Spectrally-Presaturated Modulation (SPM): An efficient fat suppression technique for STEAM-based cardiac imaging sequences.* Magnetic resonance imaging, 2017. **37**: p. 209-215.
17. Zhong, X., P.A. Helm, and F.H. Epstein, *Balanced multipoint displacement encoding for DENSE MRI.* Magnetic resonance in medicine, 2009. **61**(4): p. 981-988.
18. Bilchick, K.C., et al., *Impact of mechanical activation, scar, and electrical timing on cardiac resynchronization therapy response and clinical outcomes.* Journal of the American College of Cardiology, 2014. **63**(16): p. 1657-1666.
19. Gudbjartsson, H. and S. Patz, *The Rician distribution of noisy MRI data.* Magnetic resonance in medicine, 1995. **34**(6): p. 910-914.
20. Dietrich, O., et al., *Influence of multichannel combination, parallel imaging and other reconstruction techniques on MRI noise characteristics.* Magnetic resonance imaging, 2008. **26**(6): p. 754-762.
21. Ghiglia, D.C. and M.D. Pritt, *Two-dimensional phase unwrapping: theory, algorithms, and software*. Vol. 4. 1998: Wiley New York.
22. Spottiswoode, B.S., et al., *Tracking myocardial motion from cine DENSE images using spatiotemporal phase unwrapping and temporal fitting.* IEEE transactions on medical imaging, 2007. **26**(1): p. 15-30.
23. Sachs, T.S., et al., *The diminishing variance algorithm for real‐time reduction of motion artifacts in MRI.* Magnetic resonance in medicine, 1995. **34**(3): p. 412-422.
24. Axel, L. and L. Dougherty, *MR imaging of motion with spatial modulation of magnetization.* Radiology, 1989. **171**(3): p. 841-845.
25. Axel, L. and L. Dougherty, *Heart wall motion: improved method of spatial modulation of magnetization for MR imaging.* Radiology, 1989. **172**(2): p. 349-350.
26. Knight-Scott, J., D.D. Shanbhag, and S.A. Dunham, *A phase rotation scheme for achieving very short echo times with localized stimulated echo spectroscopy.* Magnetic resonance imaging, 2005. **23**(8): p. 871-876.

27. Li, X., et al., *In vivo 3T spiral imaging based multi - slice T1ρ mapping of knee cartilage in osteoarthritis.* Magnetic resonance in medicine, 2005. **54**(4): p. 929-936.

28. Lingala, S.G., et al., *Accelerated dynamic MRI exploiting sparsity and low-rank structure: kt SLR.* IEEE transactions on medical imaging, 2011. **30**(5): p. 1042-1054.

Chapter 3
Adaptive acquisition by diminishing residual T_1-echo energy

3.1 Introduction

Cine displacement encoding with stimulated echoes (DENSE) MRI [1] is well-established strain imaging technique. Recent studies demonstrated the potential of cine DENSE for detection of subclinical myocardium dysfunction and patient treatment stratification [2-4]. Cine DENSE acquisition is typically performed during breath-holding and multiple breath-holds are required per exam [1, 5]. However, such protocols can be challenging in patient populations such as heart failure, pediatrics, and others [5]. In practice, imperfect breath-holds lead to repetitions of acquisitions and reduce imaging efficiency. A reliable free-breathing method can overcome these challenges.

Among the various techniques for free-breathing cardiac MRI, diaphragm-based navigator (dNAV) [6] was implemented for cine DENSE and was able to reduce breathing artifacts [7, 8]. However, the dNAV method requires extra scout scans and results in variable imaging quality and efficiency [9, 10]. A better solution for free-breathing cardiac MRI is self-navigation where the respiration information is extracted from the imaging data itself and used for motion compensation.

In Chapter 2, a self-navigated reconstruction framework for free-breathing cine DENSE was presented [11]. The method addressed two major types of artifacts, striping, and blurring due to inter-heartbeat respiratory motion in free-breathing cine DENSE [11]. Cine DENSE imaging signal contains two echoes, the displacement-encoded stimulated echo and the artifact-generating T_1-relaxation echo [1]. Typically, two phase-cycled datasets during different heartbeats are acquired and subtracted to suppress the T_1-relaxation echo [12]. With free-breathing, the suppression is not effective with the subtraction, which leads to striping artifacts. Phantom and in vivo experiments

demonstrated that the residual energy of the T_1-relaxation echo (rT1E) after phase-cycling subtraction increased as the motion between the phase-cycled datasets increased. Minimal rT1E of the post-subtraction data identified phase-cycling pairs that were acquired at similar respiratory positions and reduced striping artifacts. After match-making of phase-cyclings, stimulated-echo only image-based navigators (ste-iNAVs) were reconstructed from the post-subtraction k-space data. In-plane motion due to respiration was then estimated with the ste-iNAVs and corrected to reduce blurring.

However, this reconstruction framework still had a few drawbacks. The image quality was not guaranteed and the imaging efficiency was not optimized. The reconstruction was performed retrospectively after the data acquisition was completed with a prescribed protocol. DENSE data were acquired with three repetitions to provide multiple candidates of phase-cycling pairs and a better chance of suppressing the T_1-relaxation echo sufficiently rather than acquiring each phase-cycling just once. Yet, such a protocol cannot guarantee high-quality free-breathing cine DENSE as the number of repetitions necessary may vary from subject to subject. Simply increasing the repetition number increases the possibility of matching phase-cycling data for every k-space segment but reduces imaging efficiency. Using real-time feedback on rT1E to guide data acquisition can potentially guarantee sufficient suppression of the T_1-relaxation echo and preserve the imaging efficiency.

In addition to blurring, respiratory motion within each heartbeat (intra-heartbeat motion) can induce phase errors in the stimulated-echoes. In cine DENSE, tissue motion is encoded into the phase of the stimulated-echoes. The motion-related phase is linear with the displacement of the tissue that happens between application of the preparation pulses and the k-space data acquisition. Along with the myocardial displacement with the heart contracting and relaxing periodically, the bulk movement of the heart due to respiration is also encoded into the stimulated-echo signal. The intra-heartbeat motion induced phase is likely to be greater during diastole than during systole because diastole is later from the application of preparation pulses. This phase is also likely to be different during different heartbeats. Such variations of intra-heartbeat motion and phase errors can cause signal cancellation artifacts and significantly degrade image quality. These signal cancellation artifacts are similar to those reported in diffusion weighted imaging [13, 14] and MR elastography [15] and should be properly compensated.

The purpose of the work presented in this chapter is to develop an adaptive imaging algorithm that uses real-time feedback to reduce rT1E adaptively during the acquisition. The reconstruction applies phase correction to reduce signal cancellation due to the intra-heartbeat motion. Three stopping criteria for the adaptive acquisition algorithm are proposed and experiments in healthy subjects were conducted to determine the criterion values.

3.2 Methods

3.2.1. Adaptive acquisition algorithm to minimize rT1E

The proposed algorithm for cine DENSE data acquisition with free-breathing is shown in Figure 3.1. The overall objective is to reduce the rT1E of the post-subtraction data. The algorithm starts with the acquisition of fully-sampled k-space datasets for both phase-cycling dimensions, i.e. one phase-cycling pair for each k-space segment. In the online reconstruction environment, phase-cycling subtraction is performed for each phase-cycling pair and the rT1E values are calculated by summing post-subtraction k-space energy in a predefined region. Afterward, the rT1E values are examined to determine whether the existing data satisfy the stopping criteria. If not, the segment with the highest rT1E values is determined as the target segment and a real-time feedback is delivered to the data acquisition environment which then repeats acquisition of the target segment. With the new data, the online reconstruction calculates the rT1E values of the new phase-cycling pairs and updates the best-matched phase-cycling pair for the target segment, i.e. selecting the pair that has the lowest rT1E. After the update, the rT1E values are examined again. If one of the stopping criteria is satisfied, the acquisition stops; otherwise, the acquisition continues. During each iteration, the algorithm acquires another instance of the target segment for both phase-cycling dimensions. In other words, the acquisition takes 2 heartbeats at each iteration. Cine DENSE acquires a number of scans depending on the displacement encoding methods prescribed. In this chapter, each of these scans is referred to as an encoding dimension. The adaptive acquisition process is repeated for each encoding dimension until all encoding dimensions are acquired.

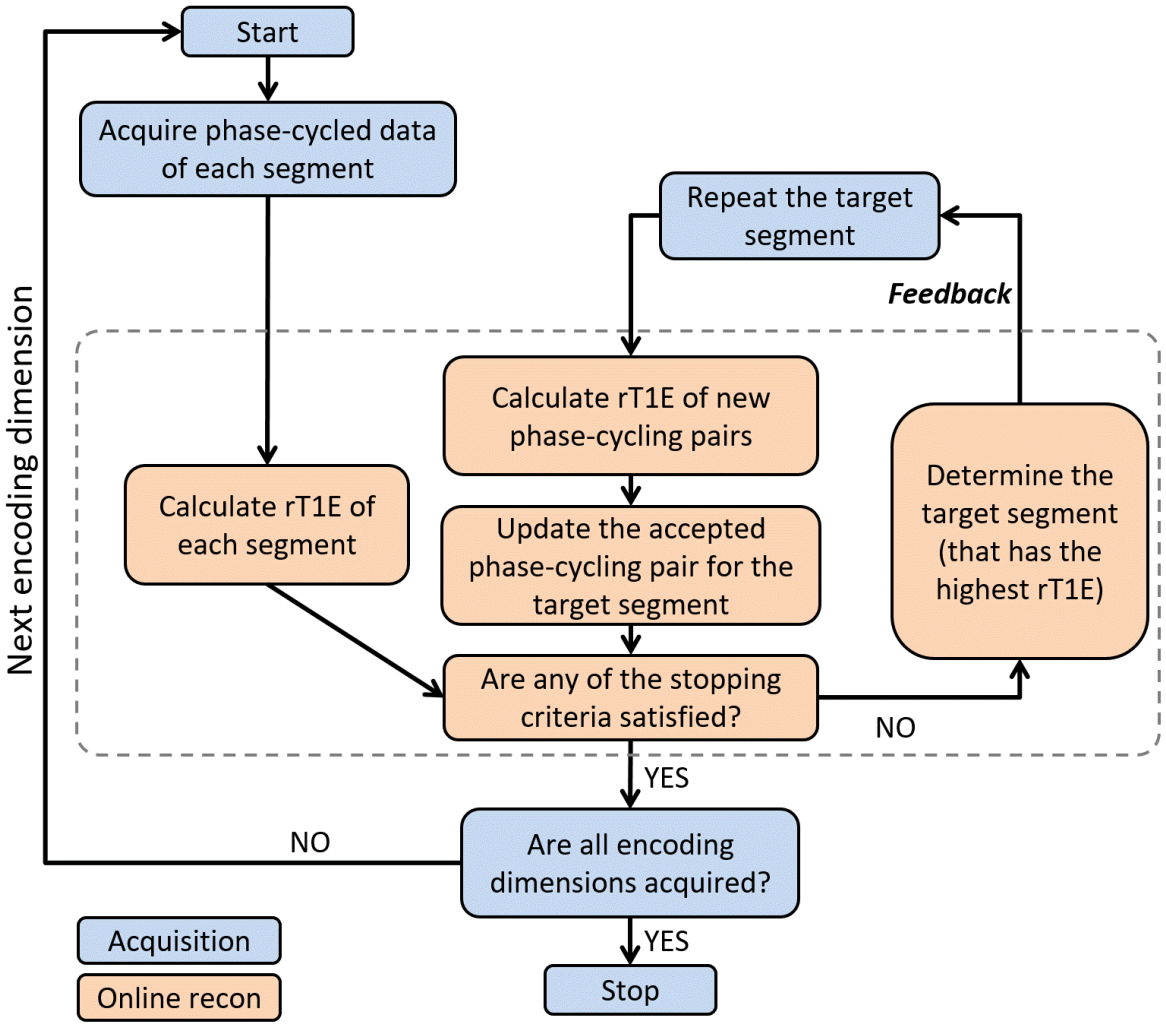

Figure 3.1. Diagram of the adaptive acquisition algorithm. The algorithm initializes by acquiring a complete set of k-space data, i.e. one instance of both phase-cycling dimensions for each segment. Then the online reconstruction environment performs subtraction of each phase-cycling pair and calculates the residual T_1-echo energy (rT1E) of each segment. The algorithm then compares the rT1E values with the stopping criteria. If they are not satisfied, then the algorithm determines the target segment with the highest rT1E and delivers the feedback to the sequence. Then the algorithm acquires another instance of the target segment for both phase-cycling dimensions. With the new data, the online reconstruction calculates the rT1E for each new phase-cycling pair and updates the best-matched phase-cycling pair for the target segment, i.e. selects the pair with the lowest rT1E. Afterward, the algorithm examines the rT1E again. The process continues until one of the stopping criteria is satisfied. The algorithm repeats the process for each encoding dimension separately and stops when all encoding dimensions are acquired.

3.2.2. Implementation

The adaptive acquisition algorithm was implemented based on a 2D spiral cine DENSE sequence that supports localized generation of the stimulated echoes [16]. Localized generation of the stimulated echoes was achieved by using two 90-degree RF pulses that are slice-selective in the orthogonal directions in the imaging plane for displacement-encoding preparation [11]. As a result, the stimulated-echo signal only originates from the region where the two slice profiles intersect. Uniform rotation of the trajectory through cardiac frames was implemented. With these methods, image-based navigators (iNAV) can be reconstructed by combining spiral data of consecutive frames. These iNAVs are reconstructed after subtraction of matched phase-cycling pairs and therefore only include the stimulated-echo (ste-iNAV) and are heart-localized. As shown in Figure 3.2, the loop structure of the data acquisition is modified to have phase-cycling dimension inside of the segment loop compared to that in Figure 2.3.

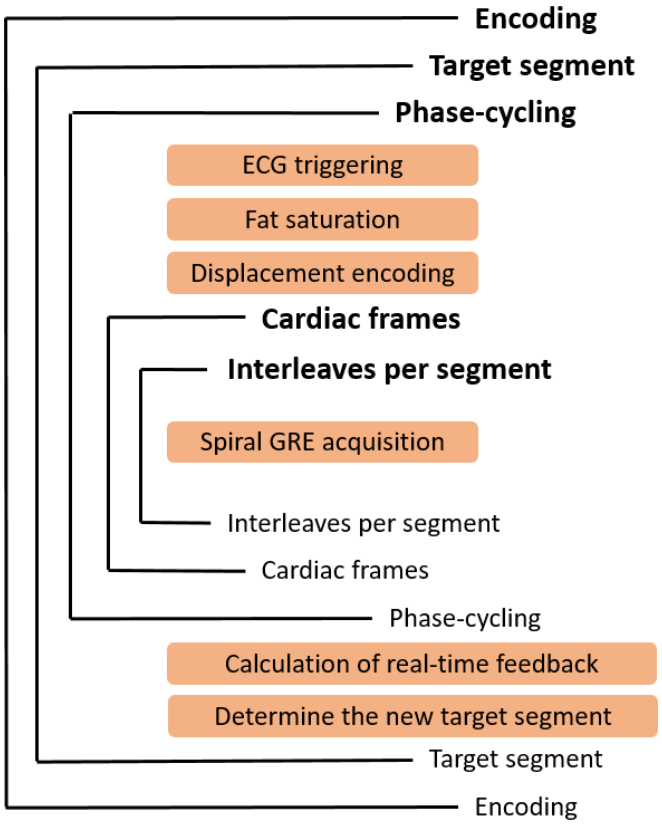

Figure 3.2. Modified loop structure for data acquisition with the adaptive algorithm.

3.2.3. Stopping criteria

Specifically, there are three criteria in the current design: (1) The relative rT1E is below a threshold for all the cardiac frames; (2) The decrease percentage of rT1E is below a threshold; 3) The imaging time reaches a maximum limit. The imaging stops for the current encoding dimension when any of the criteria is satisfied.

The first criterion requires the rT1E to be sufficiently low. The relative rT1E is calculated by normalizing the absolute rT1E to an estimated baseline value. Ideally, when the T1-relaxation echo is canceled perfectly, the rT1E is the energy of the displacement-encoded stimulated-echo in the predefined k-space region. Therefore, the rT1E should decrease and converge as the T_1-relaxation echo gets better suppressed. The absolute rT1E depends on various factors such as subject load, number of coils, and flip angle, etc. Therefore, the algorithm may not converge to the same value among different subjects and scans. However, the T_1-relaxation echo energy grows within the cardiac cycle when the phase-cycled data is not matched and the rT1E is always greater in diastole (frame # > 15) than in systole (frame # < 15) as shown in Figure 2.5C. Therefore, the average rT1E of frames during early systole (trigger time <= 300 ms) is calculated as the baseline rT1E and the absolute rT1E is normalized to the baseline as the relative rT1E. The baseline value is updated as well at each iteration.

The second and third criteria prevent the algorithm from imaging for too long. During the acquisition, it may take more than one iteration for the rT1E to be updated. However, if the rT1E does not change or decreases only marginally over a long time, it may indicate that the rT1E cannot be reduced further even when the first criterion is not satisfied. A maximum imaging time of 30 heartbeats per encoding dimension is used as the third criterion. The k-space region used for rT1E is defined as $|k| > |k_{max}|/2$.

3.2.4. Compensation for motion in the stimulated echoes

To compensate for inter-heartbeat motion, 2D translations are estimated with the ste-iNAVs by 2D cross-correlation. The translations are then corrected in the k-space data as described in Chapter 2. The translation estimation and correction are first performed among the segments of each encoding dimension and then among the encoding

dimensions. Ste-iNAVs are reconstructed again from the translation corrected k-space data for the next step of intra-heartbeat motion compensation.

In order to reduce the signal cancellation artifacts, phase error due to intra-heartbeat motion is estimated and compensated. Here, only the phase due to translations is considered, i.e. the correction is a spatially-invariant [13]. Figure 3.2A-C illustrates the estimation of the phase correction values for each k-space segment. Within each encoding dimension, one segment is chosen as the reference segment and the other segments are corrected. The estimation is performed for each iNAV-frame by maximizing the energy of the combined image (complex sum) of the reference ste-iNAV and the corrected ste-iNAV. As shown in Figure 3.3A, the ste-iNAVs of the reference segment (S_{ref}) and the segment to be corrected (S_{cor}) have different phases (red arrows). The energy of the combined image of S_{ref} and S_{cor} with phase correction (θ) is defined as,

$$E(\theta) = \left\| S_{ref} + S_{cor} e^{-i\theta} \right\|_2 \qquad (3.1)$$

The $E(\theta: \theta \in (-\pi, \pi))$ for the example ste-iNAVs is shown in Figure 3.3B. The phase value that maximizes $E(\theta)$ is determined as the correction value for the current ste-iNAV frame. The process is performed for all the ste-iNAV frames as in Figure 3.3C (square markers). Then the phase correction values along the cardiac time are smoothed with a third order median filter (green markers) and linearly interpolated to estimate the correction for all the cardiac frames (pink curve). The phase error estimation is performed for each encoding dimension separately.

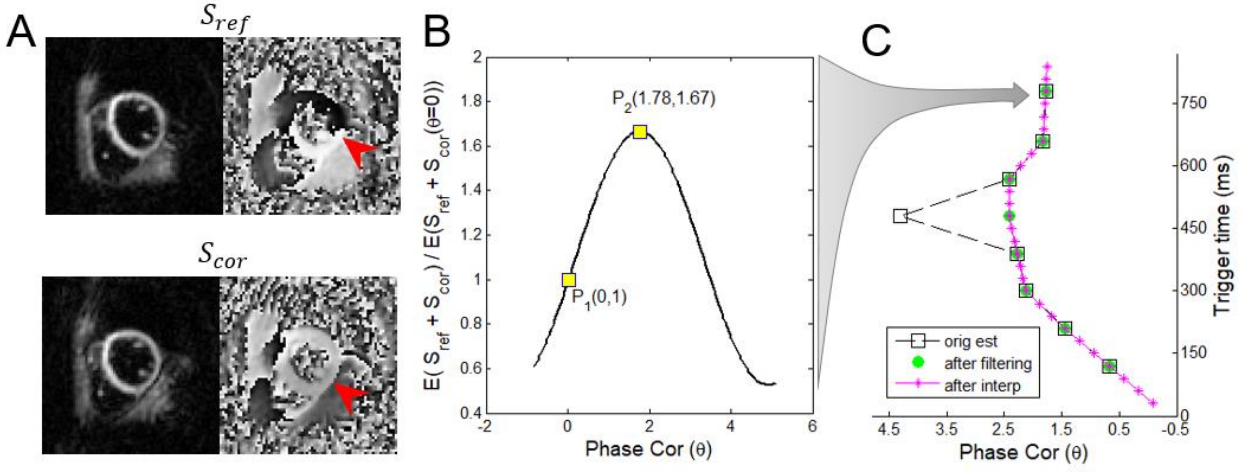

Figure 3.3. Illustration of phase error estimation based on ste-iNAVs. (A) ste-iNAVs at late diastole presenting the reference segment (S_{ref}) and the segment to be corrected (S_{cor}). The magnitude components of the two ste-iNAVs are similar to each other, while the phase components are different (red arrows), demonstrating the phase error due to intra-heartbeat motion. (B) The energy of the combined image (complex sum of S_{ref} and $S_{cor}e^{i\theta}$) as a function of phase correction values (θ). The presented data is normalized by the combined image energy without correction, i.e. P_1. The phase correction is determined as the one that maximizes the combined image energy (P_2). (C) Phase error estimation can be estimated for the ste-iNAVs (square markers). Median filtering is applied to remove noise in the estimation due to rapid heart motion during early diastole (green markers). Then the phase errors of all the cardiac frames are estimated by linear interpolation (pink markers).

3.2.5. Free-breathing cine DENSE data acquisition

To determine the threshold values for criteria (1) and (2), 10 healthy volunteers (6 female, 27 ± 4 years old) were scanned on a 3T MRI system (Magnetom Prisma, Siemens Healthineers, Erlangen, Germany) with a 32-channel spine coil and a 6-channel body coil. All human subject scans in this study were performed in accordance with protocols approved by the institutional review board and with informed consent. Free-breathing cine DENSE datasets were acquired using the adaptive algorithm with criterion (3) only (maximum imaging time of 30 heartbeats per encoding dimension) and on a mid-ventricular short-axis slice with the following parameters: slice thickness 8 mm, FOV = 320 x 320 mm^2, width of the localized stimulated-echo region = 90 ~ 110 mm, 6 spiral interleaves per image, 2 interleaves per segment, TR = 15 ms, temporal resolution = 30 ms, TE = 1.08 ms, spiral readout length of 5.5 ms, matrix size of 128 x 128, balanced displacement encoding with encoding frequency = 0.05 cyc/mm. Ramped flip angles with a final flip angle of 15 degrees were employed. Multiple frames were imaged with prospective ECG triggering covering approximately 80% of the RR interval. Fat suppression was applied immediately after ECG triggering. The imaging parameters were chosen in consistency with previous studies. The total scan time was 92 heartbeats with the first two heartbeats used for the acquisition of field map data.

3.2.6. Image reconstruction and image analysis

Cine DENSE images were reconstructed offline in MATLAB (MathWorks, Natick, MA) for each iteration. The reconstruction was performed in three ways: 1) NUFFT, 2) with additional phase error correction and 3) with both phase error correction and translation correction. The reconstruction was performed separately for each of the encoding dimensions. The final displacement phase images were not extracted as the end time points of the encoding dimensions were unknown. The relative rT1E values and image quality quantified as apparent SNR were analyzed for each iteration and each encoding dimension to determine the threshold of criterion (1). The relative rT1E was averaged through cardiac frames. The apparent SNR was quantified for a diastolic frame (trigger time = 600 ms). At each iteration when the rT1E was updated, the previous rT1E, percentage of decrease in rT1E and the time cost (number of heartbeats since the last rT1E update) were recorded to determine criterion (2). The center frequency shift was estimated from the field maps and corrected in k-space [17, 18].

In addition, the apparent SNR was quantified for reconstruction both without and with phase error correction. And the SNR increase because of the phase error correction was correlated with the mean phase correction values to analyze the contribution of phase error correction to image SNR.

3.3 Results

3.3.1. Improving image quality during the adaptive acquisition

Figure 3.3 demonstrates that the adaptive algorithm reduces rT1E and improves image quality efficiently during the acquisition. The first encoding dimension of the dataset is shown. The relative rT1E at each time during the acquisition is shown in Figure 3.4A. At beginning of the acquisition (time = 6 heartbeats), segment #3 was the target segment with the highest rT1E. Therefore, the algorithm repeated acquisition of this segment, after which the rT1E of segment #3 decreased (time = 8 heartbeats). Segment #1 then became new target segment and was repeated. The acquisition continued and after 20 heartbeats, the relative rT1E values of all segments were very low and the change was

small. The apparent SNR of the images at each time is shown in Figure 3.4B. The apparent SNR increased as the algorithm progressed, demonstrating improvement in the image quality. The rT1E of the cardiac cycle and images at 4 time points during the acquisition are shown in Figure 3.4C. Both the magnitude (mid column) and phase (right column) images at a late diastole frame are shown. The rT1E of all segments were high particularly in diastole and strong artifacts were present in the images at the initial stage of the acquisition (t_1). As the algorithm progressed, the rT1E of all segments and frames were reduced to close to 1.0 and the artifacts in the images were reduced ($t_2 - t_4$).

3.3.2. Motion correction with ste-iNAV improves image quality

Figure 3.5 shows the different reconstructions at t_4 in Figure 3.4C. The image reconstructed without phase error correction or translation correction (panels A, E) had severe signal cancellation due to intra-heartbeat motion induced phase errors. Translation correction (TC) reduced blurriness in the images (panels B, F). Reconstruction with phase correction (PhaCor) reduced signal cancellation (panels C, G). Together, the image quality is significantly improved (panels D, G). These results demonstrated that phase correction and translation correction are essential to compensate for motion in the stimulated-echoes to reduce breathing artifacts.

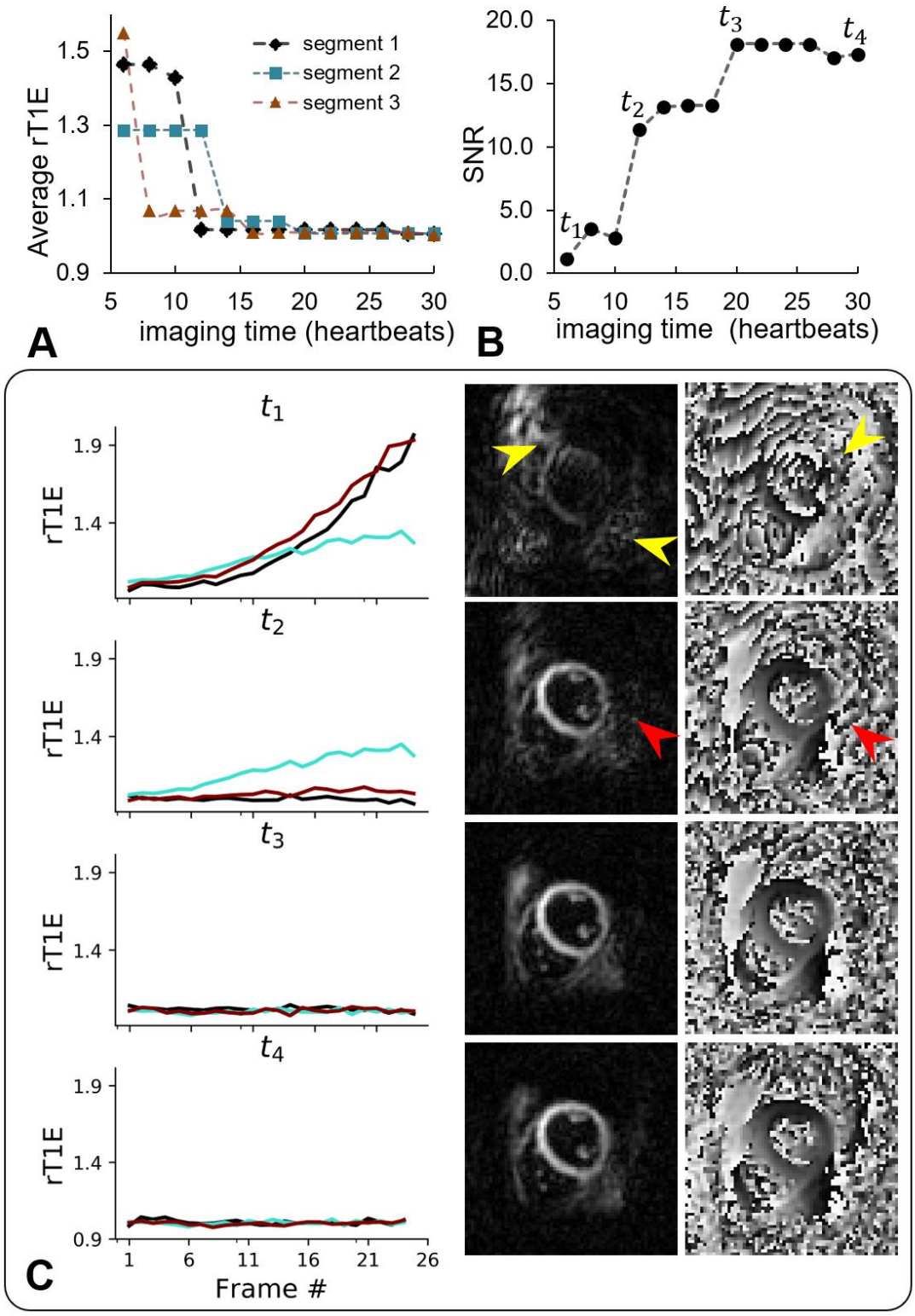

Figure 3.4. Results of a free-breathing cine DENSE dataset acquired with the adaptive imaging algorithm for a fixed duration of 30 heartbeats on a healthy subject. (A). The residual T_1-echo energy of each k-space segment decreased as the imaging progressed. (B). The

corresponding SNR of DENSE images increased. (C) The rT1Es of the post-subtraction data (left) and images of a diastolic frame (right, trigger time = 600 ms) at four different time points during the scan. These results demonstrate improving image quality during the adaptive acquisition as the rT1E decreased and converged.

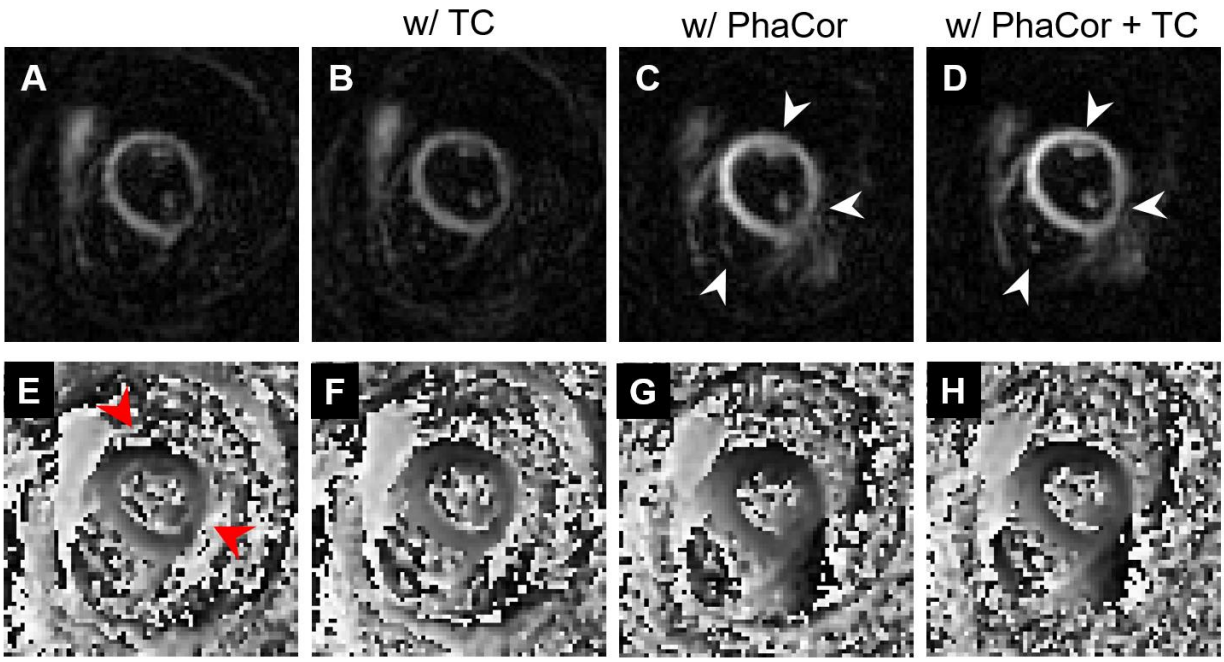

Figure 3.5. Reconstruction of the same dataset with different compensations. The dataset is the same as that in Figure 3.3, t_4. (A, E) The reconstruction without translation or phase error correction has a severe signal loss in the magnitude and errors in the myocardium phase (red arrows). (B, F) Reconstruction with correction for in-plane translation (TC) removed the blurriness. (C, G) Phase error correction (PhaCor) restores the magnitude SNR and removes errors in the phase image. (D, H) With both TC and PhaCor, the image quality is significantly improved with higher apparent SNR and sharper definition of the myocardial borders (white arrows). The magnitude images (A-D) are displayed with the same window and center.

3.3.3. Threshold of the relative rT1E

Results from all the subjects are shown in Figure 3.6. Panel A summarizes the relative rT1E of all encoding dimensions and subjects. Overall, the relative rT1E converged similarly among different subjects and decreased to a value close to 1.0. These results demonstrated that the relative rT1E of diastolic frames decreased to close to that

of early systolic frames. Panel B shows that the apparent SNR (normalized to the SNR at time = 30 heartbeats) improved correspondingly. Specifically, without translation correction or phase correction, the apparent SNR improved from 30% to 60% after 20 heartbeats (pink plot). Application of phase error correction reduced signal cancellation and improved the apparent SNR from 60% to 85% after 20 heartbeats (green plot). Then translation correction further improved image quality marginally (blue plot). These results demonstrated that a threshold on the relative rT1E can be applied to prospectively ensure matched phase-cycling pairs and ste-iNAV based compensation for both intra-heartbeat and inter-heartbeat motion is critical for reconstruction of free-breathing cine DENSE images. Based on these results, a value of 1.1 was chosen for the relative rT1E and it should take 20 heartbeats on average for the acquisition of an encoding dimension to converge to such a threshold.

3.3.4. Threshold of rT1E decrease percentage

Figure 3.6C, D show that most of the rT1E changes happened after only one iteration (blue points). The existing relative rT1E and rT1E reduction in this group varies over a wide range. As the time cost increases, the relative rT1E is lower (below 1.2 for time cost >= 3 iterations), and the decrease in rT1E is also smaller (below 5% for time cost >= 3 iterations). These results suggest that the longer it takes for an update in rT1E to occur, the less benefit there is. Based on these results, criterion (2) is reached when the rT1E decrease less than 1% over 3 iterations (i.e. 6 heartbeats).

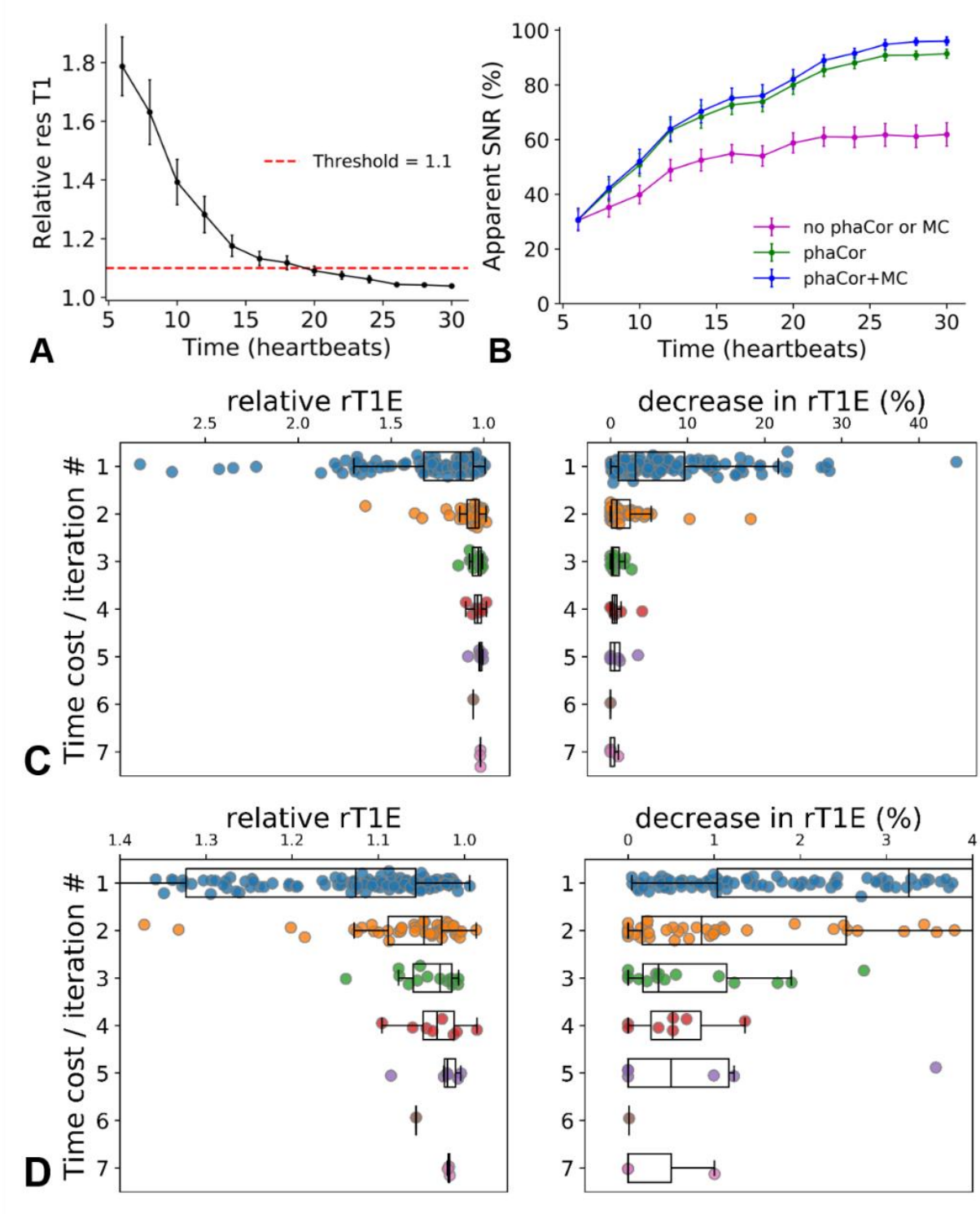

Figure 3.6. Summary of rT1E and image quality in all subjects during the adaptive acquisition with a fixed imaging duration. (A) The relative rT1E converged to a value close to 1.0. (B) The image quality (apparent SNR, normalized to that at time = 30 heartbeats) increased. Compared to the reconstruction without phase error or translation correction (pink curve),

phase error correction significantly improved image apparent SNR (green curve). Translation correction further improved the apparent SNR (blue curve). A threshold value of 1.1 (red dashed line) was chosen for rT1E based on these results. (C-D) The relative rT1E at iterations when the rT1E were updated (left) and the corresponding decreases in rT1E (right). Panel D is a zoom-in of panel C at low rT1E and rT1E decrease ranges. These results included the acquisition processes of all subjects and all encoding dimensions and the data are grouped based on the duration it takes for the rT1E to decrease (y-axis). These results demonstrated that most of the times, it took one or two iterations for the rT1E to decrease (blue and orange data points). The longer it takes to update the rT1E, the lower is the current rT1E and the rT1E decrease.

3.3.5. Phase error correction

Figure 3.7 shows the phase error correction values and the corresponding SNR increases in all subjects. Overall, the phase correction increased the image apparent SNR. For 77% of the images, the average phase correction value was less than 2 radians and the averaged SNR increase was 33% (Figure 3.7A, circled region). For 23% of the images, the phase correction value was larger than 2 radians and in a wide range.

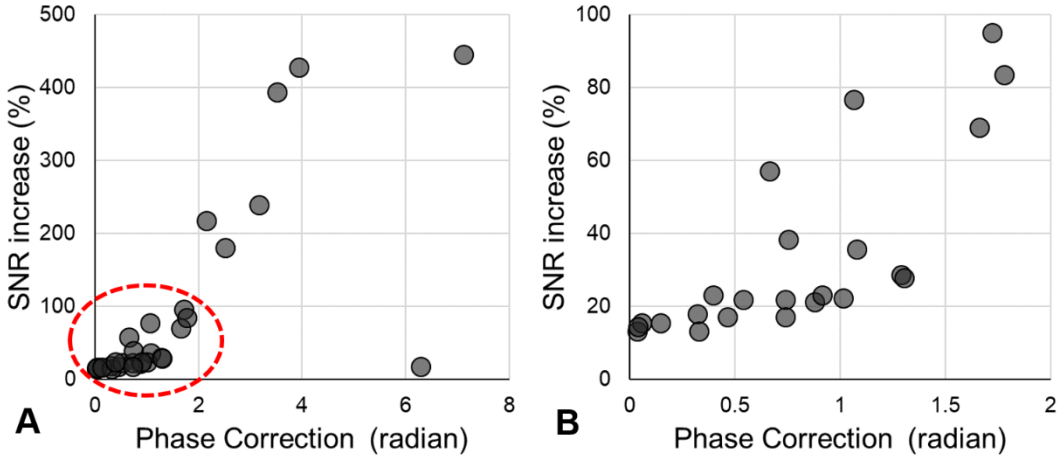

Figure 3.7. The average phase correction and apparent SNR increase. Data were estimated from all encoding dimensions and all subjects at a diastolic frame (trigger time = 600 ms). N = 30. (A) Overall, 77% of the data had phase error correction less than 2 radians and the SNR increase was 33% on average with a range of 0~100% for these data (circled region). The remaining 23% of the data has phase correction values larger than 2 radians and a wide range of SNR increases from the compensation. (B) Zoom in of the circled region in panel A.

3.4 Discussion

In this chapter, a self-navigated free-breathing cine DENSE method was presented. The method uses an adaptive algorithm to reduce the residual energy of the T_1-relaxation echo during the acquisition to compensate for striping artifacts and compensates for both the inter-heartbeat motion induced blurriness and the intra-heartbeat motion induced signal cancellation during reconstruction. Three stopping criteria were designed in the adaptive imaging algorithm to ensure image quality and efficiency. Experiments in healthy subjects were performed to demonstrate the algorithm and determine the values of the stopping criteria.

3.4.1. Adaptive acquisition

At each iteration, the algorithm acquires another instance of spiral interleaves for both phase-cycling dimensions. The new instances can pair with each of the previously acquired instances to form phase-cycling pairs, as shown in Figure 3.8. With the new data being the N^{th} repetition of this segment, the number of new phase-cycling pairs is $2N - 1$. Therefore, the online reconstruction environment needs to store all the old phase-cycled data and calculate the rT1E for all the new phase-cycling pairs. With the protocol in this study, the calculation time of the feedback is tolerable (less than 100 ms). However, the computation power needed can be demanding for the system and limit protocol parameters such as the number of interleaves.

The three stopping criteria are important to ensure both image quality and efficiency. Enforcing the rT1E to below the threshold can guarantee sufficient suppression of the T1-relaxation echo. The imaging time limit and rT1E decrease rate criterion ensures that the algorithm can terminate promptly when the data quality improves marginally over a long time.

Using relative rT1E is critical for the algorithm to apply the same rT1E threshold among subjects and scans. As shown in Figure 3.9, the absolute rT1E at a late diastolic frame converged similarly among subjects but to different values. The absolute rT1E is not applicable to apply a threshold to ensure good image quality in all subjects.

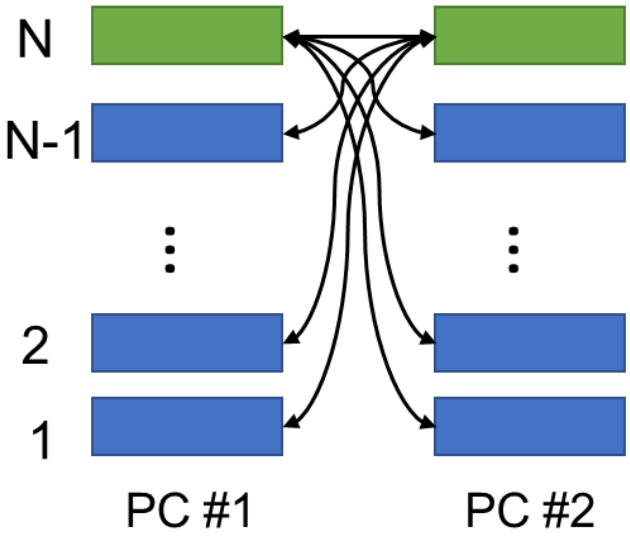

Figure 3.8. Illustration of new phase-cycling pairs at each iteration. At a particular iteration, the acquisition collects one instance of each phase-cycling dimension (PC#1 and PC#2) for the target segment. The data is labeled as the N^{th} repetition of this segment. The new data (green boxes) are paired with all the previously acquired instances (blue boxes) of both phase-cycling dimensions. Therefore, there are $2N-1$ new phase-cycling pairs. The total number of phase-cycling pairs is N^2.

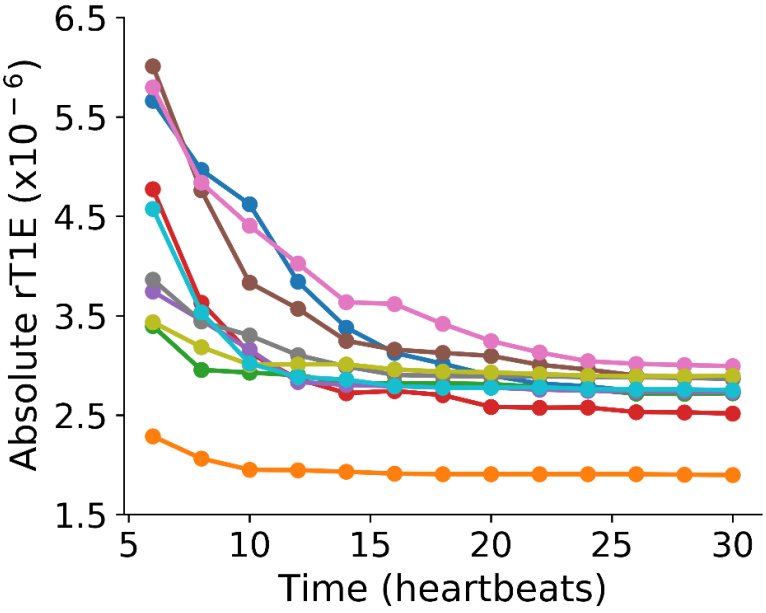

Figure 3.9. Absolute rT1E during the adaptive acquisitions of all subjects. The absolute rT1E converged but to different values.

3.4.2. Phase error correction

The phase errors induced by intra-heartbeat motion and related artifacts are similar to those in diffusion weighted imaging (DWI). However, the compensation methods that have been introduced to DWI cannot be directly applied to cine DENSE. In DWI, the image magnitudes contain the desired diffusion information. The correction for phase error in DWI aims to restore the magnitudes reduced by phase errors. The phase variations among different k-space segments are typically estimated and removed [14]. However, cine DENSE is a phase-contrast method with local tissue displacement encoded in the phase of the stimulated-echoes. Therefore, the correction should aim to reduce the signal cancelation without losing displacement-encoded phase information. In this study, the signal cancellation artifacts were compensated with a correction for the global phase differences among k-space segments without changing the spatial variations of phase from the myocardial displacement. Specifically, the correction value was determined so that it maximized the image energy (Figure 3.3).

Reconstruction of the same free-breathing datasets with different motion compensations demonstrated that both reducing the rT1E and phase correction were essential for the reconstruction. (Figure 3.6B) The global phase correction improved image quality significantly. Meanwhile, the increase of SNR with phase correction was greater when the T1-relaxation echo was better suppressed (before 20 heartbeats vs. after 20 heartbeats). Similarly, the translation correction improved image quality only when the rT1E was low. These results are likely because when the rT1E is high, the residual T_1-echo signal is the main artifact source and hinders the quality of ste-iNAVs, which leads to less improvement from phase correction or translation correction. It is therefore vital to suppress the residual T_1-relaxation signal before compensating for blurriness and signal cancellation.

A limitation of the current phase error correction is that it does not completely remove the intra-heartbeat motion in the final cine DENSE images. The correction can only compensate for the differences in intra-heartbeat motion induced phase among k-space segments. In addition, the correction only included translations while the intra-heartbeat motion can have other components [13].

An estimation of the intra-heartbeat motion or a prior of motion-free reference data would be necessary to correct the phase error accurately. One possible solution is to combine breath-hold and free-breathing acquisitions, where one segment of each encoding is acquired during a short breath-hold at the beginning of the scan to obtain reference segments and the rest of the scan is performed with the adaptive acquisition during free-breathing. With such strategies, the phase errors in the free-breathing data may be compensated accurately. Another improvement of the algorithm can be to jointly estimate the correction values of all the k-space segments.

3.4.3. Conclusion

In conclusion, an adapted acquisition algorithm was developed for self-navigated free-breathing cine DENSE imaging. The algorithm prospectively minimized the residual T_1-echo signal and reduced striping artifacts. Experiments in healthy subjects proved the concepts of the algorithm and provided the feasibility of applying a stopping criterion on the normalized residual T_1-echo to terminate the data acquisition promptly. A third type of artifact, namely signal cancellation due to intra-heartbeat motion, was investigated. A simple compensation method was developed and demonstrated effective in improving image quality. Validation of these methods in vivo in patients is necessary. Further development should investigate accurate estimation and compensation of the intra-heartbeat motion induced phase errors.

3.5 References

1. Kim, D., et al., *Myocardial tissue tracking with two-dimensional cine displacement-encoded MR imaging: development and initial evaluation.* Radiology, 2004. **230**(3): p. 862-871.
2. Auger, D.A., et al., *Imaging left - ventricular mechanical activation in heart failure patients using cine DENSE MRI: Validation and implications for cardiac resynchronization therapy.* Journal of Magnetic Resonance Imaging, 2017.
3. Mangion, K., et al., *Comparative prognostic value of myocardial strain derived from DENSE CMR: the British Heart Foundation MR-MI study.* The Lancet, 2017. **389**: p. S66.
4. Jing, L., et al., *Impaired right ventricular contractile function in childhood obesity and its association with right and left ventricular changes: a cine DENSE cardiac magnetic resonance study.* Journal of Cardiovascular Magnetic Resonance, 2017. **19**(1): p. 49.
5. Kihlberg, J., et al., *Clinical experience of strain imaging using DENSE for detecting infarcted cardiac segments.* Journal of Cardiovascular Magnetic Resonance, 2015. **17**(1): p. 50.
6. Ehman, R.L. and J.P. Felmlee, *Adaptive technique for high-definition MR imaging of moving structures.* Radiology, 1989. **173**(1): p. 255-263.
7. Zhong, X., et al., *Imaging three - dimensional myocardial mechanics using navigator - gated volumetric spiral cine DENSE MRI.* Magnetic resonance in medicine, 2010. **64**(4): p. 1089-1097.
8. Hamlet, S.M., et al., *Optimal configuration of respiratory navigator gating for the quantification of left ventricular strain using spiral cine displacement encoding with stimulated echoes (DENSE) MRI.* Journal of Magnetic Resonance Imaging, 2017. **45**(3): p. 786-794.
9. Sachs, T.S., et al., *The real-time interactive 3-D-DVA for robust coronary MRA.* IEEE transactions on medical imaging, 2000. **19**(2): p. 73-79.
10. Nehrke, K., et al., *Free-breathing cardiac MR imaging: study of implications of respiratory motion—initial results.* Radiology, 2001. **220**(3): p. 810-815.
11. Cai, X. and F.H. Epstein, *Free - breathing cine DENSE MRI using phase cycling with matchmaking and stimulated - echo image - based navigators.* Magnetic resonance in medicine, 2018.
12. Gilson, W.D., et al., *Complementary displacement - encoded MRI for contrast - enhanced infarct detection and quantification of myocardial function in mice.* Magnetic Resonance in

Medicine: An Official Journal of the International Society for Magnetic Resonance in Medicine, 2004. **51**(4): p. 744-752.

13. Anderson, A.W. and J.C. Gore, *Analysis and correction of motion artifacts in diffusion weighted imaging.* Magnetic resonance in medicine, 1994. **32**(3): p. 379-387.
14. Liu, C., et al., *Self - navigated interleaved spiral (SNAILS): application to high - resolution diffusion tensor imaging.* Magnetic Resonance in Medicine: An Official Journal of the International Society for Magnetic Resonance in Medicine, 2004. **52**(6): p. 1388-1396.
15. Johnson, C.L., et al., *Magnetic resonance elastography of the brain using multishot spiral readouts with self - navigated motion correction.* Magnetic resonance in medicine, 2013. **70**(2): p. 404-412.
16. Mills, P., et al., *Localized imaging using stimulated echoes.* Magnetic resonance in medicine, 1987. **5**(4): p. 384-389.
17. Irarrazabal, P., et al., *Inhomogeneity correction using an estimated linear field map.* Magnetic resonance in medicine, 1996. **35**(2): p. 278-282.
18. Noll, D.C., et al., *A homogeneity correction method for magnetic resonance imaging with time-varying gradients.* IEEE transactions on medical imaging, 1991. **10**(4): p. 629-637.

Chapter 4
Myocardial strain imaging with self-navigated free-breathing cine DESNE

4.1. Introduction

Cine displacement-encoded stimulated echoes (DENSE) MRI [1] is a quantitative myocardial strain imaging technique that is accurate, reproducible and amenable to fast analysis. The conventional protocol requires breath-holding, which can be difficult for many patients [2]. A free-breathing method is desirable for strain imaging in patients.

There are three major types of artifacts in free-breathing cine DENSE: striping artifacts, signal cancellation artifacts and blurring. While blurring is a common type of motion artifact in MRI, striping and signal cancelation artifacts are distinctive aspects of free-breathing cine DENSE. The source of striping artifacts is insufficient suppression of the T_1-relaxation echo [3-5]. Besides the motion that happens from heartbeat to heartbeat (inter-heartbeat motion), breathing motion also occurs within each heartbeat (intra-heartbeat motion). The intra-heartbeat motion causes various phase errors for each segment and subsequent signal cancellation artifacts when the k-space segments are combined to reconstruct images [6].

To overcome these artifacts, new self-navigated methods were developed for artifacts reduction and motion correction in free-breathing cine DENSE. The striping artifacts were compensated first by matching the phase-cycling pairs, i.e. minimizing the energy of the residual T_1-echo energy (rT1E). After subtraction of the matched phase-cycling pairs, the blurring artifacts were corrected by motion estimation with stimulated-echo only image-based navigators (ste-iNAVs) and k-space correction. The signal cancellation artifacts were reduced with segment-to-segment phase correction. An adaptive imaging algorithm for prospectively diminishing the rT1E in real-time was also developed. With this algorithm, the rT1E values are calculated for each segment in real-

time and the segment with the highest rT1E is repeated until the rT1E values of all post-subtraction data are below a prescribed threshold.

The study in the present chapter aims to apply these self-navigated (self-NAV) methods to image myocardial strain in both healthy subjects and patients with heart disease and compare the self-NAV method with the conventional dNAV method.

4.2. Methods

4.2.1. Self-navigated cine DENSE

4.2.1.1. Acquisition with adaptive imaging algorithm

The adaptive imaging algorithm introduced in Chapter 3 with all three stopping criteria is used for data acquisition. The algorithm starts with acquiring a complete k-space and calculating the rT1E values. At each iteration, the algorithm repeats the segment with the highest rT1E until any of the included stopping criteria is satisfied. Specifically, the stopping criteria are (1) the relative rT1E is below 1.1, (2) the change of rT1E over 3 iterations is below 1%, and (3) imaging time reaches the maximal limit of 30 heartbeats. The algorithm acquires data with this process for each encoding separately.

The adaptive imaging algorithm is implemented with a cine 2D spiral cine DENSE sequence. The displacement encoding module utilizes localized generation of the stimulated-echoes [7] and the data acquisition employs a segmented spiral trajectory with uniform rotation through cardiac frames.

4.2.1.2. Reconstruction with match-making framework

Image reconstruction is performed with the match-making framework described in Chapter 2. For each encoding dimension, subtraction of the matched phase-cycling pairs is first performed to cancel the T_1-relaxation echoes. Afterward, ste-iNAVs are reconstructed from the post-subtraction data and each iNAV frame is reconstructed from the data of three consecutive cardiac frames. Cross-correlation is performed to estimate the in-plane translations with the ste-iNAVs. The motion estimation is performed for each iNAV frame separately. To reduce the blurring artifacts, k-space linear phase correction is applied to compensate for the in-plane translations [8, 9] and the ste-iNAVs are

reconstructed again with the translation corrected data. Afterward, global phase error estimation and correction is performed to reduce the signal cancellation artifacts. The reference segment for phase error estimation is described in detail in the next subsection. After phase error correction, the cine DENSE images are reconstructed with non-uniform fast Fourier Transform (NUFFT) [10]. After the images of all encoding dimensions are reconstructed, the combined magnitude images and displacement-encoded phase images are extracted [11].

4.2.1.3. Joint reference segment selection for phase correction

To reduce the bulk phase error in the final displacement-encoded phase images, the reference segments of all encoding dimensions are jointly determined using the ste-iNAVs. The aim is to determine a combination of reference segments, one per encoding dimension, that minimize the overall displacement phase at late-diastole. Given that the phase due to tissue displacement increases during systole and rewinds during diastole, the bulk phase errors due to the intra-heartbeat motion can be minimized by selecting reference segments that minimize the averaged displacement phase at late-diastole. For each combination of ste-iNAVs, the overall displacement phase φ is defined as,

$$\varphi(i,j,k) = angle[\textstyle\sum_r D\left(I_{1,i}, I_{2,j}, I_{3,k}\right)] \quad (4.1)$$

where $I_{1,i}$, $I_{2,j}$, $I_{3,k}$ indicates the late-diastolic ste-iNAVs of the i^{th}, j^{th}, k^{th} segment of the first, second and third encoding dimensions respectively. D indicates the operation to extract displacement phase images. r is the spatial locations in the 2D imaging plane. The magnitudes of the displacement phase images are calculated as the average of the input ste-iNAVs, $I_{1,i}$, $I_{2,j}$, and $I_{3,k}$. The reference segments of all encoding dimensions are determined as the combination that minimizes φ,

$$\left(S_{ref,1}, S_{ref,2}, S_{ref,3}\right) = \min_{i,j,k} |\varphi(i,j,k)| \quad (4.2)$$

Two sets of reference segments are determined for extraction of the displacement encoded phases images in the x- and y-directions respectively.

4.2.2. dNAV-gated cine DENSE

A 2D spiral cine DENSE sequence that supports the acquisition of dNAV was modified to include localized generation of stimulated-echoes and rotation of trajectory through cardiac frames. The sequence acquires a dNAV right after the DENSE data acquisition during each heartbeat. Therefore, the sequence acquires data for each heartbeat and retrospectively accepts or rejects the present heartbeat based on the dNAV result.

4.2.3. Imaging healthy subjects

To evaluate the self-NAV method and compare its performance with the conventional dNAV method, a total number of 10 healthy subjects (5 females, 26 ± 3 years old) were scanned on a 3T scanner (Magnetom Prisma, Siemens Healthineers, Erlangen, Germany) with informed consent in accordance with protocols approved by the institutional review board. Cine DENSE datasets were acquired on a mid-ventricular slice once with breath-hold, twice with the self-NAV method and twice with dNAV. The imaging parameters included: slice thickness = 8 mm, FOV = 320 x 320 mm^2, width of the localized stimulated-echo region = 90 ~ 110 mm, 6 spiral interleaves per image, 2 interleaves per segment, uniform rotation of trajectory by 60 degrees per frame, TR = 15 ms, temporal resolution = 30 ms, TE = 1.08 ms, spiral readout length of 5.5 ms, matrix size of 128 x 128, balanced 3-point displacement encoding with encoding frequency = 0.05 cyc/mm. Ramped flip angles with the last flip angle = 15 degrees were employed. Multiple cardiac frames were imaged with prospective ECG triggering covering approximately 80% of the RR interval. Fat suppression was applied immediately after ECG triggering and before the DENSE displacement pulses.

For breath-hold acquisition, imaging was performed at end-expiration. For the adaptive free-breathing, imaging was performed with criteria (1) and (3). The stopping criterion (2) was applied retrospectively during reconstruction. For the dNAV-gating method, diaphragm navigator was acquired in late diastole and right after cine DENSE data acquisition of each heartbeat. The acceptance window was set at end-expiration with a width of ± 2 mm.

4.2.4. Imaging patients with heart disease

The self-navigation method was also evaluated in patients with heart disease. A total number of 13 patients (7 females, 57 ± 16 years old) were scanned on 3T systems (3 on Magnetom Skyra and 10 on Magnetom Prisma, Siemens Healthineers, Erlangen, Germany). Exclusion criteria for patient recruiting included inability to breath-hold, ages(pediatrics) and implantable devices, such as pacemakers, ICD or CRT. Cine DENSE datasets were acquired once with breath-holding, twice with self-NAV and twice with dNAV, as add-on acquisitions to clinical CMR exams. For breath-hold acquisitions, balanced 2-point encoding was used. Therefore, each slice with two breath-holds and 14-heartbeats long per breath-hold. Imaging was performed at end-inspiration to be consistent with the rest of the CMR exams. For free-breathing acquisitions, balanced 3-points was used for displacement encoding. For the adaptive imaging algorithm, all three stopping criteria were included. For dNAV acquisitions, the navigator acceptance window was ± 2 mm at end-expiration. All other imaging parameters were the same as those in healthy subject imaging.

4.2.5. Image reconstruction and analysis

Each dataset acquired with the self-NAV method was reconstructed in MATLAB to apply translation and phase correction. Displacement phase images and combined magnitude images were extracted afterward. Each self-navigated dataset in healthy subjects was also reconstructed with criterion (2) retrospectively applied. The relative rT1E was calculated for each cine DENSE dataset. The breath-hold and dNAV acquisitions were reconstructed with NUFFT.

The apparent SNR values of magnitude images were calculated based on the combined magnitude images with a myocardium region of interest and a background region. Correction for Rician distribution was applied during SNR quantification [12, 13]. Segmental circumferential strain values were computed with the displacement phase images for 6 segments of the left ventricle using the standardized AHA segmentation model [14-16]. Both the relative rT1E and the apparent SNR were averaged through cardiac frames and compared among breath-hold, dNAV and self-NAV. Between the two free-breathing methods, imaging time was compared with t-test and agreement of free-

breathing strain with breath-hold strain and reproducibility of breathing strain were analyzed using Bland-Altman plots. All statistical tests are performed using SigmaPlot (Systat Software Inc).

The reference segment selection method in the self-NAV method was assessed using the datasets acquired in healthy subjects. With the breath-hold acquisition, the ste-iNAVs were reconstructed from the post-subtraction data for the same late-diastole iNAV frame. The displacement encoded phase image was extracted from these ste-iNAVs. For each combination of ste-iNAVs of the self-NAV acquisition, the displacement encoded phase image was also extracted. The overall phase was calculated with equation 4.1 and the overall phase error relative to the breath-hold displacement encoded phase image was also estimated using the method in Figure 3.3. The overall displacement phase was then correlated with the phase error relative to the breath-hold acquisition.

4.3. Results

4.3.1. Imaging healthy subjects

Figure 4.1 demonstrates the adaptive acquisition process with the prospectively applied stopping criteria. Panel A shows the relative rT1E of the post-subtraction k-space data at each iteration during the acquisition. The rT1E values were high at the beginning of the process, particularly for segment #1. The algorithm determined segment #1 as the target segment and repeated acquisition for this segment. After this iteration, the rT1E of segment #1 decreased and the algorithm repeated acquisition for the new target segment, segment #2. Such processes continued until all the segments had a relative rT1E below the threshold 1.1 (red dashed line). The imaging time was 18 heartbeats. Panel B shows reconstructed images correspond to 4 different time points during the acquisition. The images at the beginning of the acquisition (t_1) had severe striping artifacts from the strong residual T_1-echo (arrows). The images after 1 iteration (t_2) had improved image quality compared to those at t_1. The image quality further improved as the algorithm progressed (t_3) and the final images were free of striping artifacts (t_4).

Figure 4.2 compares cine DENSE images and circumferential strains in a healthy subject acquired with breath-hold, self-NAV and dNAV. The images and circumferential

strain curves with breath-hold were high quality. The images and strain curves with the self-navigation method resemble the quality of those from breath-hold acquisition. However, the images acquired with dNAV method had severe artifacts in the magnitude (yellow arrows), errors in the phase images (red arrows) and the strain curves.

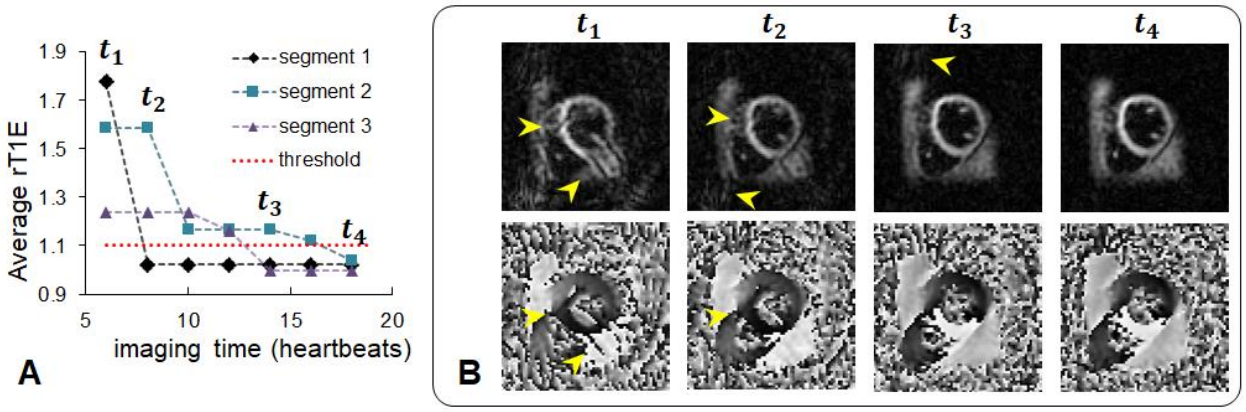

Figure 4.1. Demonstration of the adaptive acquisition method. Panel (A) shows the relative rT1E values as they update during an 18-heartbeat acquisition and panel (B) shows images corresponding to 4 time points during the acquisition. After the initial free-breathing acquisition of all segments (t_1), the overall rT1E was high and the image had strong artifacts (panel B-t_1, arrows). Next, the acquisition of segment 1 (with the highest rT1E) was repeated. The rT1E of segment 1 decreased and the image quality improved (t_2). As the algorithm iterated, the rT1E decreased and the image quality improved further (t_3, t_4). The acquisition stopped at t_4 when all the rT1E were below the predefined threshold.

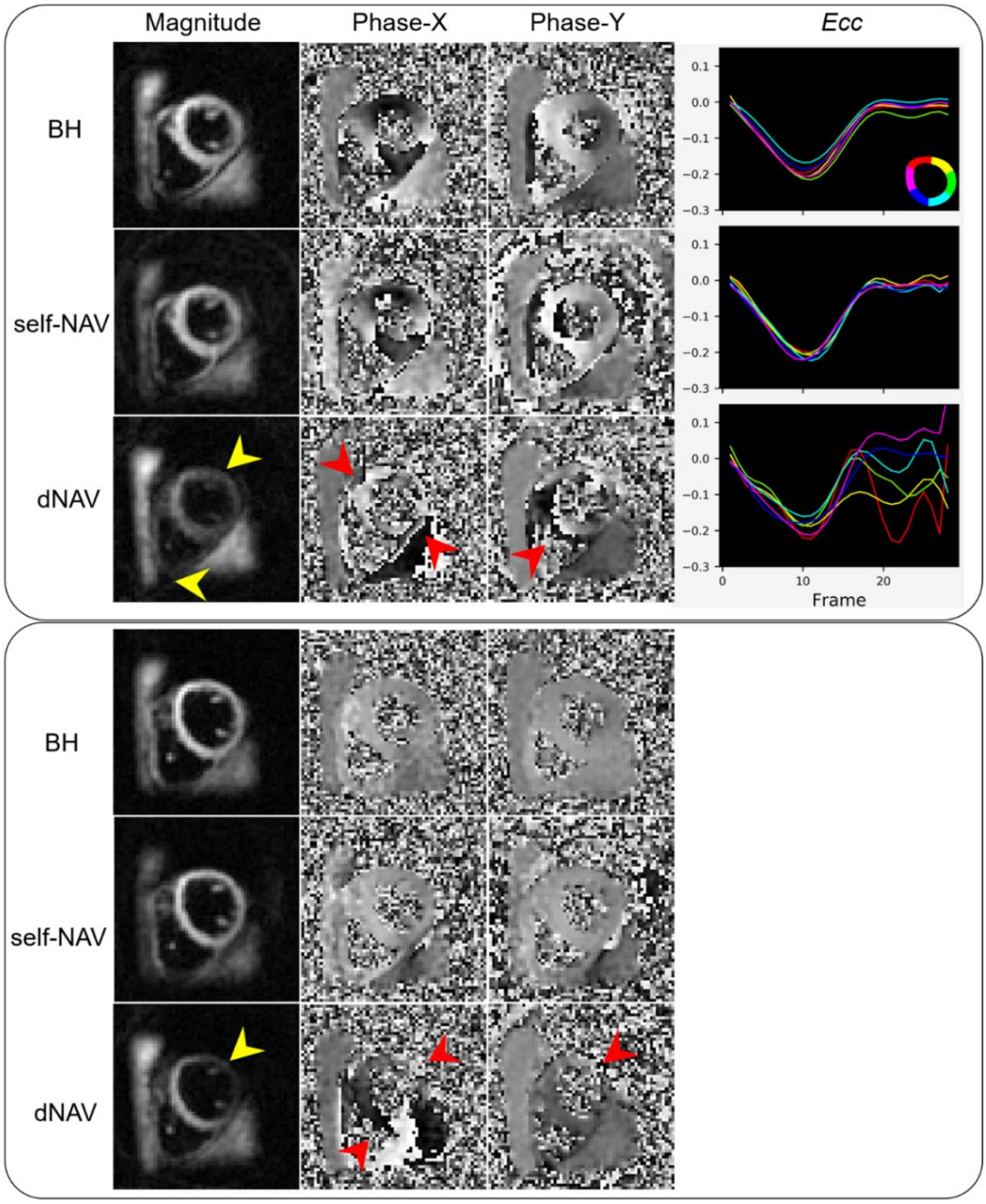

Figure 4.2. Example cine DENSE images and circumferential strain from a healthy volunteer acquired with breath-hold (BH), self-NAV and dNAV methods. An end-systolic frame (top box) and a late-diastolic frame (bottom box) are shown. In this subject, the images acquired with dNAV had artifacts and reduced SNR in the magnitudes (yellow arrows) and errors in the myocardium displacement phase (red arrows). The images acquired with self-NAV had high-quality magnitude and phase images. The segmental strain curves by dNAV had severe errors while the strain curves by the self-NAV method well-resembled those by BH.

Figure 4.3 summarizes the comparison of the self-NAV method with dNAV in healthy subjects. The rT1E of breath-hold acquisitions was lower than free-breathing acquisitions and the rT1E of dNAV was higher than that of self-NAV (panel A). The image SNR of breath-hold acquisitions was higher than that of free-breathing acquisitions (panel B). The imaging time of self-NAV method without criterion (2) was longer than dNAV by 7 heartbeats per encoding (panel C). However, the imaging time of dNAV did not include the time for scout scans to set up navigators. The Bland-Altman plots showed that the circumferential strain by self-NAV, both without and with criterion (2) was in better agreement with that by breath-hold (panels D, E vs. F) and was more reproducible than dNAV (panels G, H vs. I). These results demonstrated that the proposed adaptive method produced better suppression of the T_1-relaxation echo and strain quantification than dNAV with similar imaging time.

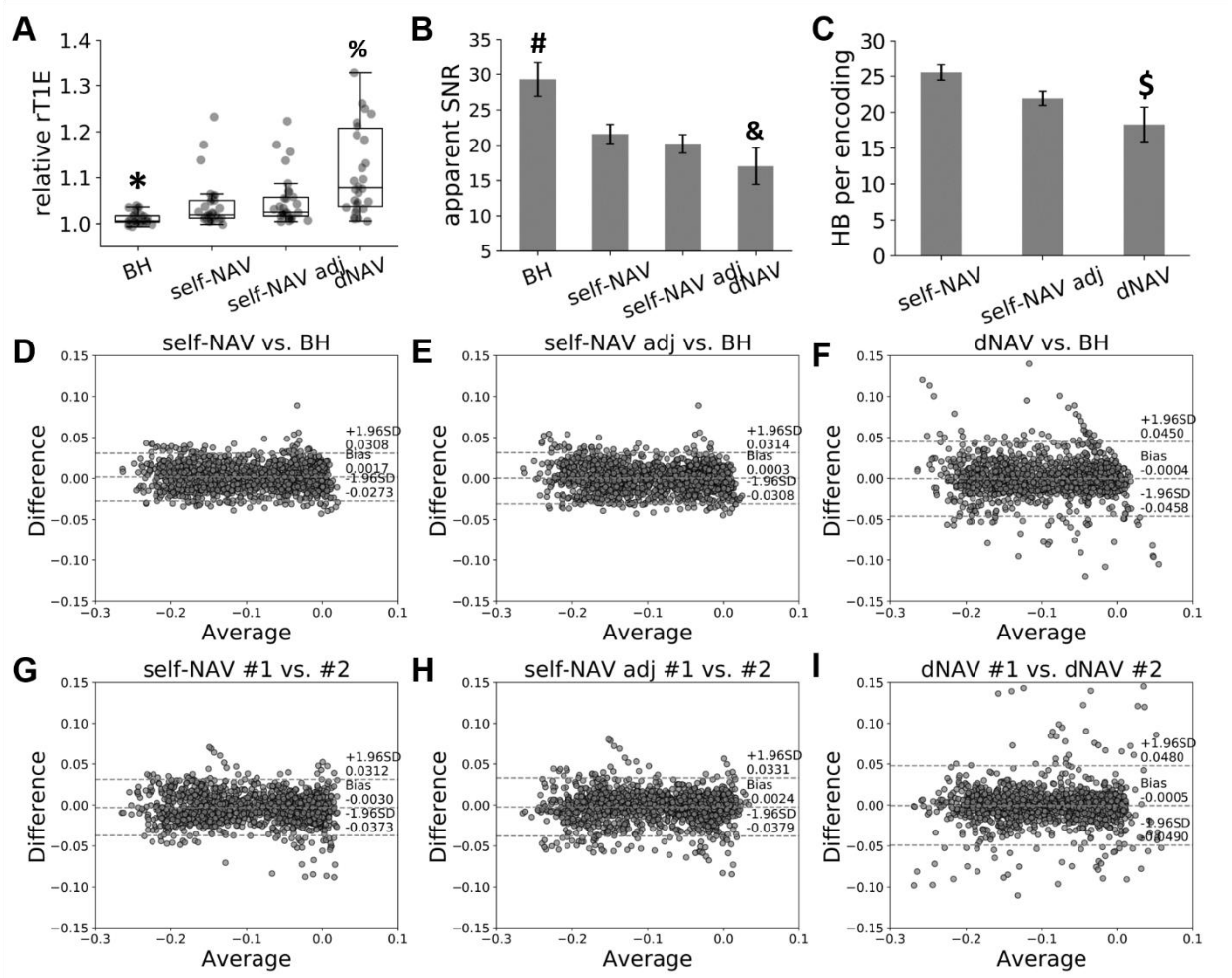

Figure 4.3. Comparison of rT1E, imaging time and image quality among BH, self-NAV and dNAV in healthy volunteers. (A) Relative rT1E. BH overall achieved a lower relative rT1E than free-breathing acquisitions. The adaptive method, without or with criterion (3), achieved lower rT1E than dNAV. (B) Apparent SNR. BH achieved the highest SNR. The SNR of the dNAV method trended to be lower than self-NAV. (C) The imaging time of dNAV was less than self-NAV without criterion (2) by 7 heartbeats per encoding dimension. (D - F) The Ecc by self-NAV was in better agreement with that by BH than dNAV. (G - I) The Ecc by the self-navigation method was more reproducible than that by dNAV. (self-NAV: self-navigated free-breathing method without criterion (2); self-NAV adj: self-navigated free-breathing method with criterion (2) retrospectively applied; *P < 0.05, vs. self-NAV, self-NAV adj, and dNAV, %P < 0.05 vs. BH, self-NAV, and self-NAV adj, one-way repeated measure ANOVA on ranks; #P < 0.05, vs. self-NAV, self-NAV adj, and dNAV, &P = 0.187 vs. self-NAV, one-way repeated measure ANOVA; $P < 0.05 vs. self-NAV, one-way repeated measure ANOVA on ranks)

4.3.2. Imaging patients

Figures 4.4-4.5 show cine DENSE images and segmental circumferential strains from two patients comparing the free-breathing acquisitions with the breath-hold acquisition. In the example of Figure 4.4, the breath-hold images have little striping artifacts but are blurry. The free-breathing images with dNAV had residual artifacts (yellow arrows) and phase errors in the images (red arrows). The images by self-NAV have less blurriness and residual T_1-echo signal than dNAV. The self-NAV and dNAV produced similar strain curves. In the example of Figure 4.5, the images with breath-hold and self-NAV are high quality. The images by dNAV have artifacts (yellow arrows) and phase errors (red arrows). The segmental strain curves are similar among the acquisitions and all show reduced myocardial strain in the septum sectors.

Figure 4.6 summarizes the results in patients. The rT1E of the dNAV was higher than both breath-hold and self-NAV (panel A) indicating less sufficient suppression of the T_1-relaxation echo by dNAV. There was no significant different in the image apparent SNR between the acquisitions (panel B). The imaging time of self-NAV was longer than dNAV by 4 heartbeats per encoding dimension (panel C). The agreement of free-breathing strain with breath-hold strain was similar between self-NAV and dNAV

(panels D, E). The reproducibility of free-breathing strain by dNAV was better than self-NAV (panels F, G).

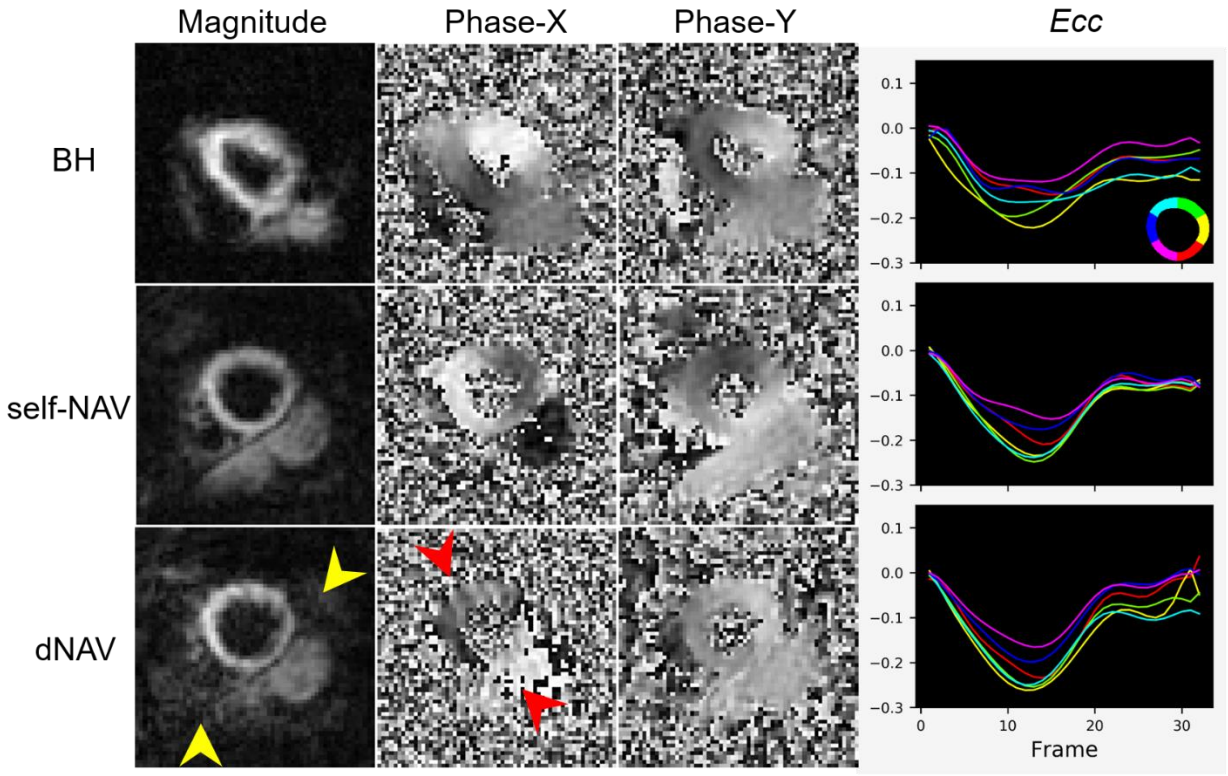

Figure 4.4. Example cine DENSE images and circumferential strains from a patient. The images are at a diastolic frame (trigger time = 630 ms). The BH images were blurry. Self-NAV produced the best quality images and segmental strain. With dNAV, the images had more striping and blurring artifacts (yellow arrows) and phase errors (red arrows). The BH was performed at end-inspiration and therefore the heart position was different from those of free-breathing acquisitions. (BH: breath-hold; self-NAV: self-navigated free-breathing method; dNAV: diaphragm navigator-based gating method).

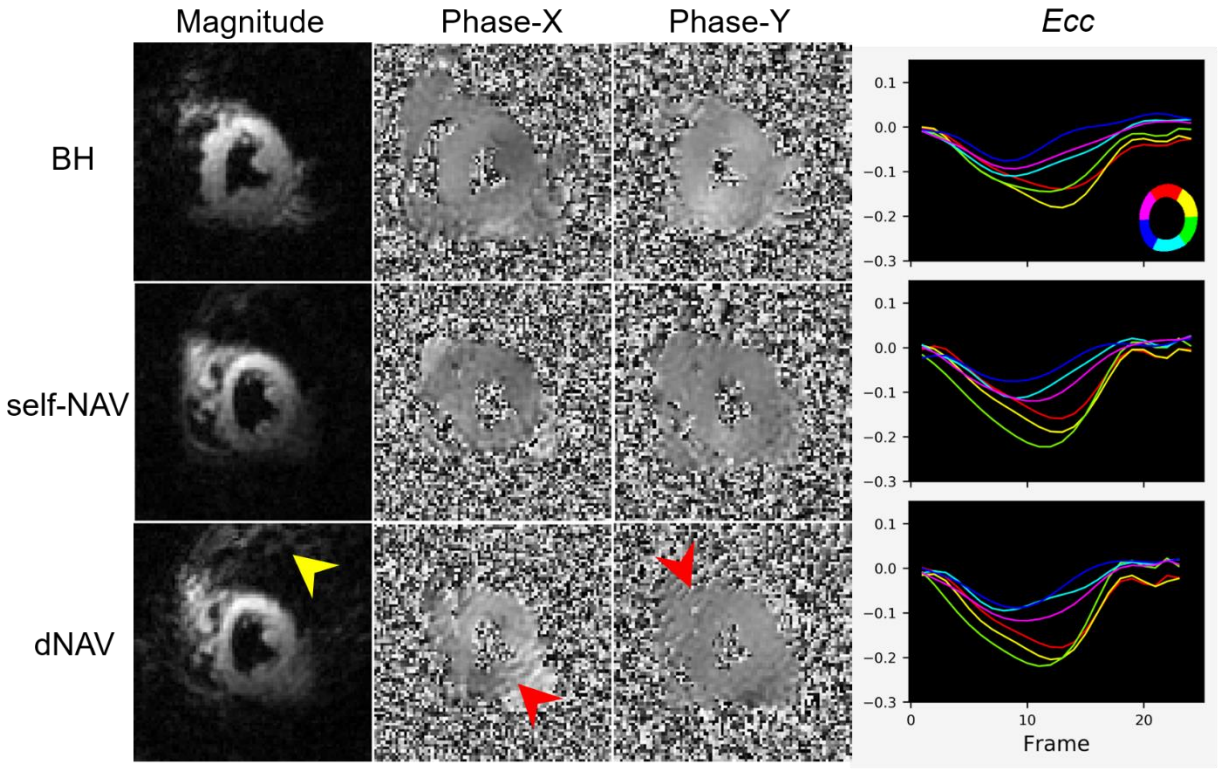

Figure 4.5. Example cine DENSE images and circumferential strains from another patient. The images at a late diastolic frame are shown (trigger time = 690 ms). The BH images are high quality. The images by dNAV had artifacts (yellow arrows) and phase errors (red arrows). The segmental strain curves were similar among the acquisitions and showed dysfunction in the septum sectors. (BH: breath-hold; self-NAV: self-navigated free-breathing method; dNAV: diaphragm navigator-based gating method).

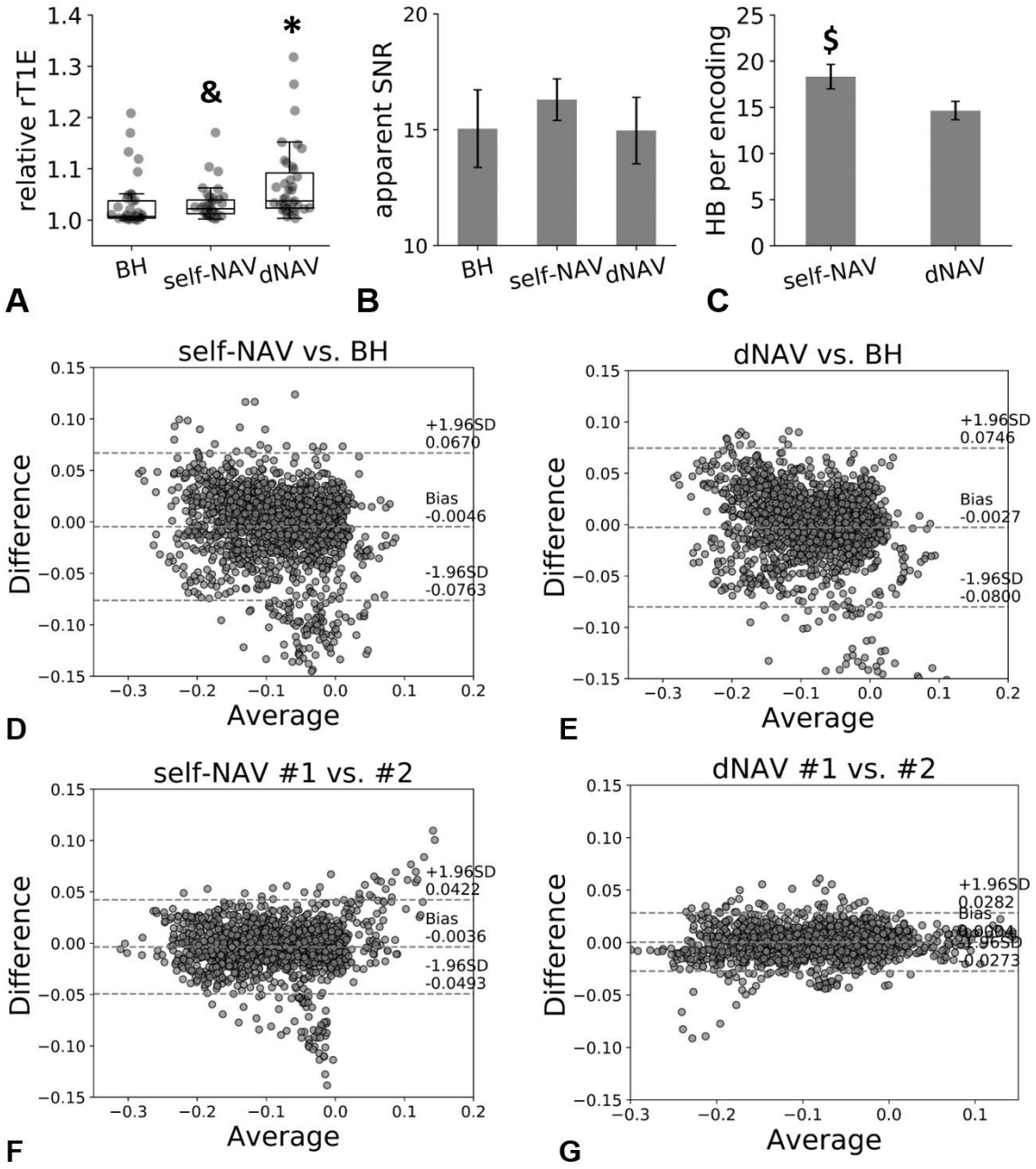

Figure 4.6. Evaluation of the free-breathing method in patients. (A) The relative rT1E. (B) Apparent SNR. (C) Imaging time. (D) Bland-Altman plot of free-breathing strain by self-NAV with breath-hold strain. (E) Bland-Altman plot of free-breathing strain by dNAV with breath-hold strain. (F) Bland-Altman plot of the repeated free-breathing strain by self-NAV. (G) Bland-Altman plot of the repeated free-breathing strain by dNAV. (*P <0.05 vs. BH or self-NAV, &P = 0.061 vs. BH, one-way repeated measure ANOVA on ranks; $P < 0.05, paired t-test) (BH: breath-hold; self-NAV: self-navigated free-breathing method; dNAV: diaphragm navigator-based gating method).

4.3.3. Joint reference segment selection

In a healthy subject, the average phase of free-breathing displacement phase image was highly correlated with the bulk phase error relative to breath-hold (Figure 4.7). The data are estimated using ste-iNAVs of one encoding dimension. Minimizing the average displacement phase at late-diastole identified reference segments that can minimize the phase error with breath-hold in the final free-breathing displacement phase images (C_1).

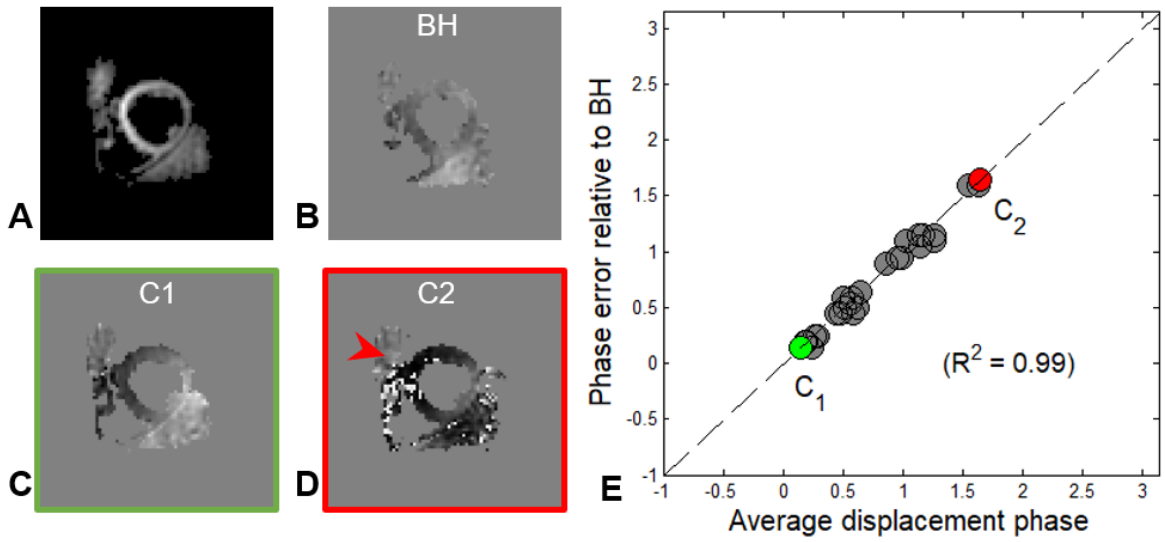

Figure 4.7. Correlation of the averaged displacement phase with the bulk phase error relative to the breath-hold displacement phases in a subject. (A-B) The magnitudes and the phases of the displacement-encoded ste-iNAV acquired with breath-hold (BH) at a late-diastole. The background regions are excluded with a region-of-interest created based on the magnitudes. The displacement phase values in the myocardium are overall trivial. (C-D) The displacement encoded phase images extracted from two combinations of free-breathing ste-iNAVs. For C_1, the overall displacement phase was small and similar to the breath-hold displacement phase in panel B. For C_2, the overall displacement phase is close to $-\pi$ especially in the anterior wall (arrow). (E) In this subject, the averaged displacement phase is highly correlated to the bulk phase error relative to BH with $R^2 = 0.99$. The two combinations in panels C-D are color-coded. Minimizing the averaged displacement phase identifies the reference segments that provide minimized phase error relative to BH (C_1). (BH: breath-hold; the dashed line is the identity line)

Overall, the correlation held up in all healthy subjects with R^2 of 0.61 (Figure 4.8). The reference segment combinations chosen with minimal displacement phase reduced the phase error with breath-hold compared to those consisting of the first segments (green dots vs. pink dots). These results demonstrate the proposed method for reference segment selection can reduce the overall phase errors due to intra-heartbeat motion relative to breath-hold acquisitions in the displacement phase images.

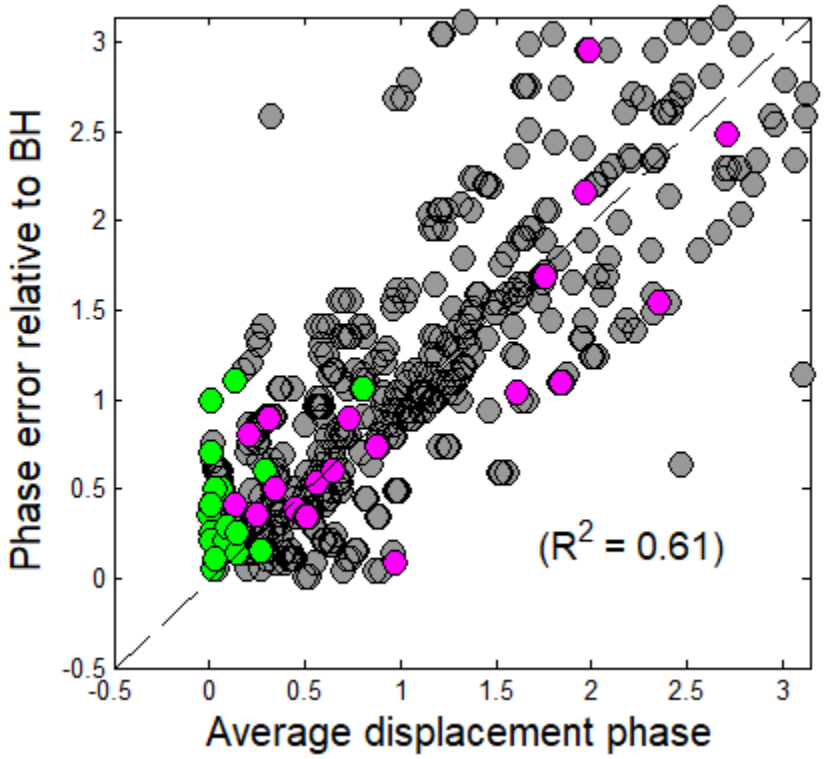

Figure 4.8. Correlation between the averaged displacement phase and the phase error relative to breath-hold data in all healthy subjects. Overall, the phase error relative to BH is correlated with the averaged displacement phase with $R^2 = 0.6\,1$. The free-breathing ste-iNAV combinations identified by minimizing the average displacement phase are shown in green and the ste-iNAV combinations with the first segments are shown in pink. These results demonstrate that minimizing the averaged displacement phase identifies the reference segments that provide reduced phase error relative to breath-hold. (BH: breath-hold; the dashed line is the identity line)

4.4. Discussion

In the studies of this chapter, the self-navigated free-breathing cine DENSE method was evaluated in both healthy subjects and patients with heart disease and compared to the conventional dNAV method.

4.4.1. Comparison with dNAV in healthy subjects

In the healthy subject experiments, the self-NAV method was better than dNAV for myocardial strain imaging with lower rT1E, better agreement of segmental strain with that by breath-hold, and better reproducibility of strain.

The self-NAV method is better than dNAV potentially due to multiple reasons. First, minimizing rT1E is more reliable than minimizing dNAV acceptance window for reducing striping artifacts in free-breathing cine DENSE. The 1D navigator position in dNAV is not sufficient to measure the motion of the heart [17] and the respiration pattern measured as diaphragm positions varies significantly from subject to subject. Therefore, the dNAV method produces variable image quality. On the other hand, reduced rT1E directly reduces striping artifacts and improve image quality regardless of the respiration pattern. In addition, diminishing rT1E can reduce residual T_1-relaxation signal due to factors other than breathing. For instance, cine DENSE uses prospective ECG triggering and RR interval changes during the acquisition can lead to missing triggering (e.g. skipping a heartbeat). Imaging signal during the heartbeats after the skipped ones is higher than other heartbeats because of the longer relaxation time. Such changes can lead to increased residual signal and artifacts even when respiratory positions are similar. The self-NAV method can reject such data while dNAV cannot.

The results of healthy subject experiments also showed improvement in free-breathing strain imaging compared to those of the evaluation of the match-making framework in Chapter 2, Figure 2.9. The agreement of free-breathing strain with breath-hold strain is better while the imaging time is similar. Both the reduced rT1E from the adaptive imaging and the reduced phase errors from the intra-heartbeat motion compensation may have contributed to these improvements.

4.4.2. Comparison with dNAV in patients

In the patient experiments, there was no significant difference in the relative rT1E between breath-hold and self-NAV, while in healthy subjects breath-hold acquisition consistently achieved lower rT1E than free-breathing acquisitions. Again, the breath-hold duration in healthy subject imaging was longer by 6 heartbeats than that in patient imaging. These results are likely because of reduced breath-holding capabilities in patients. Correspondingly, the apparent SNR of breath-hold acquisitions was not higher than the free-breathing acquisitions in patients.

The relative rT1E of self-NAV was lower than dNAV, demonstrating better suppression of the T_1-relaxation echo with self-NAV. However, there was no significant advantage of self-NAV in image quality or strain quantification. The image SNR of self-NAV was not significantly higher than dNAV. The strain by self-NAV was neither in better agreement with breath-hold strain nor more reproducible than dNAV. These results are potentially due to several reasons. First, the sample size is relatively small. The variability of image SNR in patients was larger than in healthy subjects. Second, the residual T_1-echo did not affect the image quality in the myocardium with the imaging field-of-view of 320 mm. Figure 4.9 compares acquisitions in a patient where dNAV had significantly strong residual T_1-eho (arrows) than self-NAV. Yet, the residual T_1-echo signal was mainly outside of the myocardium region and did not lead to significant errors in the strain curves.

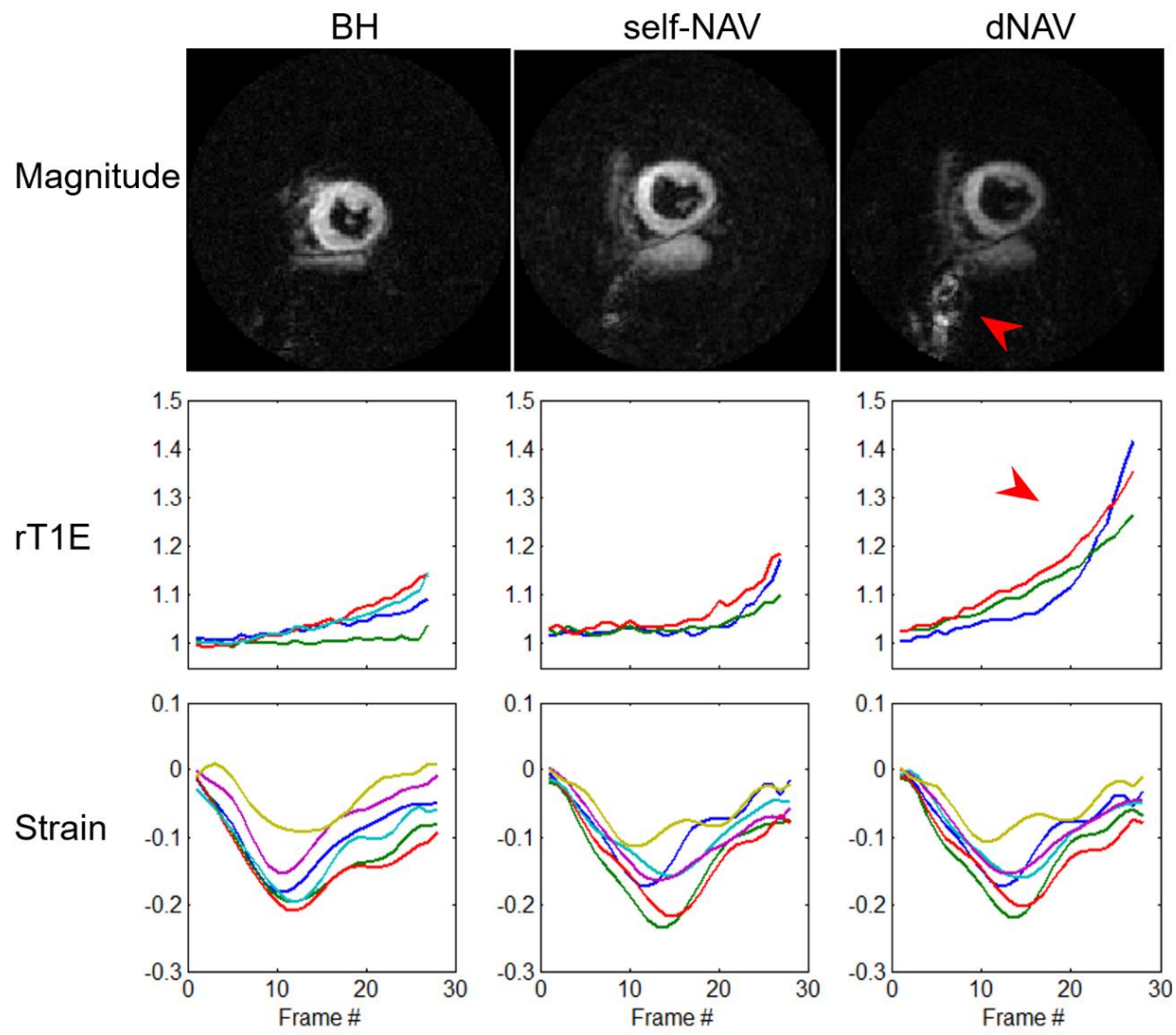

Figure 4.9. Example datasets in a patient. The dNAV method achieved worse suppression of the T_1-echo and had strong residual T_1-echo signal in the images (arrows). However, the residual T_1-echo signal in this case was outside of the myocardium region and did not affect the strain quantification. The strain curves are similar between dNAV and self-NAV.

The overall agreement of free-breathing strain with breath-hold strain in patients was less than that in healthy subjects, which was likely due to the differences in heart position and subsequently differences in slice position between breath-holding and free-breathing as the breath-hold data were acquired at end-inspiration in patients. The reduced strain agreement may also suggest the variabilities of breath-hold cine DENSE

in patients due to their reduce breath-hold capacities. In summary, breath-hold acquisition may not be the best reference to evaluate the free-breathing acquisition.

In patients, the reproducibility of strain imaging by self-NAV was less than that by dNAV. These results are likely due to the imperfect compensation for the intra-heartbeat motion. The reference segments of all encoding dimensions were chosen to reduce the overall phase errors in the displacement encoded phase images. However, intra-heartbeat phase error correction may still be incomplete and inaccurate. Ideally, a reference segment that has minimal phase error should be obtained and so the phase correction of other segments is in reference to the true phase. In reality, such prior information is not available without an accurate measurement of the motion of the heart due to respiration. Therefore, errors in the displacement phase images may still exist and cause reduced reproducibility of the strain quantification. Such phase errors were identified in the data of a patient subject. This particular subject had a relatively slower heart rate and longer RR interval (approximately 1100 ms). Extreme phase errors at late-diastole were observed in the self-NAV acquisition. These errors cannot be reduced with the current methods and lead to strain errors. The reproducibility of strain by self-NAV was much closer to that by dNAV when excluded the data of this subject, as shown in Figure 4.10.

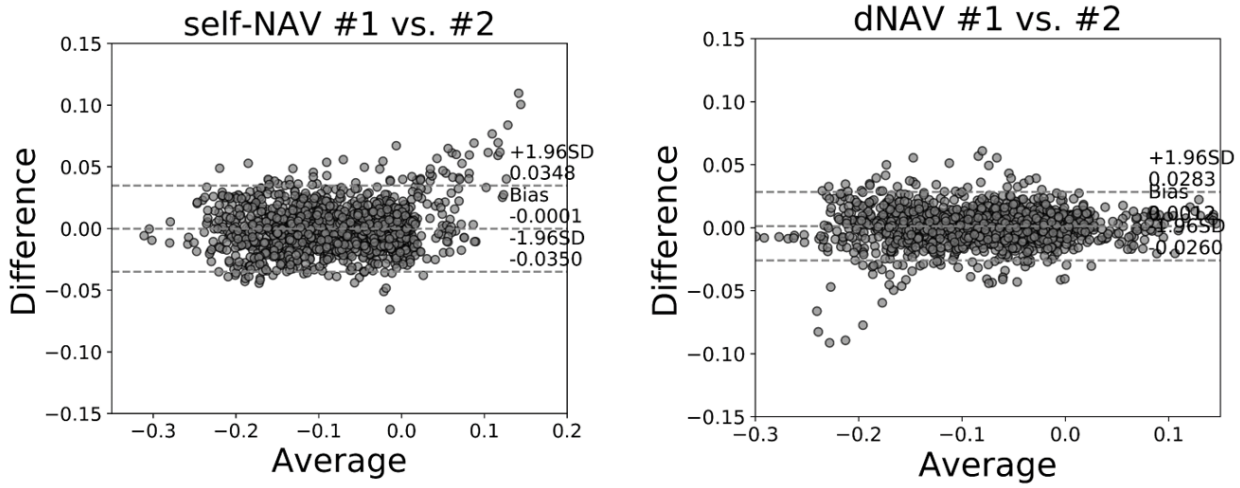

Figure 4.10. Replot of free-breathing strain reproducibility in patients (Figure 4.6F,G) with one patient dataset excluded. Extreme phase errors was observed in the displacement phase images and the phase correction was not able to compensate for these erros.

4.4.3. Limitations

There are a few limitations in the current self-NAV method. A large field-of-view was employed even with localized stimulated-echo generation. The intra-heartbeat motion correction and inter-heartbeat translation correction are performed off-line. The proposed method to jointly select reference segments for all encoding dimensions was able to reduce the overall phase offset in the displacement phase images. However, this method still cannot correct for the absolute phase errors accurately. The imaging time of the proposed method is still relatively long compared to breath-hold. The method can be combined with in-plane acceleration or simultaneous multi-slice imaging to improve imaging efficiency and shorten imaging time. Specifically, previous studies have demonstrated the feasibility of accelerating cine DENSE using the compressed sensing method. Only the best-matched phase-cycling pair per segment was accepted for reconstruction for a fair comparison with dNAV and breath-hold, whereas more instances of phase-cycling pairs of similar quality can be utilized. The reconstruction is performed after the data acquisition is done. An interactive interface that provides visual feedback of images at each iteration and allows user control of the scan (pause, continue or stop the scan) may be useful [17].

4.4.4. Conclusion

In summary, the experiments in healthy subjects and patients proved that the self-NAV method was overall advantageous over dNAV. The self-NAV method consistently achieved better suppression of the T1-relaxation echo than dNAV in all subjects and better strain quantification in healthy subjects. The reproducibility of strain by self-NAV was overall good except in cases with extreme phase errors due to the intra-heartbeat motion. The self-NAV method does not require additional scout scans. Future work should investigate options to optimize the imaging protocols and develop a more accurate estimation and compensation method for the intra-heartbeat phase errors.

4.5. References

1. Kim, D., et al., *Myocardial tissue tracking with two-dimensional cine displacement-encoded MR imaging: development and initial evaluation.* Radiology, 2004. **230**(3): p. 862-871.
2. Kihlberg, J., et al., *Clinical experience of strain imaging using DENSE for detecting infarcted cardiac segments.* Journal of Cardiovascular Magnetic Resonance, 2015. **17**(1): p. 50.
3. Kim, W., et al., *Extraction of cardiac and respiratory motion cycles by use of projection data and its applications to NMR imaging.* Magnetic resonance in medicine, 1990. **13**(1): p. 25-37.
4. Epstein, F.H. and W.D. Gilson, *Displacement - encoded cardiac MRI using cosine and sine modulation to eliminate (CANSEL) artifact - generating echoes.* Magnetic Resonance in Medicine: An Official Journal of the International Society for Magnetic Resonance in Medicine, 2004. **52**(4): p. 774-781.
5. Cai, X. and F.H. Epstein, *Free - breathing cine DENSE MRI using phase cycling with matchmaking and stimulated - echo image - based navigators.* Magnetic resonance in medicine, 2018.
6. Anderson, A.W. and J.C. Gore, *Analysis and correction of motion artifacts in diffusion weighted imaging.* Magnetic resonance in medicine, 1994. **32**(3): p. 379-387.
7. Mills, P., et al., *Localized imaging using stimulated echoes.* Magnetic resonance in medicine, 1987. **5**(4): p. 384-389.
8. Felmlee, J.P., et al., *Adaptive motion compensation in MRI: accuracy of motion measurement.* Magnetic resonance in medicine, 1991. **18**(1): p. 207-213.
9. Shechter, G. and E.R. McVeigh. *MR motion correction of 3D affine deformations*. in *Proceedings Int Soc Mag Reson Med*. 2003. Citeseer.
10. Fessler, J.A. and B.P. Sutton, *Nonuniform fast Fourier transforms using min-max interpolation.* IEEE Transactions on Signal Processing, 2003. **51**(2): p. 560-574.
11. Zhong, X., P.A. Helm, and F.H. Epstein, *Balanced multipoint displacement encoding for DENSE MRI.* Magnetic resonance in medicine, 2009. **61**(4): p. 981-988.
12. Gudbjartsson, H. and S. Patz, *The Rician distribution of noisy MRI data.* Magnetic resonance in medicine, 1995. **34**(6): p. 910-914.
13. Dietrich, O., et al., *Influence of multichannel combination, parallel imaging and other reconstruction techniques on MRI noise characteristics.* Magnetic resonance imaging, 2008. **26**(6): p. 754-762.

14. Segmentation, A.H.A.W.G.o.M., et al., *Standardized myocardial segmentation and nomenclature for tomographic imaging of the heart: a statement for healthcare professionals from the Cardiac Imaging Committee of the Council on Clinical Cardiology of the American Heart Association.* Circulation, 2002. **105**(4): p. 539-542.
15. Spottiswoode, B.S., et al., *Tracking myocardial motion from cine DENSE images using spatiotemporal phase unwrapping and temporal fitting.* IEEE transactions on medical imaging, 2007. **26**(1): p. 15-30.
16. Spottiswoode, B.S., et al., *Motion-guided segmentation for cine DENSE MRI.* Medical image analysis, 2009. **13**(1): p. 105-115.
17. Sachs, T.S., et al., *The real-time interactive 3-D-DVA for robust coronary MRA.* IEEE transactions on medical imaging, 2000. **19**(2): p. 73-79.

Chapter 5
Discussion and Conclusions

5.1 Summary

This dissertation developed and evaluated self-navigated methods that aimed to address the artifacts in free-breathing cine displacement-encoded stimulated-echo (cine DENSE) for myocardial strain imaging.

Chapter 2 described a match-making framework for image reconstruction where residual T_1-echo energy (rT1E) was first minimized and stimulated-echo image-based navigators (ste-iNAVs) were then reconstructed and used for in-plane motion estimation and correction. The framework was demonstrated to be effective in suppressing the striping and blurring artifacts due to inter-heartbeat breathing. Phantom experiments demonstrated that minimal rT1E indicated minimal motion between the acquisitions of the phase-cycled data and that subsequent motion correction reduced blurring. Evaluation in healthy subjects demonstrated that the minimal rT1E suppressed striping artifacts better than minimizing diaphragm navigator window. The conventional image-based navigators (c-iNAV) were also investigated. Without effective suppression of the T_1-relaxation echo, the c-iNAV is corrupted by the residual T_1-echo signal and therefore respiratory motion estimated from c-iNAVs is not accurate. The reconstruction was performed retrospectively after free-breathing data were acquired with a prescribed protocol.

Chapter 3 introduced an adaptive imaging algorithm to prospectively reduce the rT1E during the acquisition. The algorithm uses rT1E of the post-subtraction k-space data as feedback to guide the data acquisition to repeat the k-space segment with the highest rT1E. Experiments in healthy subjects where cine DENSE datasets were acquired with the adaptive algorithm for a fixed duration demonstrated that the relative rT1E converged and the quality of cine DENSE images improved as the algorithm progressed. The stopping criteria values were determined from the in vivo experiments. In this

chapter, the third type of respiratory motion artifacts, signal cancellation due to intra-heartbeat motion, was also investigated. A global phase correction was introduced to compensate the phase variances due to intra-heartbeat motion and demonstrated to reduce signal cancellation artifacts.

Chapter 4 evaluated the developed self-navigated method in healthy subjects and patients with heart disease and compared its performance with the conventional dNAV method. The free-breathing data acquisition used the adaptive imaging algorithm with the three stopping criteria applied. Reconstruction used the framework introduced in Chapter 2. In healthy subjects, the self-NAV method outperformed dNAV with lower rT1E, better agreement of free-breathing strain with breath-hold strain, and better reproducibility of strain quantification. In patients, the self-NAV achieved better suppression of the T_1-relaxation echo and similar agreement of strain with breath-hold strain. The reproducibility of strain was not as good as dNAV due to extreme phase error from the intra-heartbeat motion in one subject. Overall, the self-NAV method is promising for accurate and reproducible free-breathing myocardial strain with cine DENSE.

5.2 Discussion

5.2.1. T_1-relaxation echo suppression

The T_1-relaxation echo has been a major source of artifacts for cine DENSE imaging [1, 2] and effective suppression of this echo is important for high-quality strain imaging with cine DENSE. The residual T_1-echo and subsequent striping artifacts are unique challenges to free-breathing cine DENSE MRI. The self-navigation methods presented in this dissertation used a data-driven metric, rT1E, to guide data acceptance in retrospective reconstruction (match-making framework in Chapter 2) and data acquisition (adaptive imaging algorithm in Chapter 3) in prospective artifacts reduction to reduce the residual T_1-echo signal. This method, reducing the residual T_1-echo energy, was proven effective in reducing striping artifacts and is a better method than the conventional dNAV.

5.2.2. Residual T_1-echo energy calculation

In the adaptive acquisition algorithm, the rT1E is defined as energy in k-space over the high-frequency region irrespective of the location of the T_1-relaxation echo center, i.e. the second half of the interleaves with spiral-out readouts. (Figure 5.1A, E) Therefore, the rT1E does not necessarily include the T_1 -relaxation echo center with the encoding frequency and encoding method used (Figure 5.1E). Nonetheless, it is sufficient to distinguish matched phase-cycling pairs from mismatched phase-cycling pairs. The reason is that the T_1-relaxation echo signal exists in the entire k-space.

Alternatively, the rT1E may be defined with a region around the T_1-echo center as shown in Figure 5.1B-D, F-H. Using these definitions, the rT1E values are likely more sensitive to the residual T_1-echo signal. There are a few disadvantages though. First, the calculation needs prior knowledge of the T_1-echo center. Secondly, the calculation cannot apply to acquisitions without in-plane displacement encoding (background encoding with simple encoding method). Thirdly, the region radius should be carefully chosen based on the encoding frequency to avoid regions around the stimulated-echo center.

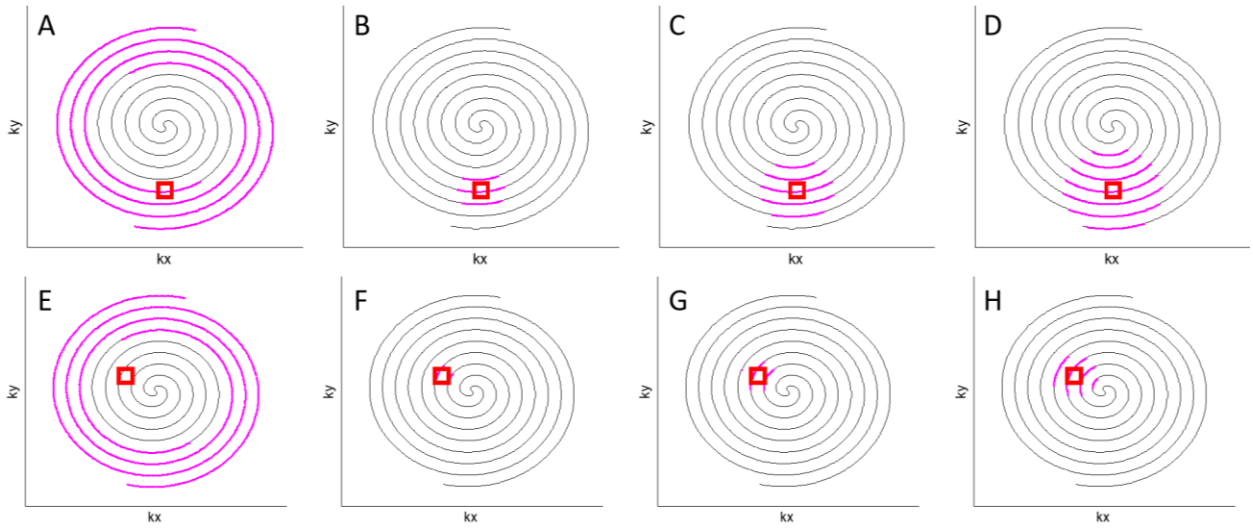

Figure 5.1. Illustration of k-space regions for calculation of rT1E in a spiral trajectory. The k-space region included in the calculation of rT1E is highlighted in pink. The T1-relaxation echo center is labeled with a red square, which is at 0.1 cyc/mm and 0.05 cyc/mm for the simple encoding (A-D) and balanced encoding example (E-H) respectively. (A, E) The region of high-spatial-frequency regardless of the T_1-echo center. The region does not include the T_1-echo

center with balanced encoding. (B, F) The k-space region around T_1-echo center with a radius of $k_e/3$. (C, G) The k-space region around T_1-echo center with a radius of $k_e/2$. (D, H) The k-space region around T_1-echo center with a radius of $2k_e/3$. As the radius increases, the region grows closer to the stimulated-echo center.

Figure 5.2 shows the rT1E results of the adaptive acquisitions in Chapter 3 calculated with the definition shown in Figure 5.1G, i.e. around the T_1-echo center with a radius of $k_e/2$. Compared to the results in Figure 3.6A, the averaged relative rT1E at the beginning of the acquisition was much higher as expected. The rT1E converged similarly to the results. Yet, a different threshold value would perhaps be chosen using this definition.

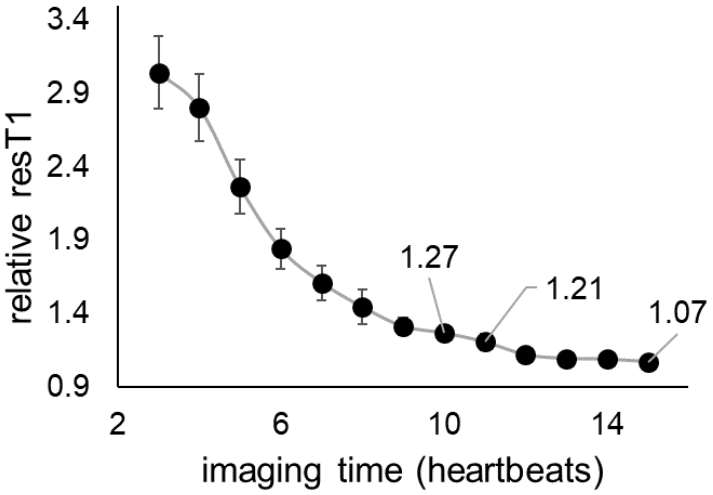

Figure 5.2. Residual T_1-echo results of experiments in chapter 3 with a different calculation. The rT1E includes k-space region shown in Figure 5.1G, i.e. a circular region with a radius of $k_e/2$.

5.2.3. Displacement encoding method

The experiments in Chapters 2-4 utilized different displacement encoding methods. Specifically, the experiments in Chapter 2 used simple displacement encoding and the experiments in Chapters 3-4 used balanced encoding. The advantages of imaging with balanced encoding is that the centers of T_1-relaxation and displacement-encoded stimulated echoes do not overlap in the k_{xy} plane, which may facilitate detecting a k-space segment that is corrupted by residual T_1-echo signal. The disadvantage is that with

balanced encoding, the encoding frequency is typically smaller due to a greater weighting factor in the displacement encoded phase. As a result, the T_1-echo center is closer to the stimulated-echo center. Further, with simple encoding, a large encoding frequency can be used so that the T_1-relaxation echo center is further from the stimulated-echo center when the in-plane displacement encoding is used. However, the T_1-echo and stimulated-echo centers overlap for the background encoding acquisition.

Despite the differences between simple encoding and balanced encoding, the same rT1E threshold may be applied with the chosen definition of rT1E (Figure 5.1A, E).

5.2.4. Data selection

All the reconstruction of free-breathing cine DENSE images accepted one repetition of data for all k-space segments. The experiments were designed for the purpose of fair comparison of image apparent SNR between the self-NAV and dNAV methods and among different time points during the adaptive acquisition process. In this way, each reconstruction had the same intrinsic SNR given the same imaging time. The apparent SNR was, therefore, a quantification of artifact level in the images. However, there can be more matched phase-cycling pairs at the end of the adaptive acquisition. As in the example shown in Figure 5.3, the reconstruction accepted the best-matched pair (red curve) but not the other two phase-cycling pairs that also met the rT1E threshold (blue curves). Accepting all the phase-cycling pairs that meet the rT1E threshold can further improve the quality of the reconstructed images. Such a method can be useful for imaging subjects where SNR is limited, such as patients with obesity or devices.

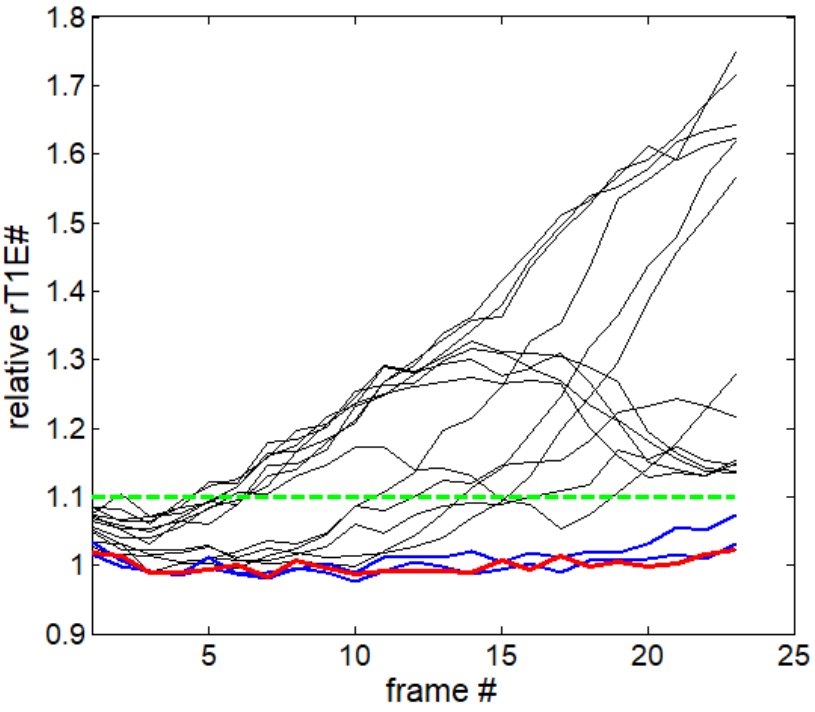

Figure 5.3. The rT1E of all phase-cycling pairs and all frames at the end of the adaptive acquisition. There are 16 phase-cycling pairs in total with the acquisition of this segment repeated 4 times. The reconstruction accepted the phase-cycling pairs with the lowest rT1E (red curve). Two other phase-cycling pairs (blue curves) also met the rT1E threshold, i.e. the relative rT1E of all frames are below the threshold of 1.1 (green dashed line). Yet, these two phase-cycling pairs were not included in the reconstruction of the final images.

5.2.5. Intra-heartbeat motion correction

The intra-heartbeat motion induced phase error is also a unique challenge of cine DENSE compared to other CMR imaging techniques. The intra-heartbeat breathing causes both signal cancelation and phase errors in the displacement encoded phase images. This dissertation attempts to address the problem by applying a global phase factor to account for the phase variations among k-space segments and jointly selecting reference segments to reduce the overall displacement phase errors at late diastole. Overall, these methods can reduce signal cancellation and reduce the phase errors (Figure 3.5, Figure 4.8). However, these methods still cannot completely remove the phase errors.

Accurate estimation and compensation for the intra-heartbeat motion induced phase errors may be the last thing in the bucket list towards reproducible and reliable strain imaging with free-breathing cine DENSE.

5.2.6. Optimizing the adaptive imaging algorithm

As was discussed in Chapter 3, the current design of the adaptive acquisition algorithm requires the online reconstruction to store all the previously acquired phase-cycling data and the computation task can be a limit to expanding the imaging protocol. The algorithm can potentially be optimized with the following adjustments,

1. Acquire one instance of both phase-cycling dimensions to start with;
2. At each iteration, only repeat acquiring the second phase-cycling of the target segment;
3. Calculate feedback after each heartbeat;
4. Replace the second phase-cycling data if the rT1E decreased.

In this way, there is no need to store all the previously acquired data and there is only 1 new phase-cycling pair needed to calculate rT1E. The algorithm may be able to converge faster.

5.2.7. Longitudinal strain imaging

So far, all the studies in this dissertation only imaged a short axis mid-ventricular slice and calculated circumferential strain. Yet, there is growing interest in quantifying longitudinal strain [3-5]. With cine DENSE, longitudinal strain can be obtained by imaging a slice on the longitudinal views (2-, 3-, or 4-chamber views) or 3D acquisition [6]. The self-NAV methods introduced in this dissertation can be applied to imaging these views and longitudinal strain. Figure 5.4 and Figure 5.5 show an example cine DENSE acquisition on the 4-chamber view with the self-NAV method. The data was acquired in a healthy subject. Similar to the results for short-axis imaging, the residual T_1-echo energy decreased and the image quality improved as the acquisition progressed (Figure 5.4). The final magnitude images and displacement-encoded phase images of this acquisition are high quality at both end-systole and end-diastole. 2D displacement and longitudinal strain were analyzed from this dataset (Figure 5.5).

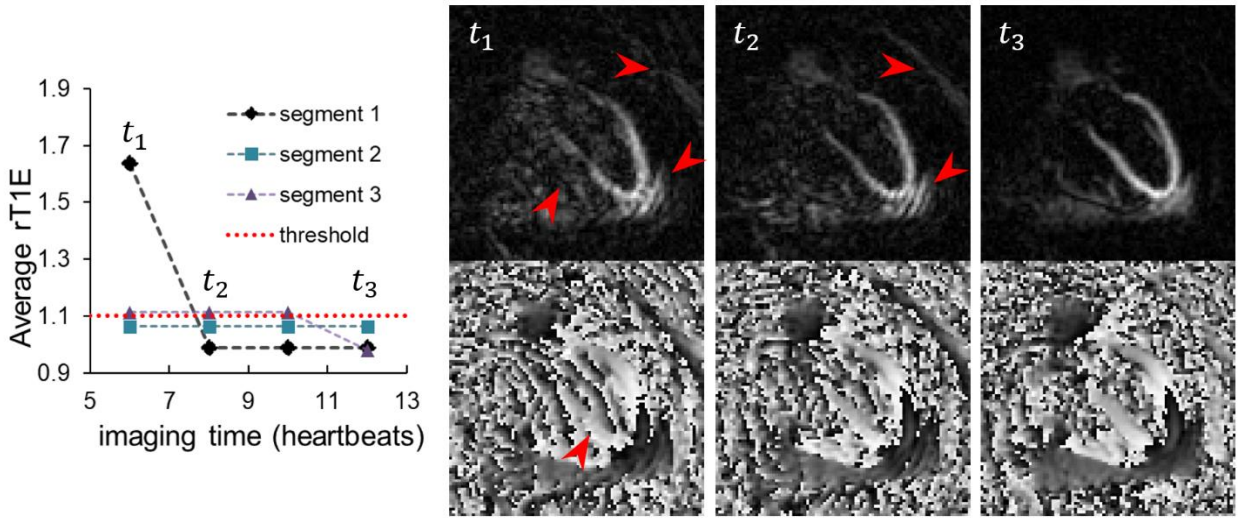

Figure 5.4. An example adaptive acquisition for a 4-chamber view. Left: residual T_1-echo energy values of all the segments during the acquisition. Right: reconstructions at different times during the acquisition. An end-diastolic frame is shown. The images at beginning of the acquisition (t_1) had artifacts due to strong residual T_1-echo signal in both the magnitude and phase images (arrows). These artifacts were reduced (t_2). The imaging stopped after the rT1E values were below the threshold and the images were high quality and free of artifacts (t_3).

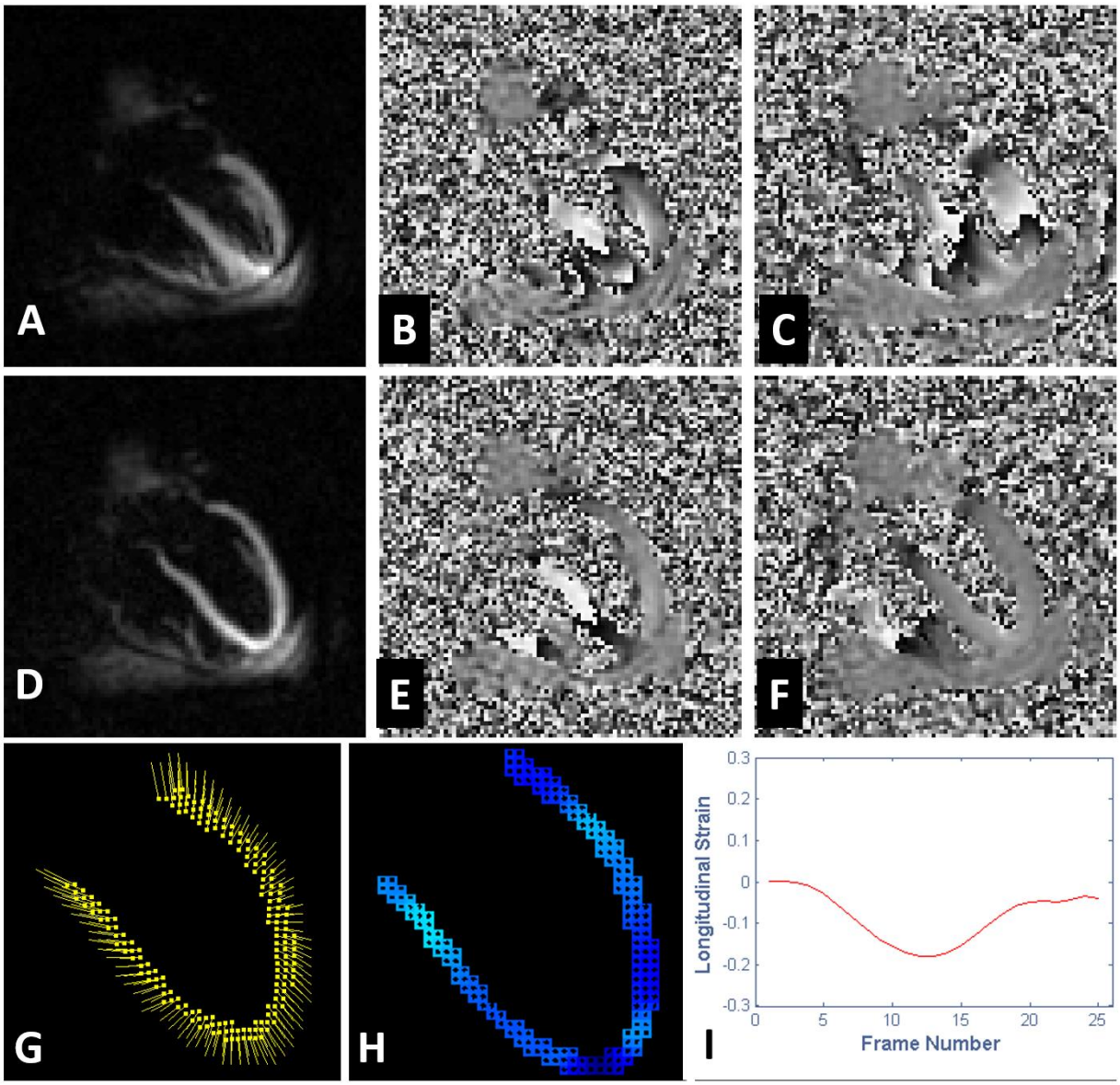

Figure 5.5. An example of longitudinal strain imaging with the self-NAV cine DENSE method. (A-C) The magnitude and displacement-encoded images at end-systole (trigger time = 390 ms). (D-F) The same images at end-diastole. The magnitude images are high quality without significant breathing artifacts and good delineation of the left ventricular myocardium (trigger time = 750 ms). So are the phase images. (G) 2D Lagrangian displacement map estimated from the phase images at end-systole. (H) The longitudinal strain map at end-systole. (I) The global longitudinal strain time curve.

5.2.8. B_0 inhomogeneity correction

B_0 inhomogeneity is a major challenge for spiral imaging. Off-resonance leads to blurriness in the images. The studies in this dissertation either used a short spiral readout (Chapter 2) or corrected for the center-frequency offset in the heart (Chapters 3-4) with field maps to reduce the inhomogeneity induced blurriness [7]. However, these methods may not be sufficient to compensate for the inhomogeneity.

The field inhomogeneity can vary greatly from region to region in cardiac MRI. The results of compensating for center frequency offset depend on the region-of-interest for estimation. Figure 5.6 shows a breath-hold cine DENSE image reconstructed without (top) and with (bottom) correction for center-frequency shift. In this example, the center frequency offset was estimated using a small region around the heart. Thus, the center frequency shift compensation significantly reduced blurriness in the region around the left ventricle (green arrows). However, reduced sharpness can be observed in the chest wall and right ventricle (yellow arrows). With the tissue-air interface and perturbations from the large epicardial veins, evident focal regions of field inhomogeneity are often observed in the heart [8, 9]. The estimated variation of off-resonance in the left ventricle within a slice was 71 Hz at 1.5T [8] and 130 Hz at 3.0T [9]. In addition, the field map data are acquired during the first two heartbeats with free-breathing and therefore may contain errors due to breathing motion. The field map data acquisition may be improved. A better correction method such as multi-frequency approximation[10] or iterative methods [11, 12] may be useful to account for the spatial variations of inhomogeneity in the heart.

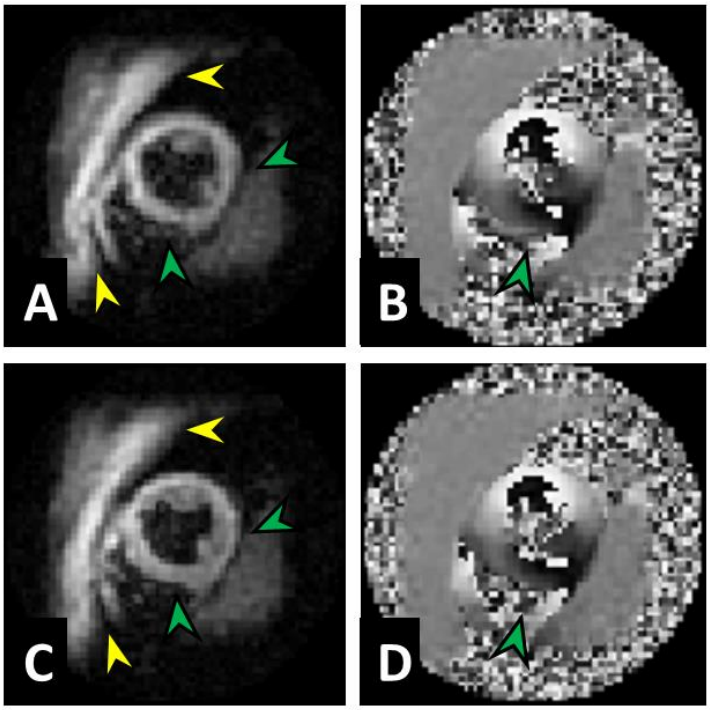

Figure 5.6. Example cine DENSE data reconstructed without and with off-resonance correction. (A, B) The reconstruction without off-resonance correction has significant blurriness and degraded definition of the myocardium borders. (C, D) The reconstruction that compensates for the center frequency offset estimated from the heart region improved the sharpness of the myocardium boarder. (Green arrows) However, the chest wall and the right ventricle boarders became blurrier. (Yellow arrows)

5.2.9. Other limitations

There are a few limitations of the self-NAV method. The differences in heart positions between end-inspiration and end-expiration can be problematic for the planning of cine DENSE with the localized stimulated-echo generation. As shown in Figure 5.7, both breath-hold and free-breathing cine DENSE acquisitions were planned with short-axis localizer images acquired with breath-hold and end-inspiration. The breath-hold DENSE acquisition had intact left-ventricle. However, with the same imaging parameters, the anterior wall of the myocardium had significant signal drop as the heart position shifted off the center of the slice profiles (of the displacement encoding RF pulses) at end-expiration (red arrow). The imaging time of the self-NAV method is still relatively long compared to breath-hold imaging (18 on average vs 6 heartbeats per

encoding). All the imaging was performed on 3T scanners and the performance of the methods on 1.5T systems was not investigated. In Chapter 3 and Chapter 4, a large field-of-view was used for all acquisitions despite the usage of localized generation the stimulated-echoes. The imaging protocol may be optimized to further reduce the imaging time with a smaller field-of-view. Figure 5.8 demonstrates the acquisition of cine DENSE with a field-of-view of 200 mm and 4 interleaves per image. The imaging time was 4 heartbeats per encoding with breath-hold and the field map data were acquired with a large field-of-view.

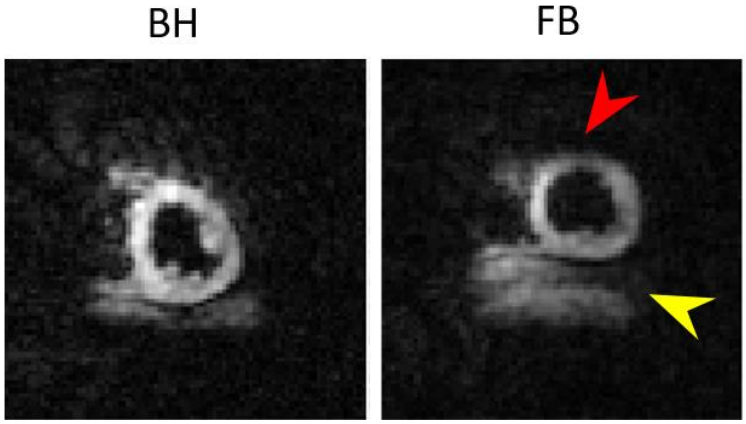

Figure 5.7. Comparison of heart positions with breath-hold and free-breathing. The imaging was performed at end-inspiration with breath-hold (BH) in this patient while the free-breathing (FB) acquisition tended to accept data at end-expiration. Therefore, the heart positions were very different (yellow arrow). The heart position shift caused signal loss in the anterior wall of the left ventricle (red arrow) with the use of localized generation of stimulated-echoes.

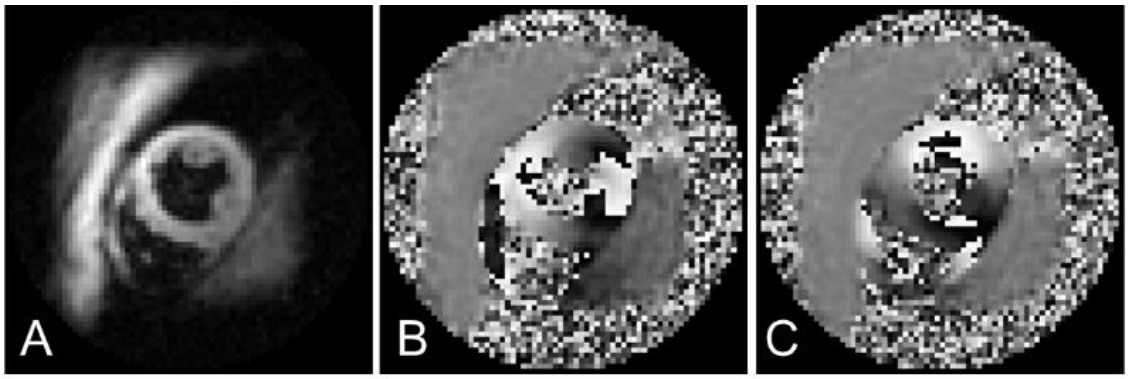

Figure 5.8. Example data acquired with a reduced field-of-view and a reduced number of interleaves per image. The field map data is acquired with a large field-of-view. Center frequency offset was corrected with the field maps.

5.3 Future directions

Future investigations can potentially aim to improve the reliability of the strain imaging, reduce the imaging time, and improve the spatial coverage of the presented self-NAV free-breathing cine DENSE method.

Intra-heartbeat motion induced phase errors was partially solved with the presented methods but remain a problem and can lead to strain errors. An accurate estimation and correction for the phase errors is important for reliable and reproducible free-breathing strain imaging. The phase errors may be estimated from the free-breathing data. While the respiratory motion varies from heartbeat to heartbeat, the heart motion is similar among heartbeats. As discussed in section 5.2.4, the adaptive acquisition produces redundant data. Only the post-subtraction data with the lowest rT1E are accepted for the final image reconstruction. The other post-subtraction data still contain the heart motion information. The heart motion can be extracted from redundant data as the principal feature. Another approach to accurately estimate the phase errors could be to acquire k-space central lines along with the spiral data. Fourier Transform the k-space central lines produce 1D projections of the heart. Phase-cycling subtraction of the 1D projections produce localized heart projections and cross-correlation [13-15] may provide accurate intra-heartbeat translations for intra-heartbeat motion compensation.

A potential approach to reduce the imaging time of the self-NAV method is to employ in-plane acceleration acquisition and reconstruction methods, such as parallel imaging [16, 17] and compressed sensing [18-21]. With these methods, less k-space data is sampled than that required by the Nyquist sampling theorem. The imaging time is reduced correspondingly. The images reconstructed from inverse Fourier Transform contain artifacts due to the undersampling. However, these artifacts can be removed utilizing the spatial correlations of signal received by different coils or the sparsity properties of MRI images in a transformed domain. Previously, parallel imaging and compressed sensing were applied to accelerate 2D and 3D cine DENSE imaging and were demonstrated to provide accurate strain quantification at up to 4-fold of acceleration [22].

The current imaging is limited to 2D single slice imaging while 3D cine DENSE imaging could be useful to increase image SNR and calculate more myocardial mechanics such as torsion. Match-making of phase-cyclings applies to 3D free-breathing cine

DENSE. However, reconstruction of 3D ste-iNAVs may be challenging and compensation for the motion in the stimulated echoes may require additional acquisitions of 3-dimensional projections. Another way to expand the spatial coverage in the slice direction is to utilize simultaneous multi-slice (SMS) imaging [23, 24]. With SMS methods, the imaging RF pulses are modified to excite multiple slices and the k-space of the multiple slices are collapsed together in the collected data. Image reconstruction often uses the spatial profiles of the data in the slices to try to separate the images from each other. To better separate and reconstruct the images, careful designed phase modulations are often applied to the different slices during the excitation. The benefit of SMS is that the imaging time is reduced without sacrificing the imaging SNR of each slice.

Recently, there has been growing interest in applying deep learning methods to the field of medical imaging. Studies have demonstrated promising usage of deep learning methods in applications including but not limited to image classification, image segmentation, artifact removal and accelerated reconstruction [25, 26]. Future work can potentially investigate whether deep learning can be an alternative and/or complementary method to the presented self-NAV methods for artifact removal in free-breathing cine DENSE.

5.4 Conclusion

Strain imaging with cine DENSE is a promising method for quantification of cardiac function and detection of global and regional myocardium dysfunction. The requirement of breath-holds during data acquisition is a major challenge for patient imaging. The conventional dNAV method for free-breathing cardiac imaging has multiple disadvantages and the field of cardiac MRI is shifting towards self-navigated free-breathing imaging.

This dissertation developed self-navigated methods that specifically address the artifacts in free-breathing cine DENSE. A match-making of phase-cycling pairs and adaptive acquisition algorithm were proposed to suppress the T_1-relaxation echo and striping artifacts in free-breathing cine DENSE. Image-based navigators reconstructed with the post-subtraction stimulated echoes were used to correct for blurriness due to in-plane motion and phase error due to intra-heartbeat motion. Initial evaluations

demonstrated that the self-NAV method was a better than dNAV for free-breathing cine DENSE imaging. Future investigations to improve the accuracy of intra-heartbeat motion correction and imaging efficiency are necessary.

5.5 References

1. Epstein, F.H. and W.D. Gilson, *Displacement - encoded cardiac MRI using cosine and sine modulation to eliminate (CANSEL) artifact - generating echoes.* Magnetic Resonance in Medicine: An Official Journal of the International Society for Magnetic Resonance in Medicine, 2004. **52**(4): p. 774-781.
2. Zhong, X., et al., *Selective suppression of artifact - generating echoes in cine DENSE using through - plane dephasing.* Magnetic resonance in medicine, 2006. **56**(5): p. 1126-1131.
3. Sengeløv, M., et al., *Global longitudinal strain is a superior predictor of all-cause mortality in heart failure with reduced ejection fraction.* JACC: Cardiovascular Imaging, 2015. **8**(12): p. 1351-1359.
4. Park, J.J., et al., *Global longitudinal strain to predict mortality in patients with acute heart failure.* Journal of the American College of Cardiology, 2018. **71**(18): p. 1947-1957.
5. Smiseth, O.A., et al., *Myocardial strain imaging: how useful is it in clinical decision making?* European heart journal, 2015. **37**(15): p. 1196-1207.
6. Zhong, X., et al., *Imaging three - dimensional myocardial mechanics using navigator - gated volumetric spiral cine DENSE MRI.* Magnetic resonance in medicine, 2010. **64**(4): p. 1089-1097.
7. Irarrazabal, P., et al., *Inhomogeneity correction using an estimated linear field map.* Magnetic resonance in medicine, 1996. **35**(2): p. 278-282.
8. Reeder, S.B., et al., *In vivo measurement of T* 2 and field inhomogeneity maps in the human heart at 1.5 T.* Magnetic resonance in medicine, 1998. **39**(6): p. 988-998.
9. Noeske, R., et al., *Human cardiac imaging at 3 T using phased array coils.* Magnetic Resonance in Medicine: An Official Journal of the International Society for Magnetic Resonance in Medicine, 2000. **44**(6): p. 978-982.
10. Man, L.C., J.M. Pauly, and A. Macovski, *Multifrequency interpolation for fast off - resonance correction.* Magnetic resonance in medicine, 1997. **37**(5): p. 785-792.
11. Sutton, B.P., D.C. Noll, and J.A. Fessler, *Fast, iterative image reconstruction for MRI in the presence of field inhomogeneities.* IEEE transactions on medical imaging, 2003. **22**(2): p. 178-188.

12. Chen, W. and C.H. Meyer, *Semiautomatic off - resonance correction in spiral imaging.* Magnetic Resonance in Medicine: An Official Journal of the International Society for Magnetic Resonance in Medicine, 2008. **59**(5): p. 1212-1219.
13. Ehman, R.L. and J.P. Felmlee, *Adaptive technique for high-definition MR imaging of moving structures.* Radiology, 1989. **173**(1): p. 255-263.
14. Liu, J., et al., *Respiratory and cardiac self - gated free - breathing cardiac CINE imaging with multiecho 3D hybrid radial SSFP acquisition.* Magnetic resonance in medicine, 2010. **63**(5): p. 1230-1237.
15. Feng, L., et al., *XD - GRASP: golden - angle radial MRI with reconstruction of extra motion - state dimensions using compressed sensing.* Magnetic resonance in medicine, 2016. **75**(2): p. 775-788.
16. Griswold, M.A., et al., *Generalized autocalibrating partially parallel acquisitions (GRAPPA).* Magnetic Resonance in Medicine: An Official Journal of the International Society for Magnetic Resonance in Medicine, 2002. **47**(6): p. 1202-1210.
17. Pruessmann, K.P., et al., *SENSE: sensitivity encoding for fast MRI.* Magnetic resonance in medicine, 1999. **42**(5): p. 952-962.
18. Lustig, M., D. Donoho, and J.M. Pauly, *Sparse MRI: The application of compressed sensing for rapid MR imaging.* Magnetic Resonance in Medicine: An Official Journal of the International Society for Magnetic Resonance in Medicine, 2007. **58**(6): p. 1182-1195.
19. Lustig, M., et al. *kt SPARSE: High frame rate dynamic MRI exploiting spatio-temporal sparsity*. in *Proceedings of the 13th Annual Meeting of ISMRM, Seattle*. 2006.
20. Pedersen, H., et al., *k - t PCA: temporally constrained k - t BLAST reconstruction using principal component analysis.* Magnetic resonance in medicine, 2009. **62**(3): p. 706-716.
21. Lingala, S.G., et al., *Accelerated dynamic MRI exploiting sparsity and low-rank structure: kt SLR.* IEEE transactions on medical imaging, 2011. **30**(5): p. 1042-1054.
22. Chen, X., et al., *Accelerated two-dimensional cine DENSE cardiovascular magnetic resonance using compressed sensing and parallel imaging.* Journal of Cardiovascular Magnetic Resonance, 2016. **18**(1): p. 38.
23. Barth, M., et al., *Simultaneous multislice (SMS) imaging techniques.* Magnetic resonance in medicine, 2016. **75**(1): p. 63-81.

24. Breuer, F.A., et al., *Controlled aliasing in volumetric parallel imaging (2D CAIPIRINHA).* Magnetic Resonance in Medicine: An Official Journal of the International Society for Magnetic Resonance in Medicine, 2006. **55**(3): p. 549-556.

25. Gjesteby, L., et al. *Reducing metal streak artifacts in CT images via deep learning: Pilot results*. in *The 14th International Meeting on Fully Three-Dimensional Image Reconstruction in Radiology and Nuclear Medicine*. 2017.

26. Zhu, B., et al., *Image reconstruction by domain-transform manifold learning.* Nature, 2018. **555**(7697): p. 487.

Appendix: List of publications

Conference abstracts

1. Cai, X. Meyer, C. & Epstein, F. Free-breathing cine DENSE imaging by adaptively diminishing the residual T1-echo energy: evaluation in healthy subjects. SCMR 2019. Accepted.
2. Cai, X. & Epstein, F. Self-gated free-breathing cine DENSE imaging by adaptively reducing residual T1-echo energy. In Proceedings Int. Soc. Mag. Reson. Med. 26. 2018.
3. Cai, X. & Epstein, F. Free-breathing cine DENSE using phase-cycling with match-making and stimulated-echo image-based navigators. CMR 2018.
4. Cai, X. & Epstein, F. Artifact compensation strategy for free-breathing cine DENSE using match-maker echoes. ISMRM workshop on magnetic resonance imaging of cardiac function, 2017. Proffered oral presentation.
5. Cai, X., Yang, Y., Salerno, M., Kramer, C., Bilchick, K. & Epstein, F. Improved image-based navigators (iNAVs) for free-breathing cine DENSE using principle component analysis to separate the stimulated echo and T1 relaxation signals. In Proceedings Int. Soc. Mag. Reson. Med. 25. 2017, P5054.
6. Cai, X., C., Bilchick, K. & Epstein, F. A novel and robust reconstruction method for free-breathing cine DENSE by minimizing k-space entropy. In Proceedings Int. Soc. Mag. Reson. Med. 25. 2017, P3946.
7. Cai, X., Yang, Y., Salerno, M., Kramer, C., Bilchick, K. & Epstein, F. Improved free-breathing cine DENSE using image-based navigators with motion compensation and compressed sensing: development and initial evaluation. Journal of Cardiovascular Magnetic Resonance. 2017. W012.
8. Cai, X., C., Bilchick, K. & Epstein, F. Accurate and rapid longitudinal strain imaging by cine DENSE using one-dimensional longitudinal displacement encoding. Journal of Cardiovascular Magnetic Resonance. 2017. W024.
9. Cai, X., C., Epstein, F., Auger, D. & Bilchick, K. Improved DENSE Strain Imaging Using a Reduced Field of View in a Patient with Heart Failure and a Cardiac Implantable Electronic Device. Journal of Cardiovascular Magnetic Resonance. 2017.

10. Cai, X., Chen, X., Yang, Y., Salerno, M., Weller, D., Meyer, C. & Epstein, F. Free-breathing 2D cine DENSE MRI using localized signal generation, image-based navigators and motion-compensated compressed sensing. In Proceedings Int. Soc. Mag. Reson. Med. 24. 2016, P3126.
11. Cai, X., Chen, X., Yang, Y., Salerno, M., Weller, D., Meyer, C. & Epstein, F. Free-breathing 2D Cine DENSE with Localized Excitation, Self-navigation and Motion Correction. Journal of Cardiovascular Magnetic Resonance. 2016, P319.

Invention disclosures

- Cai, X., Epstein, F. & Zhong, X. Systems and methods for free-breathing DENSE cine MRI using self-navigation. US 15/493,825, April 2017. Patent pending.

Manuscripts

- Cai, X., Meyer C, Salerno M, Epstein H. Free-breathing cine DENSE with adaptive acquisition and motion correction. In preparation for submission to Magnetic Resonance in Medicine.
- Cai X, Epstein FH. Free-breathing cine DENSE MRI using phase cycling with matchmaking and stimulated-echo image-based navigators. Magnetic Resonance in Medicine. 2018 Apr 1. https://doi.org/10.1002/mrm.27199
- Chen, X., Yang, Y., Cai, X., Auger, D. A., Meyer, C. H., Salerno, M., & Epstein, F. H. (2016). Accelerated two-dimensional cine DENSE cardiovascular magnetic resonance using compressed sensing and parallel imaging. Journal of Cardiovascular Magnetic Resonance, 18(1), 38.

Awards

- ISMRM Summa Cum Laude Merit Award (2018)
- ISMRM Cardiac MR Study Group Abstract Award – 1st place (2018)
- CMR2018 Early Career Award-Basic Science finalist (2018)
- CMR2018 Regional Travel Award (2018)
- AHA Predoctoral Fellowship - AHA and CHF Congenital Heart Defect Research Award (2016)